

METAL SPINTRONICS: TUNNELING SPECTROSCOPY IN JUNCTIONS
WITH MAGNETIC AND SUPERCONDUCTING ELECTRODES

A DISSERTATION

SUBMITTED TO THE DEPARTMENT OF ELECTRICAL ENGINEERING

AND THE COMMITTEE ON GRADUATE STUDIES

OF STANFORD UNIVERSITY

IN PARTIAL FULFILLMENT OF THE REQUIREMENTS

FOR THE DEGREE OF

DOCTOR OF PHILOSOPHY

Hyunsoo Yang

March 2006

© Copyright by Hyunsoo Yang 2006
All Rights Reserved

I certify that I have read this dissertation and that in my opinion it is fully adequate, in scope and quality, as dissertation for the degree of Doctor of Philosophy.

(James S. Harris) Principal Advisor

I certify that I have read this dissertation and that in my opinion it is fully adequate, in scope and quality, as dissertation for the degree of Doctor of Philosophy.

(Stuart S. P. Parkin) co-Principal Advisor

I certify that I have read this dissertation and that, in my opinion it is fully adequate, in scope and quality, as dissertation for the degree of Doctor of Philosophy.

(David A. B. Miller)

Approved for the University Committee on Graduate Studies.

ABSTRACT

Due to fundamental physical limitations the scaling of CMOS devices, after nearly 40 years of a continuous evolution, is coming to an almost certain end. Consequently, more and more research is focused on alternative technologies to CMOS, especially nanoscale devices based on the manipulation and storage of spins and photons. The two main goals are devices that can be scaled to smaller dimensions and devices that consume less power. Also new device architectures are being sought. In the future technologies may involve combinations of elements using both the charge and spin properties of electrons as well as devices that take advantage of the unique properties photons. These devices may be based on materials quite distinct from silicon, such as molecular devices.

In recent years, materials and devices that are based on the manipulation of the electron's spin are often termed *spintronic* to distinguish them from electronic devices based on charge. Spintronic devices have already had enormous technological impact as highly sensitive field sensors used in all magnetic data storage devices today. Among recent advances in spintronics, magnetic tunnel junctions have been under intensive study and are poised to become one of the most widely used spintronic devices: important applications include advanced magnetic field sensors for even higher density hard disk drives and non-volatile memory cells for high performance magnetic random access memories.

The work presented in this thesis focuses on magnetic tunnel junctions, which are devices that display large changes in resistance in magnetic fields as small as ~ 1 Oe. Using sputter deposited crystalline tunnel barriers formed from magnesium oxide (MgO) we show that highly spin polarized tunneling current can be generated with remarkably high polarization values, as high as 90%. The tunneling spin polarization is directly measured using superconducting tunneling spectroscopy. For the past thirty years, such measurements have been carried out using superconducting layers of aluminum so that measurements can only be carried out very low temperatures ($\sim < 0.4$ K). In this work we

evaluate alternative superconducting materials and show that, of these, NbN can be used at temperatures as high as 1.2 K.

An important goal of the work of this thesis was to understand the role of defects in tunnel barriers on the polarization of the tunneling current. As a result of these studies we observed that by deliberately introducing small magnetic nanoparticles in the interior of MgO tunnel barriers, there is evidence for Kondo-assisted tunneling in planar magnetic tunnel junctions. In particular, we find an increased conductance at low bias voltages which we speculate is due to a Kondo resonance. The excess conductance decreases logarithmically with increasing temperature, disappearing above a Kondo temperature, which we observe can be as high as ~ 100 K for very small nanoparticles. In this same voltage and temperature regime we find that the tunneling magnetoresistance is quenched. There has been considerable work in recent years on both theoretical and experimental studies of the Kondo effect in artificial atoms created in two dimensional electron gas systems by applying voltages to gates. These systems are regarded as promising for quantum computing applications. Our results suggest that a promising and simpler system, perhaps operable at higher temperatures, could involve magnetic nanodots embedded in insulating layers with ferromagnetic leads.

A final related project presented in this thesis is the effect on the tunneling spin polarization, and particularly its voltage dependence, of the introduction into the tunnel barrier of thin insulating antiferromagnetic oxide layers. We show that such layers can lead to highly asymmetric voltage dependences of tunneling magnetoresistance (with regard to positive and negative bias voltage), and negative values of tunneling magnetoresistance under certain voltage regimes. Using inelastic tunneling spectroscopy we explore possible origins of such effects.

ACKNOWLEDGMENTS

First of all I was quite lucky to get admission to Stanford. A well organized curriculum and very active research activities were the perfect environment for me. More importantly I joined Jim Harris's group at Stanford University, where I learned and practiced the basic thin film technology. He has always created an open research environment, so that students can pursue self-motivated and self-guided research. I consider the biggest turning point in my life until now to be the experience at IBM Almaden research center under the guidance of Dr. Stuart Parkin, who engages actively in science and the pursuit of excellence, not only by transferring professional knowledge, but by showing the path. Now I appreciate what real passion is.

This work would not be possible without the help of many people. I would like to acknowledge See-Hun Yang and Christian Kaiser. See-Hun taught me how to operate the sputtering machine as well as basic physical concepts. In addition we discussed almost everyday. Christian showed me how to cool samples in the Helium down to 0.25K and I also acknowledge him for much discussion about superconductivity. Thanks to the other members of Stuart's team; Masamitsu Hayashi for Labview help, Brian Hughes for keeping the annealing equipment up, Kevin Roche for general software help, Guenole Jan for some samples from PLD, Luc Thomas for magneto-optical Kerr measurement, Mahesh Samant for general lab help, Xin Jiang and Rai Moriya for helpful discussion, and Anthony Ndirango for theoretical background. I wish good luck to Guenole Jan, Rekha Rajaram, Li Gao, Bastiaan Bergman, and Cheng-han Yang for their successful completion of study.

I acknowledge the help of Andrew Kellock who performed the RBS measurements, Phil Rice who took the TEM images at Almaden and Titus Leo for TEM at Arizona State University.

Many thanks also to the Harris group members; Mark Wistey for his guidance to MBE system and Vincenzo Lordi for clean room fabrication teaching. The administrative skill of Gail Ghun-Creech at Stanford was invaluable.

I am grateful to Prof. David Miller for serving on my reading committee, and Prof. Calvin Quate, Prof. Philip Levis on my oral defense committee.

Finally I would like to thank my parents and my sister for years of support and encouragement.

DEDICATION

The author wishes to dedicate this dissertation to my lovely mother, Pansoon Gu.

TABLE OF CONTENTS

List of figures	xi
Chapter 1: Introduction	1
1.1 Spintronics – history and potential	1
1.2 Common Acronyms	3
Chapter 2: Magnetic tunnel junctions and experimental techniques	5
2.1 Magnetic Tunnel Junctions	5
2.1.1 Description of magnetic tunnel junctions	5
2.1.2. One dimensional free electron approximation for tunneling	10
2.2 Superconducting tunneling spectroscopy	13
2.2.1 Working principle of superconducting tunneling spectroscopy	13
2.2.2 Fitting analysis using Maki theory	16
2.4 Sample preparation	27
Chapter 3. Coherent tunnel barriers	29
3.1 High TMR from Fe/MgO(001)/Fe	29
3.2 TSP from (100) CoFe/MgO	34
3.3 TSP from CoFeB/(100) MgO	40
3.4 TSP from CoFe(B)/(111) MgO	43
3.5 AlN tunnel barriers	49
Chapter 4. NbN superconducting spin detector	53
4.1 The need for a new superconducting material for STS	53
4.2 STS using Ta, Nb, and NbN superconductors	55
Chapter 5. Kondo resonance in magnetic tunnel junctions	62
5.1 Kondo effect [93]	62
5.2 Kondo resonance in MTJs	67
Chapter 6. Impurity assisted resonant tunneling	77
6.1 Motivation	77
6.2 Voltage dependence of TMR	79
6.3 Resonant inversion of TMR from MgO/NiO(or CoO) barriers	82

Chapter 7. Conclusions & future work	90
7.1 conclusions.....	90
7.2 Suggestions for future directions	91
References.....	93

LIST OF FIGURES

Figure 2.1: One dimensional wave-function profile of quantum mechanical tunneling across an insulator between two metal electrodes.6

Figure 2.2: Simple illustration of the two states of a MTJ as used in a memory cell; parallel configuration (left) and antiparallel configuration (right). Parallel alignment of the two ferromagnetic electrodes gives a much higher current than the antiparallel configuration (for non-identical ferromagnetic electrodes or interfaces with the tunnel barrier, the AP state may, in rare cases, have a lower resistance value).6

Figure 2.3: (a) TMR versus field corresponding to a major hysteresis loop of an exchange biased MTJ, (b) same as (a) but for a minor loop, (c) TMR and junction resistance of P and AP states as a function of temperature, (d) Bias voltage dependence of TMR (blue curve) and junction resistance at 290K (P – black, and AP – red curves).....7

Figure 2.4: Density of spin-up ($\rho\uparrow$) and spin-down ($\rho\downarrow$) electrons, showing position of the Fermi energy E_F for one-band E_{F1} and two-band E_{F2} models of a ferromagnet. [18]11

Figure 2.5: One-dimensional tunneling simulation using the transfer matrix technique. A double barrier profile with two different barrier heights is used. The first barrier is assumed to be 2.3nm thick with the barrier height of 2eV. The second barrier height is 1eV and the thickness was changed. The molecular field was 0.3eV. The electron effective mass in the barriers are assumed to be 0.2 times free electron’s mass.11

Figure 2.6: Superconductor-Insulator-Ferromagnet tunneling at zero magnetic field. Left figure illustrates the DOS of a BCS superconductor and a ferromagnetic metal. Right figure shows the theoretical normalized conductance from such a junction.....15

Figure 2.7: Superconductor-Insulator-Ferromagnet tunneling at finite magnetic field. Left figure illustrates the DOS of a BCS superconductor and a

ferromagnetic metal. Right figure shows the theoretical normalized conductance from such a junction.....	15
Figure 2.8: Influence of orbital depairing parameter (a) and spin-orbit scattering parameter (b) on the theoretical conductance curve in a ferromagnetic metal / barrier / superconductor junction. The curves are calculated using an applied field of 2T, at a temperature of 0.25K. The values of ζ and b are indicated in the graph.....	18
Figure 2.9: Typical measured conductance versus voltage data for a Al/Al ₂ O ₃ /Co FIS junction and the corresponding fitted curve derived using Maki theory.	20
Figure 2.10: Energy diagram of a tunneling junction showing elastic and inelastic tunneling processes. [40]	23
Figure 2.11: Illustration of an I - V curve, and corresponding conductance and derivative of conductance versus V curves (the latter corresponds to what is termed the inelastic tunneling spectrum - IETS).....	23
Figure 2.12: IETS measurement scheme for a MTJ. The complex filter scheme is not shown.	25
Figure 2.13: Conductance and IETS measurement from CoFe/ Al ₂ O ₃ barrier/ CoFe junction at 2.6K. Red corresponds to the parallel configuration and black indicates the antiparallel configuration.	26
Figure 2.14: Schematic of the sputtering system (left image). Shadow masking is used to define the electrodes and barriers. In the middle a typical deposited wafer and on the right hand side an SEM picture of one of the junctions is shown.	28
Figure 3.1: Majority (top), minority (middle), and antiparallel (bottom) conductance versus the crystal momentum in the film plane for a (100) Fe/8ML MgO/Fe structure. [57]	30
Figure 3.2: Tunneling density of states (TDOS) of the majority and minority channels at $k_{\parallel}=0$ from Fe(100)/8ML MgO/Fe(100). [57]	32
Figure 3.3: Transmission electron micrographs of an STS film with the structure of Ta/IrMn/CoFe/MgO/AlSi. The image is courtesy of Titus Leo, Arizona State University.....	35

Figure 3.4: The contact resistance change of top AlSi electrode versus AlSi thickness. The structure is Ta/IrMn/CoFe/MgO(100)/AlSi.....	36
Figure 3.5: Conductance versus applied voltage curves of unannealed and after annealing for various AlSi thicknesses. The annealing temperature is indicated in the figure.	37
Figure 3.6: Tunneling spin polarization of the Fe/MgO interface versus Mg underlayer thickness for various annealing temperature. The structure is Ta/IrMn/CoFe/xMg/MgO (100)/AlSi.....	38
Figure 3.7: Tunneling spin polarization of the Co ₇₀ Fe ₃₀ /MgO interface versus annealing temperature measured from STS studies at 0.25 K.....	39
Figure 3.8: Conductance versus applied voltage curves showing 90% tunneling spin polarization from STS measurements. The fitting parameters of the STS measurement are shown in the figure.	39
Figure 3.9: TMR versus field curves at (a, b: major loop) 2.6 K and (c, d: minor loop) 290K for an exchanged biased magnetic tunnel junction with a highly (100) textured MgO tunnel barrier.....	40
Figure 3.10: Tunneling spin polarization from CoFeB (12%)/MgO versus Mg underlayer thickness.....	41
Figure 3.11: Tunneling spin polarization from CoFeB (15%)/MgO versus Mg underlayer thickness.....	41
Figure 3.12: Tunneling spin polarization from CoFeB (20%)/MgO versus Mg underlayer thickness.....	42
Figure 3.13: TEM images with low (upper panel) and high magnification (lower panel) for the following MTJ structure: 50Ta / 150Pt / 250IrMn / 25CoFe / 40MgO / 100CoFe / 100TaN (in Å). The high magnification image reveals that CoFe grows (110) oriented on the (111)IrMn and the MgO layer has a (111) texture. The image is courtesy of Phil Rice, IBM Almaden Research Center.....	44
Figure 3.14: TSP versus Mg underlayer thickness for (100) and (111) MgO orientation. The structure is Ta, Pt or Cu/250 IrMn/ 3CoFeB/60CoFe /xMg/MgO/40AlSi (in Å).	45

Figure 3.15: TSP versus MgO barrier thickness for (100) and (111) MgO orientation. ...	45
Figure 3.16: TMR of MTJs with (111) textured MgO barriers: (a) R_p , R_{AP} , and TMR versus temperature. (b) Bias dependency (b) and major (c) and minor (d) loops of samples showing the maximum TMR found.	46
Figure 3.17: IETS of the (111) textured MgO from same sample as Figure 3.16 at 2.7K.	48
Figure 3.18: IETS from the sample of CoFe/(100)MgO/CoFe at 2.8K.	48
Figure 3.19: XTEM of MTJ with AlN tunnel barrier. The structure is 100Ta/250IrMn/ [50CoFe/x AlN] ₅ (in Å).	50
Figure 3.20: TSP from AlN barrier with different electrodes. The sample structure is 45 AlSi/34 AlN/electrodes or 45 AlSi/1.5 Al ₂ O ₃ /22 AlN/electrodes (in Å)....	51
Figure 3.21: Tunneling spin polarization and magnetic moment per atom for different...	51
Figure 3.22: IETS data at 2.5 K from an MTJ with the structure of 40 CoFe/45 AlN/200 CoFe (in Å). The signal from P and AP states is almost identical due to small TMR effect.	52
Figure 3.23: TSP data from MgO/Al ₂ O ₃ hybrid barrier. Each barrier thickness is inserted in the figure (in Å).	52
Figure 4.1: Conductance data from Ta/ IrMn/ CoFe/ MgO/ 4.5nm Al at 0.25K for various magnetic fields (left) and at a fixed field of 3T with various temperatures (right).....	54
Figure 4.2: Periodic table showing superconducting transition temperatures of the elements.	54
Figure 4.3: Superconducting energy gap $\Delta_1 + \Delta_2$ from tunneling spectroscopy data at zero field and 0.25 K versus NbN thickness for x nm NbN/MgO/ x nm NbN tunnel junctions. Δ_1 (Δ_2) corresponds to the energy gap of the bottom (top) NbN electrode. The inset shows a typical conductance versus bias voltage curve for x= 116nm.	56
Figure 4.4: The critical temperature of NbN layers. When NbN is used as a top electrode in an FIS structure, it shows a maximum T_c . The inset shows the resistance of NbN layer versus temperature.	57

Figure 4.5: Normalized conductance versus bias voltage curves (symbols) and fits (solid lines) for various superconducting counter-electrodes: (a) as-deposited (no anneal) Ta/IrMn/CoFe/MgO/7.5nm NbN junctions at 6T and 0.245K – fit without strong-coupling parameter ($\Gamma=0$), (b) same as (a) but fit with $\Gamma= -0.05$, (c) same as (a) but measured at 8T and 1.2K and fit with $\Gamma= -0.025$, (d) as-deposited Ta/IrMn/CoFe/MgO/5nm Nb junctions at 6T and 0.25K, data fitted with $\Gamma= -0.08$, (e) same as (d) but measured at 1.2K and fit with $\Gamma= -0.1$, and, (f) as-deposited Ta/IrMn/CoFe/MgO/10nm Ta junctions at 2T and 0.25K, data fitted with $\Gamma= -0.013$.	58
Figure 4.6: Conductance data from Ta/ IrMn/ CoFe/ MgO/ 7.5nm NbN junctions at 0.25K for various magnetic fields (left) and at a fixed field of 8T with various temperatures between 0.25 and 1.6 K (right).	60
Figure 4.7: The fitted magnetic field is plotted as a function of the applied field at 0.25K and 1.2K for the devices of Figure 4.6. The solid line in the inset corresponds to the fitted field equal to the applied field.	60
Figure 5.1: (a) Temperature dependence of resistance from different metals. (b) Conductance enhancement due to Kondo assisted tunneling. (c) Metals with magnetic impurities have lots of scattering centers, which increases the resistance at low temperature. (d) Kondo resonance in a double tunnel junction device. [93]	63
Figure 5.2: The Anderson model of a magnetic impurity with one electron energy level (ϵ_0), showing effective spin flipping due to quantum mechanical tunneling. Right figure shows the Kondo resonance due to many such tunneling events. [93].	65
Figure 5.3: (a) Previous studied Kondo examples. (b) Simple device diagram with Kondo resonance state. (c) Conductance enhancement due to Kondo effect. [94].	66
Figure 5.4: Schematic illustration of magnetic tunnel junctions with transmission electron micrographs (TEM). In this work double magnetic tunnel junctions are comprised of 100 Ta / 250 IrMn/ 35 Co ₇₀ Fe ₃₀ / 25 MgO/ X Co ₇₀ Fe ₃₀ / 25 MgO/ 70 Co ₇₀ Fe ₃₀ / 150 IrMn/ 100 Ta, where all thicknesses	

in angstroms (Å). Active tunnelling area is $\sim 700\mu\text{m}\times 700\mu\text{m}$. (a) When middle CoFe thickness is above 10 Å. (b) TEM shows continuous layer of 10 Å CoFe. (c) When middle CoFe thickness is less than 10 Å, nanoparticles are formed. (d) scanning TEM (STEM) of 2.5 Å CoFe layer. (e) STEM image of 7.5 Å CoFe layer. (f) Electron Energy-Loss Spectroscopy data from 7.5 Å CoFe layer.....68

Figure 5.5: Signature of Coulomb blockade and TMR suppression in a DTJ. Magnetic fields of -500 and +10,000 Oe were applied to set the state of the junction in the AP and P states, respectively. Single tunnel junctions were prepared with same method as DTJ, consisting of 100 Ta / 250 IrMn/ 35 Co₇₀Fe₃₀/ 28 MgO/ 70 Co₇₀Fe₃₀/ 100 Ta, where thicknesss are in Å. TMR, typically defined as $(R_{\text{AP}}-R_{\text{P}})/R_{\text{P}}$, where R_{AP} and R_{P} are the resistances for anti-parallel (AP) and parallel (P) alignment of the magnetic moments, respectively. (a) R_{P} change of STJ with temperature and bias. (b) R_{AP} change with temperature and bias. (c) corresponding TMR of STJ shows highest value at low temperature and zero bias. (d) R_{P} change with temperature and bias of DTJ with 4.5 Å thick middle CoFe layer. (e) R_{AP} change with temperature and bias of same DTJ. (f) TMR of DTJ shows a dip at low temperature and low bias.70

Figure 5.6: (a) Field cooled and zero field cooled magnetization versus temperature for 5Å thick CoFe middle layers in MgO based MTJs. (b) DC resistance at zero bias vs temperature for different thicknesses of the CoFe middle electrode and consequently, the nanoparticle size. Open (filled) symbols correspond to R_{P} (R_{AP}). (c) Differential conductance with 5Å middle electrode at 2.5 K. (d) Maximum excess conductance ratio with 2Å middle electrode is calculated from $(G_{\text{v}}-G_{\text{o}})/G_{\text{o}}$, where G_{v} is experimental conductance data at zero bias and G_{o} is the minimum of fitted background. This excess conductance of DTJ is saturated to a maximum value well below T_{K} . The line is a fit of the excess G as a function of temperature using the formula $G_{\text{K}}(T)=G_{\text{o}}/1+(2^{1/s}-1)T^2/T_{\text{K}}^2)^s$, yielding $T_{\text{K}}=76\text{K}$ and $s=2.48$71

Figure 5.7: Nanoparticle size of middle CoFe layer effect. (a) Kondo temperature (T_K), defined by three different methods. (b) The maximum TMR and TMR suppression ratio change with the size of nanoparticles. TMR suppression ratio is defined by the ratio between maximum TMR and TMR at zero bias. (c) TMR suppression evolution with temperature. (d) TMR and magnetization as a function of magnetic field from 100 MgO 150 Ta 40 CoFe 23 MgO 5 CoFe 23 MgO 150 Ta.....	73
Figure 5.8: Measured conductance at 2.5K with different middle CoFe layer thicknesses.	75
Figure 6.1: TEM images with low (upper panel) and high magnification (lower panel) for the following MTJ structure: IrMn 60 CoFe(70/30) 8 Mg 25 MgO 10 NiO 25 CoFe(70/30) (in Å). The image is courtesy of Titus Leo, Arizona State University.....	78
Figure 6.2: The voltage and temperature dependence of TMR from an MTJ with a structure of CoFe/MgO/4Å NiO/CoFe.	78
Figure 6.3: Bias dependence of TMR (left column) and IETS data (right column) from an MTJ with a structure of CoFe/yMgO/x NiO/CoFe ($x+y=27\text{Å}$). All the samples are unannealed.....	84
Figure 6.4: (a) Voltage dependence of TMR from a sample of CoFe/4Å NiO/25Å MgO/CoFe at 290K. (b) Voltage dependence of TMR from a sample of CoFe/12Å MgO/4Å NiO/12Å MgO/CoFe at 2.8K. (c) Temperature dependence of TMR and junction resistance at zero bias from the same sample as (b). (d) IETS data from the same sample as (b) at 2.8K.	86
Figure 6.5: Voltage dependence of the TMR and IETS from an MTJ with a barrier of MgO/4 Å NiO annealed at 260°C (a, b) and 400°C (c, d).....	87
Figure 6.6: (a) IETS from the barrier of 20Å MgO/16Å NiO, (b) IETS from the barrier of 56Å NiO, (c) IETS from the barrier of 24Å MgO/8Å CoO and 22Å MgO/12Å CoO, (d) Voltage dependence of TMR with different CoO thickness.....	88

Chapter 1: Introduction

1.1 Spintronics – history and potential

The astonishing growth of digital data in recent years has resulted in the explosive growth of all sorts of solid state memory devices and magnetic hard disk drive storage devices. The growth in data storage has been driven by a multiplicity of new and very cheap portable electronic devices for consumers, especially, MP3 players for audio and video playback, and digital cameras, as well as cellular phones and personal digital assistants (PDAs). In the coming years, portable systems will require ever more nonvolatile data storage capabilities, both for audio and video applications, which require very high storage capacities in the smallest possible volume, but without necessarily either high performance nor high data fidelity, as well as new applications which might arise if cheap and high density memory storage devices are developed which have sufficiently high access times for computing applications. Even though hard disk drives are by far the largest and cheapest nonvolatile media among currently available technology products (with the exception of magnetic tape which is still cheaper but which is much too slow for most consumer applications) hard disk drives consume more power than solid state memories and are inherently less reliable due to the mechanical nature of the technology. Therefore, there have been tremendous efforts to make new types of nonvolatile solid state memories which combine the best features of static random access memory (SRAM; high speed - tens of ns reading and writing time-) and dynamic random access memory (DRAM; very high density and consequent low cost). Other important specifications include high endurance of solid state memories (typically more than a 10 year lifetime and more than 10^{12} reading and writing cycles) as well as being integrable with the conventional complementary metal oxide semiconductor (CMOS) processes in order to take advantage of CMOS based logic capabilities. Intrinsically low power consumption and low cost per bit are also important issues. If we could develop such a new type of memory, in addition to the merit of the memory itself, it would be possible to vastly

simplify computing systems and their software which today are obliged, for cost and performance reasons, to transfer and manage data between many different types of semiconductor memories and the hard disk drive itself.

Solid state memories can be divided into three classes based on their working principles; the first group, such as Ferroelectric Random Access Memory (FRAM) and FLASH memory, use the quantity of stored charge. The second approach, resistive memories, is based on the quantity of charge flowing: these include phase change memories based various materials including polymers, perovskites and chalcogenide glasses. Perhaps the final class is those memories which use the spin degree of freedom of the electron such as magnetic random access memory (MRAM). Concepts of spin engineering began almost 20 years ago with the discovery of giant magnetoresistance (GMR) in metal thin film multilayers [1] and subsequently developed in the late 80s and 90s into an intensive research field often termed “spintronics”. Magnetic sensors based on spin-valve GMR sandwiches with artificial antiferromagnetic reference layers have resulted in enormous increases in the storage capacity of magnetic hard disk drives. [2] The unique properties of magnetic tunnel junctions (MTJ) devices, such as much larger magnetoresistance (MR) values and perpendicular current flow, have led to the development of high performance nonvolatile MRAM as well as magnetic field sensors for high density hard disk drive read heads.[3-5] In the current cross-point MRAM architectures, each MTJ, corresponding to a single bit storage cell, is located at the crossing point between a word line and a bit line. The magnetic bit is designed to have two stable operation points (Parallel (P) and Anti-Parallel (AP) configurations), where two different resistance values represent “0” or “1”.

The focus of this dissertation is a deep understanding of the phenomenon of spin polarized tunneling in MTJs. Chapter 2 begins by describing the details of the experimental techniques used subsequently in this thesis. Details of the sputtering growth procedures as well as DC and AC spectroscopy techniques are discussed. AC techniques include superconducting tunneling spectroscopy (STS) to measure tunneling spin polarization (TSP) and inelastic electron tunneling spectroscopy (IETS) to detect local energy excitations.

In order to achieve sufficiently high density and stable operation of MRAM, the resistance difference between parallel and anti-parallel configurations of the MTJ storage cells must be sufficiently large. This can be achieved by the generation of highly spin polarized current flowing in the MTJ device. Chapter 3 deals with MTJs which exhibit extremely high tunneling spin polarization (~90%) by using novel tunnel barriers formed from highly oriented crystalline MgO (100) yet which are formed by relatively simple magnetron sputter deposition techniques at ambient temperature.

Chapter 4 discusses the development of a novel high temperature superconducting electrode (NbN) for STS, which enables the measurement of TSP at temperatures as high as 1.2K (about 4 times higher than was previously possible). Until now nearly all STS studies have used low temperature aluminum superconducting electrodes which necessitate the use of ³He cryostats.

One of the most interesting phenomena in tunneling devices is resonant tunneling effect. Depending on the energy and strength of the density of states in the metal electrodes and impurity states in the tunnel barrier of the tunneling device, resonant tunneling can be a dominant tunneling mechanism, for certain bias voltage and temperature regimes. Kondo resonance assisted tunneling at the Fermi level is discussed in Chapter 5, and impurity assisted resonant tunneling is presented in Chapter 6.

1.2 Common Acronyms

All of the acronyms are defined in the text of this dissertation. It is however, useful to have a single source of the common acronyms and definitions, as listed here.

AFM	Antiferromagnetic material
AP	Antiparallel magnetic configuration of two magnetizations
AR	Andreev reflection
CIP	Current in plane
CPP	Current perpendicular to plane

DOS	Density of states
FIS	Ferromagnet/insulator/superconductor
FM	Ferromagnet or Ferromagnetic material
G	Differential conductance (dI/dV)
GMR	Giant magnetoresistance
I	Insulating barrier
IETS	Inelastic electron tunneling spectroscopy
IV	Current-Voltage curve
MR	Magnetoresistance
MRAM	Magnetic random access memory
MTJ	Magnetic tunnel junction
P	Parallel magnetic configuration of two magnetizations
PCAR	Point contact Andreev reflection
SC	Superconductor
SEM	Scanning electron microscope
SP	Spin polarization
SQUID	Superconducting quantum interference device
STS	Superconducting tunneling spectroscopy
TMR	Tunneling magnetoresistance
TSP	Tunneling spin polarization
UVOCS	Ultra violet ozone cleaning system
VBS	Virtual bound state
XPS	X-ray photoelectron spectroscopy
XTEM	Cross-section transmission electron microscopy

Chapter 2: Magnetic tunnel junctions and experimental techniques

2.1 Magnetic Tunnel Junctions

2.1.1 DESCRIPTION OF MAGNETIC TUNNEL JUNCTIONS

Magnetic tunnel junctions (MTJs) consist of two ferromagnetic (or ferrimagnetic) metal layers (FM) separated by a thin ($\sim 20\text{\AA}$) insulating barrier (I). In MTJs current can flow between the electrodes upon application of a bias voltage due to quantum mechanical tunneling through the barrier, as the wave-function profile illustrates in Figure 2.1. The resistance of the structure depends on the relative orientation of the magnetization of the two ferromagnetic electrodes, in either parallel (P) or antiparallel (AP). The tunneling magnetoresistance (TMR), in this work, is defined as

$$TMR = \frac{\Delta R}{R_L} \quad (2.1)$$

where ΔR is the difference in the resistance between the antiparallel and parallel magnetic states, and R_L is the lowest resistance state of the device. For conventional ferromagnetic metals (e.g. Co, Fe, and Ni) the resistance is higher when the magnetizations of the two electrodes are antiparallel as compared to the parallel alignment, as illustrated in Figure 2.2.

The simplest way to realize the AP state in a MTJ is to use two ferromagnetic layers with different coercive fields. Exchange biasing is another method. In this case one of the magnetic electrodes is placed in direct contact with an antiferromagnetic (AFM) material, such as NiO or IrMn. The presence of unidirectional exchange anisotropy at the AFM/FM interface shifts the center of its magnetization versus field loop away from zero

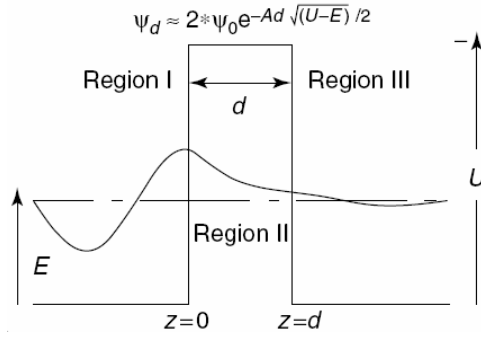


Figure 2.1: One dimensional wave-function profile of quantum mechanical tunneling across an insulator between two metal electrodes.

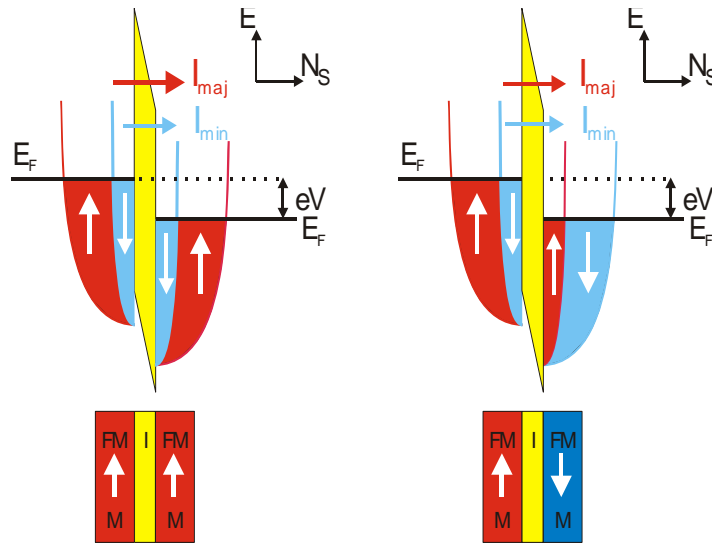


Figure 2.2: Simple illustration of the two states of a MTJ as used in a memory cell; parallel configuration (left) and antiparallel configuration (right). Parallel alignment of the two ferromagnetic electrodes gives a much higher current than the antiparallel configuration (for non-identical ferromagnetic electrodes or interfaces with the tunnel barrier, the AP state may, in rare cases, have a lower resistance value).

field, as shown in Figure 2.3(a), where the electrode, which is exchange biased, has its magnetization loop centered at ~ 80 Oe. The relative field directions of the exchange biased layers of the pinned layer (red) and the free layer (blue) are indicated with colored arrows in the graph. The magnetic field sweep direction is indicated by the black arrows.

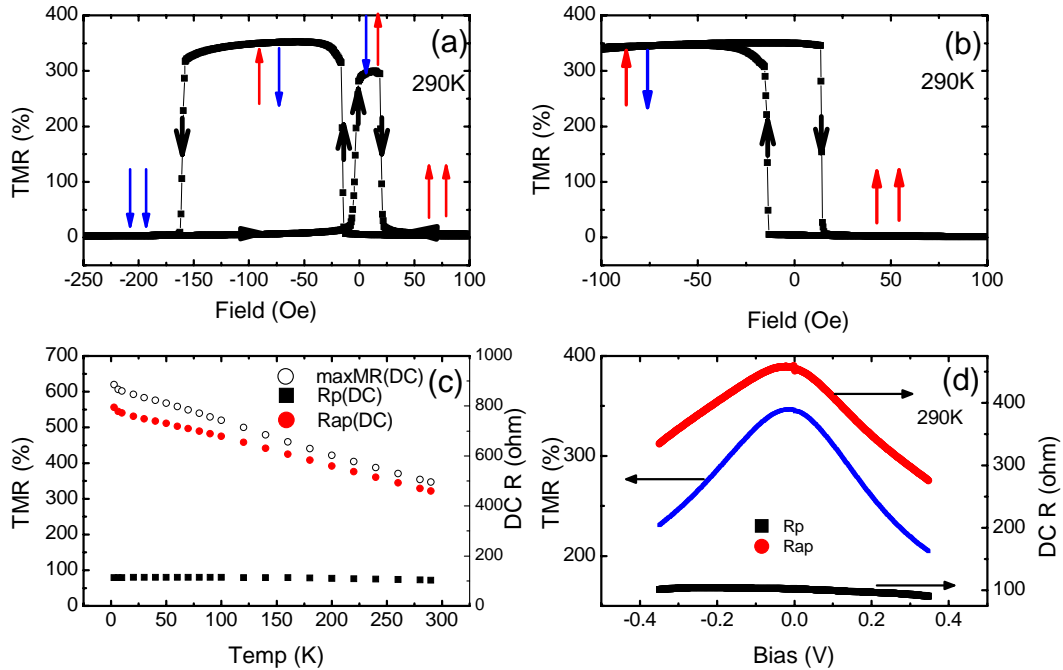


Figure 2.3: (a) TMR versus field corresponding to a major hysteresis loop of an exchange biased MTJ, (b) same as (a) but for a minor loop, (c) TMR and junction resistance of P and AP states as a function of temperature, (d) Bias voltage dependence of TMR (blue curve) and junction resistance at 290K (P – black, and AP – red curves).

In most MTJs the magnitude of the TMR decreases strongly with both increasing bias voltage and temperature as shown in Figure 2.3(c) and (d). It is generally believed, but yet not clear, that increased contributions from magnons, magnetic impurities, localized trap states, and the modified electronic structure at elevated bias and temperature are responsible for these effects. Two step tunneling through localized defect states in the barrier, which mainly increase the conductance of the minority spins [6], might be the key to understand the voltage and temperature dependence [7]. The temperature dependence of TMR can be accounted for by a decrease in interfacial spin polarization and magnetization due to spin wave excitations. [8, 9] The voltage dependence of TMR will be discussed in detail in Chapter 6. Interestingly, by engineering and controlling defect states in the barrier, defect mediated tunneling can become the dominant tunneling mechanism: this is an important topic in this thesis. An interesting property of magnetic tunnel junctions is the weak temperature and bias dependence of tunneling current in the *parallel* state configuration as shown in Figure 2.3(c) and (d). This suggests that thermal

energy variation from low temperature ($< 4\text{K}$) to room temperature has little effect on the tunneling characteristic between metals across wide band gap insulators.

The first successful magnetic tunnel junction was prepared by Julliere in the early 70s [10]. Julliere used Co and Fe as electrode materials and Ge as the insulating barrier, which was oxidized after deposition. A resistance change as high as 14% was observed at low temperatures and at very low bias (a few mV). After the initial discovery of tunneling magnetoresistance in an MTJ, other tunnel barriers (e.g. NiO [11] and Gd_2O_3 [12]) were explored, but only small effects ($< 7\%$ at 4.2K) were observed. In 1995, two different groups (Moodera [3] and Miyazaki [4]) prepared MTJs using amorphous Al_2O_3 barriers and achieved TMR values much higher than previously reported (18% at room temperature and 30% at 4.2K, respectively). These results sparked tremendous interest and research on magnetic tunnel junctions, largely due to their promising applications in recording read heads for hard disk drives and novel magnetic random access memories. [5]

As proposed by Julliere [10], the tunneling current between two ferromagnets can be described as follows for the P and AP configurations:

$$I_P \approx N_{\uparrow}^1 N_{\uparrow}^2 + N_{\downarrow}^1 N_{\downarrow}^2 \quad (2.2)$$

$$I_{AP} \approx N_{\uparrow}^1 N_{\downarrow}^2 + N_{\downarrow}^1 N_{\uparrow}^2 \quad (2.3)$$

where $N_{\downarrow\uparrow}^{1,2}$ are the density of down- and up-spin states at the Fermi energy for the two ferromagnetic electrodes (1 and 2).

The magnitude of the TMR can then be written as:

$$TMR = \frac{I_P - I_{AP}}{I_{AP}} = \frac{2P_1 P_2}{1 - P_1 P_2} \quad (2.4)$$

where $P_i = \frac{N_{\uparrow}^i - N_{\downarrow}^i}{N_{\uparrow}^i + N_{\downarrow}^i}$, $i = 1, 2$ is the spin polarization (SP) of the left or right electrodes.

With this definition, the SP calculated from Julliere's TMR value was about 26%. The spin polarization of tunneling current can be directly measured by replacing one of the F layers with a superconducting material, as discussed later in this chapter (section 2.2). Meservey and Tedrow first used such a technique of superconducting tunneling spectroscopy to measure the SP of electrons tunneling through Al_2O_3 from a variety of ferromagnetic 3d metals. Using superconducting layers of Al, they reported a SP of 44% from Fe [13]. However, they overestimated the value of SP because they ignored spin-orbit corrections [14]. Many years later the IBM group reported a SP of 55% from a NiFe alloy [14], the maximum value yet observed using amorphous Al_2O_3 tunnel barriers, likely due to improved deposition techniques and consequently better interfaces. Results for Co and Ni are inconsistent with the bulk band structure of these strong ferromagnetic metals, for which the dominant tunneling contribution is predicted to be from minority spin-polarized states at the Fermi energy, so leading to a negative SP as compared to the measured positive SP.

This inconsistency between the experimental and theoretical values of the SP is the consequence of the fact that the tunneling SP depends not only on the density of states at the Fermi energy but also on the tunneling matrix elements which depend on the symmetry of the electronic states. Stearns suggested that the tunneling matrix element varies in an inverse manner with the effective mass of the electrons: localized d-electrons have much higher effective masses than the highly dispersive s-electrons and consequently tunnel less probably. [15] Therefore, assuming that the dominant tunneling is due to the DOS of the free-electron-like dispersive s-bands at the Fermi energy, which is proportional to their Fermi wave-vector, we can write the SP as follows:

$$P_i = \frac{k_{\uparrow}^i - k_{\downarrow}^i}{k_{\uparrow}^i + k_{\downarrow}^i}, i = 1, 2 \quad (2.5)$$

where k^{\uparrow} and k^{\downarrow} are the Fermi wave-vectors of the dispersive bands for the majority and minority spins. The SP of Ni on this basis is 10%, consistent with the early experimental

data. Although Stearns developed the notion of ‘tunneling DOS’ only including the effective number of electrons, in which the nearly free-electron-like s-d hybridized bands are assumed to provide essentially all of the tunneling current, the method of interpreting TMR in terms of the intrinsic properties of ferromagnets was largely unchanged.

De Teresa et al. demonstrated that the insulating barrier material can strongly influence and even change the sign of the spin polarization of tunneling electrons using SrTiO₃ barriers. [16] Recently, extremely high TMR values, of up to 220% at room temperature, have been reported in practical MTJ devices with highly oriented crystalline MgO(100) tunnel barriers. [17] Consequently, this new type of barrier, MgO, demonstrates an extremely high tunneling spin polarization (~90%), which cannot be explained solely by the role of the ferromagnet’s spin polarization, as suggested above. It is obvious, therefore, that the tunneling SP is determined not only by the ferromagnet, but also by the structural and electronic properties of the barrier, including the interfaces between the ferromagnets and the insulator.

2.1.2. ONE DIMENSIONAL FREE ELECTRON APPROXIMATION FOR TUNNELING

A more accurate theoretical description of spin polarized tunneling was first proposed by Slonczewski [18]. He considered two identical ferromagnets separated by a rectangular potential barrier and assumed that the electronic structure of the ferromagnetic electrodes can be described by two parabolic bands shifted in energy due to the exchange spin splitting, as shown in Figure 2.4. In the free-electron approximation of the spin polarized conduction electrons inside each ferromagnet, the longitudinal part of the effective one-electron Hamiltonian may include an internal exchange energy term, $-\mathbf{h} \cdot \boldsymbol{\sigma}$ in addition to the kinetic energy and potential energy terms, where $-\mathbf{h}$ is the molecular field and $\boldsymbol{\sigma}$ is the conventional Pauli spin operator. Here the effective SP of the tunneling electron is given by:

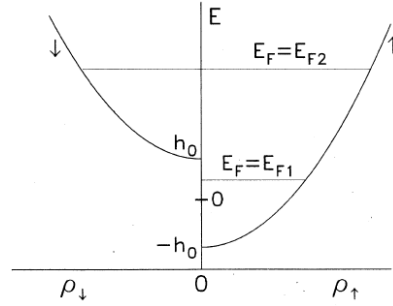


Figure 2.4: Density of spin-up ($\rho\uparrow$) and spin-down ($\rho\downarrow$) electrons, showing position of the Fermi energy E_F for one-band E_{F1} and two-band E_{F2} models of a ferromagnet. [18]

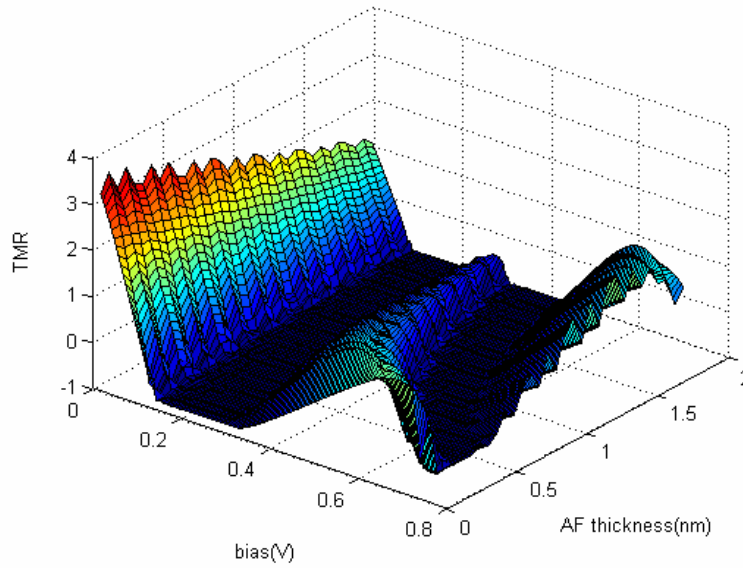


Figure 2.5: One-dimensional tunneling simulation using the transfer matrix technique. A double barrier profile with two different barrier heights is used. The first barrier is assumed to be 2.3nm thick with the barrier height of 2eV. The second barrier height is 1eV and the thickness was changed. The molecular field was 0.3eV. The electron effective mass in the barriers are assumed to be 0.2 times free electron's mass.

$$P_i = \frac{k_{\uparrow}^i - k_{\downarrow}^i}{k_{\uparrow}^i + k_{\downarrow}^i} \frac{\kappa^2 - k_{\uparrow}^i k_{\downarrow}^i}{\kappa^2 + k_{\uparrow}^i k_{\downarrow}^i}, \quad i=1,2 \quad (2.6)$$

where κ is the wave-function decay constant into the barrier which is determined by the potential barrier height. The tunneling current through an insulator, to first order, depends

on the barrier height and thickness of the insulator. The barrier height is related to the energy difference between the Fermi energy and the bottom of the conduction band of the insulator. In the case of a high barrier, it results in Julliere's formula. However, if the barrier is not very high and the decay ratio is comparable to the wave-vectors of electrons in the ferromagnets, the TMR decreases with decreasing barrier potential and even changes sign for sufficiently low barriers. This indicates that the tunneling SP is not an intrinsic property of the ferromagnets, but depends on the electrodes and barrier.

One of the techniques which can be used to solve one-dimensional quantum mechanical problems is the transfer matrix technique. To determine the fraction of incident particles that are transmitted by the barrier, a continuously-varying potential is modeled by a step-wise potential. Once we apply boundary conditions to the incident, reflected, and transmitted wave-functions inside each layer and at the interface, tunneling rates can be calculated in terms of the overall transfer matrix. Please refer to the applied quantum mechanics class notes from Prof. David Miller for more details. One typical example of this type of calculation is shown in Figure 2.5, for a double barrier as the thickness of one barrier is changed.

Although free electron models capture some important features of spin dependent tunneling in MTJs, they are limited. Free electron models ignore the multi-band electronic structure of the ferromagnetic electrodes and the interface between the ferromagnets and the insulator, as well as the complex band structure of the insulator. Free electron models are very sensitive to the profile of the potential barrier. Actual tunnel junctions contain a large amount of disorder in the electrodes, in the barrier, and at the interfaces between the electrodes and barrier. Interdiffusion, interface roughness, and impurity and defects can dramatically affect TMR by changing the electronic and atomic structure, modifying the barrier profile, or by assisting tunneling processes. [6]

2.2 Superconducting tunneling spectroscopy

2.2.1 WORKING PRINCIPLE OF SUPERCONDUCTING TUNNELING SPECTROSCOPY

Many aspects of the TMR phenomenon are poorly understood although it is clear that the fundamental origin of TMR is the spin polarization of the tunneling current. Thus, the measurement of the magnitude and sign of the tunneling spin polarization (TSP) is very important to help further our understanding of TMR. [10] The spin polarization can be probed by a variety of techniques, including photoemission [19, 20], point contact Andreev reflection [21] and superconducting tunneling spectroscopy (STS) [22]. Photoemission experiments determine the unweighted density of states (DOS) at the Fermi-energy and, therefore, for the 3d transition metal ferromagnets are sensitive mainly to the contribution of the d-electrons, whereas most of the tunneling current is due to electrons from the more extended sp-bands. [23] Andreev reflection measures the magnitude (but not the sign) of the polarization of electrons at a diffusive interface between the ferromagnetic metal and a superconductor, whereas MTJs involve electrons tunneling across a thin dielectric layer. The STS technique uses a superconducting electrode (S) in the presence of a large magnetic field to detect both the magnitude and sign of the spin polarization of current tunneling from a ferromagnetic electrode (F) at the Fermi energy across an insulating layer (I) in FIS junctions. Thus, STS is clearly the technique most closely related to spin dependent tunneling in MTJs. Thus, the TSP, taking into account spin dependent transmission matrix elements, M , can be written as

$$TSP_i = \frac{M_{\uparrow}^i N_{\uparrow}^i - M_{\downarrow}^i N_{\downarrow}^i}{M_{\uparrow}^i N_{\uparrow}^i + M_{\downarrow}^i N_{\downarrow}^i}, i = 1,2 \quad (2.7)$$

The STS technique was first developed by Meservey and Tedrow using aluminum superconducting electrodes in 1971 [22] and has been applied to many ferromagnetic and ferrimagnetic metals including the 3d transition metals and many of their alloys [24], the rare-earth metals [22] and rare-earth-metal transition-metal alloys [25].

Giaever first showed that electron tunneling experiments can be used to probe the superconducting DOS [26], theoretically justified by Bardeen, Cooper, and Schrieffer (BCS) [27]. On the basis of Fermi's golden rule [28], the number of tunneling electrons is given by the product of the density of filled states at a given energy in one electrode and the density of empty states in the other electrode at the same energy multiplied by the square of a matrix element describing the probability of tunneling. The total current is given by:

$$I(eV) \sim |M|^2 \int_{-\infty}^{\infty} N_1(E + eV) N_2(E) [f(E + eV) - f(E)] dE \quad (2.8)$$

where V is the voltage at the first electrode with respect to the second, N is the DOS of the electrodes, and f is the Fermi function, and the energy E is measured from the Fermi energy. When one electrode is superconducting and the other is a normal metal, assuming that the matrix element is independent over the energy range of a typical STS measurement (i.e. within a few meV) and the DOS of the normal metal is also constant over this energy range, the total current becomes:

$$I(eV) \sim |M|^2 N_n \int_{-\infty}^{\infty} N_s(E) [f(E + eV) - f(E)] dE \quad (2.9)$$

where N_s , the BCS DOS for superconductor, has a gap between $\pm\Delta$ and characteristic singularities at the energy of $\pm\Delta$. Thus little current flows when $|eV| < \Delta$ because there are only a few available states in the superconducting electrode. When the bias voltage (eV) exceeds the gap energy, the current increases very rapidly. Once we take the derivative of equation (2.9) and after removing constant terms, the conductance can be written in the following form:

$$\frac{dI}{dV}(eV) \sim \int_{-\infty}^{\infty} N_s(E) f'(E + eV) dE \quad (2.10)$$

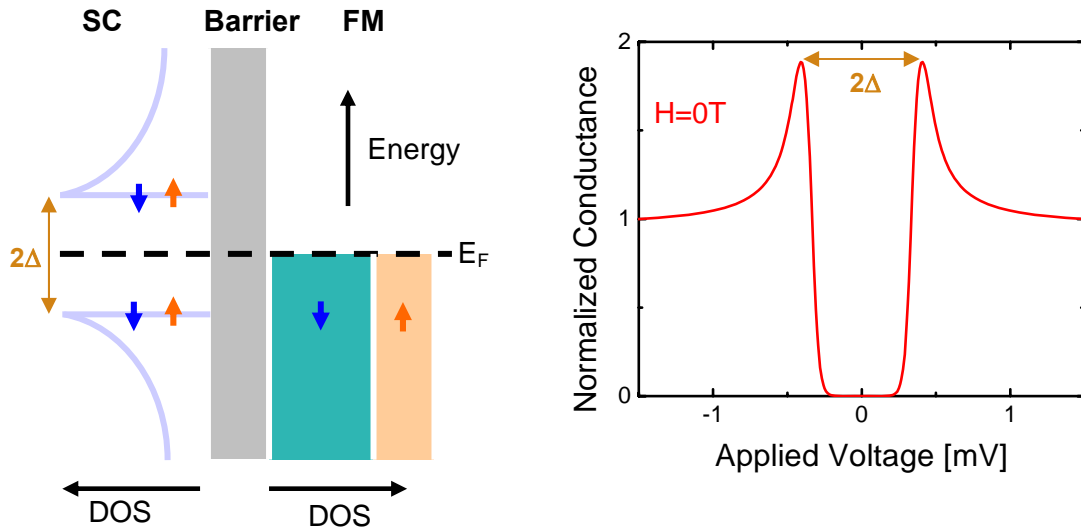


Figure 2.6: Superconductor-Insulator-Ferromagnet tunneling at zero magnetic field. Left figure illustrates the DOS of a BCS superconductor and a ferromagnetic metal. Right figure shows the theoretical normalized conductance from such a junction.

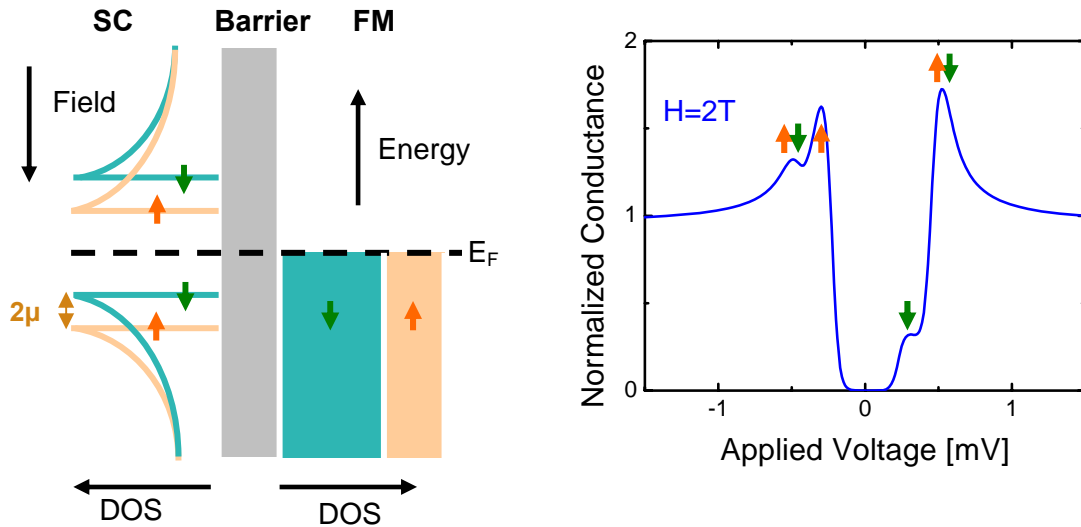


Figure 2.7: Superconductor-Insulator-Ferromagnet tunneling at finite magnetic field. Left figure illustrates the DOS of a BCS superconductor and a ferromagnetic metal. Right figure shows the theoretical normalized conductance from such a junction.

where f' is the derivative of the Fermi function with respect to eV . At low temperatures, f' approaches a δ function and a measurement of the conductance closely resembles the

density of states in the superconductor. In zero magnetic field, the conductance curve from a Superconductor-Insulator-Ferromagnet (SIF) junction mimics the DOS of the superconducting layer as shown in Figure 2.6, which is similar to measurements from non-ferromagnetic metals.

Figure 2.7 illustrates the superconducting density of states in a magnetic field as well as the conductance of a SIF junction. Note the Zeeman splitting displaces the spin up and spin down DOS peaks of the superconductor by $2\mu_B H$. The conductance curve now has four peaks with the peak height being asymmetric with respect to zero bias. Note that the inner two peaks contain predominantly one spin component, either up or down. The degree of the asymmetry between these two peaks is a measure of the tunneling SP from the ferromagnet.

2.2.2 FITTING ANALYSIS USING MAKI THEORY

For many years, the determination of TSP was based simply on using four values of the conductance at the four nominal peak positions [13, 22]. This method tends to overestimate the polarization, so requiring a more accurate method of analysis [29]. Later, spin orbit scattering and orbital depairing in the superconductor were taken into account by using the DOS as derived by Maki [30]. The DOS of BCS superconductor is given by

$$N_s(E) = \frac{N_s(0)}{2} \text{Im}\left(\frac{u_{\pm}}{\sqrt{1-u_{\pm}^2}}\right) \quad (2.11)$$

where u_{\pm} is defined by

$$u_{\pm} = \frac{E \mp \mu H}{\Delta} + \frac{\zeta u_{\pm}}{\sqrt{1-u_{\pm}^2}} + b\left(\frac{u_{\mp} - u_{\pm}}{\sqrt{1-u_{\mp}^2}}\right) \quad (2.12)$$

Here $N_s(0)$ is the normal DOS at the Fermi energy in the superconductor, Δ is the energy gap, ζ is the depairing parameter and b the spin-orbit parameter, and μ is the magnetic moment of the electron. If the temperature and applied field are known, the remaining

fitting parameters are the superconducting gap (Δ), the depairing parameter (ζ), the spin orbit parameter (b) and the spin polarization of the tunneling current (TSP).

The most familiar response of a superconductor to a magnetic field is the Meissner effect [31] in which a superconductor in a magnetic field responds to screening the field by establishing circulating currents similar to eddy currents in a normal metal. The current flows in a surface layer whose thickness, the penetration depth λ , is the depth to which the external field penetrates into the superconductor. This current is non-dissipative and leads to the critical field by raising the free energy of the superconductor. In the case of Al, a type I superconductor, the penetration depth λ is shorter than the coherence length ξ . The coherence length ξ is a measure of the average size of the electron pairs and the minimum length scale over which the superconducting wave function can change. It is roughly inversely proportional to the critical temperature of the superconductor T_c . [22]

If the thickness d of the superconductor is much smaller than the penetration depth (λ) and smaller than the coherence length (ξ), a magnetic field parallel to the plane of the film penetrates the film almost uniformly and the screening currents are minimal. From a microscopic point of view, the magnetic field breaks the time-reversal symmetry and tends to break up superconducting pairs. Maki [32] showed that in the short-mean-free-path limit, the strength of the interaction detrimental to superconductivity can be included in terms of the orbital depairing parameter (ζ) parallel to the film plane with

$$\zeta = \frac{e^2 d^2 v_F l H^2}{18\hbar} \quad (2.13)$$

where v_F is the Fermi velocity, l is the mean free path, and H is the magnetic field applied in the film plane. Thus thicker films with longer mean free paths give a larger depairing parameters, which tend to break up superconducting pairs, leading to smaller critical fields. From this calculation, the critical field of thin Al is about 4.7T, showing good agreement with experiment. Pair breaking can not only be caused by an applied magnetic field but also by magnetic impurities in the superconductor. Figure 2.8(a) illustrates the influence of a change in ζ on the superconducting DOS. As ζ increases, the intensity of

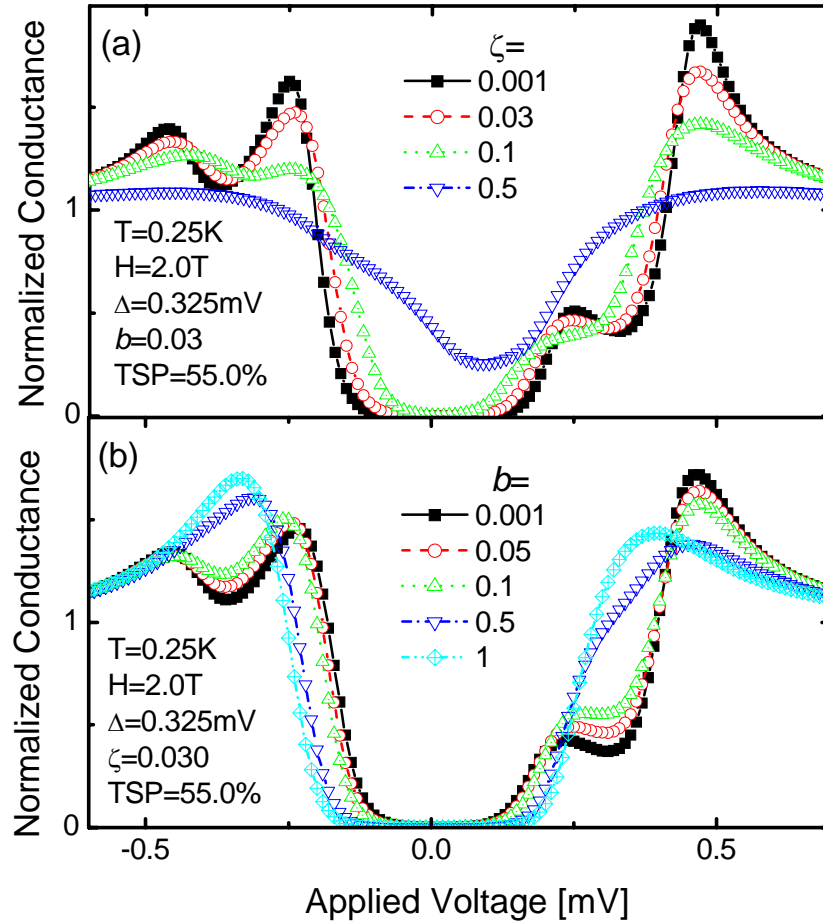


Figure 2.8: Influence of orbital depairing parameter (a) and spin-orbit scattering parameter (b) on the theoretical conductance curve in a ferromagnetic metal / barrier / superconductor junction. The curves are calculated using an applied field of 2T, at a temperature of 0.25K. The values of ζ and b are indicated in the graph.

each peak decreases, resulting in a blurred curve, and eventually loses features of superconductivity.

Another important mechanism in the fitting procedure is spin-orbit scattering. Consider an electron moving in a perfect lattice of a conductor. If a non-magnetic impurity is present in the otherwise periodic structure, a distortion of the periodic (in space) electric field will result. This distortion has the effect on the rapidly moving electron of a time-varying magnetic field which can then flip the electron spin. This effect tends to mix the up and down spins, however, it does not break the pairs (time-reversal invariant). In

Maki's description of the superconducting DOS, followed by the calculation of the strength of this process from Abrikosov and Gorkov [33], the normalized spin-orbit scattering rate is given by

$$b = \frac{e^8 Z^4}{3\hbar^3 c^4 \Delta \tau} \quad (2.14)$$

where $1/\tau$ is the rate of momentum scattering, Z is the atomic number and Δ is the gap energy of superconductor. This Z dependence explains why Al is a good material for studying spin dependent tunneling. As pointed out by Engler and Fulde [34], the spin-orbit scattering effect modifies the spin-dependent DOS of the excited quasi-particles shown in Figure 2.8(b). As b increases, the intensity of the inner peaks is increased compared to that of the right outer peak, and the energy separation of the two peaks decreases, eventually merging together as though there is no spin.

Al has been widely used over the past 30 years because Al has a low spin-orbit scattering, which mixes the spin-up and spin-down electrons: the spin-orbit scattering increases approximately as Z^4 , where Z is the atomic number [22]. Moreover, the structure of Al/Al₂O₃/ferromagnet junctions, where the Al layer is deposited first, is insensitive to the over- or under-oxidation of the Al layer since the superconductor and tunnel barrier are formed from the same metal. However, the superconducting temperature of Al is typically below ~ 2.5 K and so measurements must be made at even lower temperatures, typically below ~ 0.4 K, for good spectral resolution. It would be useful if higher temperature superconductors could be used. A different superconducting material NbN which enables us to measure at elevated temperatures will be discussed in Chapter 4.

One of our typical TSP measurements with an Al superconducting layer and the corresponding fit is shown in Figure 2.9. Usually, the temperature and applied field are measured and so are not used as fitting parameters. The remaining fitting parameters are ζ , b , Δ and the tunneling spin polarization (TSP). A background signal is subtracted before the fitting procedure to take the non-linear behavior of tunnel junctions into account. The background can be determined by driving the superconductor normal either by applying a field higher than the critical field or by increasing the temperature above

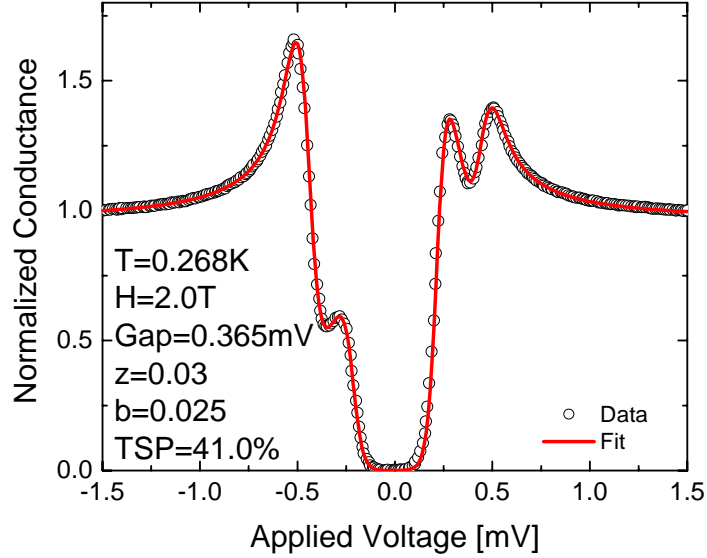


Figure 2.9: Typical measured conductance versus voltage data for a Al/Al₂O₃/Co FIS junction and the corresponding fitted curve derived using Maki theory.

the critical temperature of the superconductor. Although there are four fitting parameters, the TSP can be extracted with high accuracy ($\pm 1\%$) since the asymmetry of the low energy peaks, which is a measure of the spin polarization, is largely insensitive to changes of ζ , b , and Δ .

A small amount of Si is incorporated into the Al superconducting layer in order to enhance the critical temperature (T_c) and the critical field of the superconductor and to reduce hillock formation of the Al film. [35] In the case of Nb, which has a peak in the DOS near the Fermi surface (FS), scattering tends to smear out that peak, and along with the McMillan equation due to the phonon softening at surfaces and interfaces, T_c reduces with disorder, even when the disorder is interface scattering. The opposite is true with Al and Mo, which each have a dip in the DOS around the FS, so disorder increases T_c due to the reduced grain size. [36]

The TMR value calculated using the Julliere's formula and values of measured TSP from STS studies is the upper limit for TMR because the TSP experiment is carried out at high field (a few tesla), low temperatures ($\sim 0.25\text{K}$), and almost zero bias (a few mV), all of which conditions favor high TSP. The advantage of high field is that it can align

completely all the magnetic moments including any paramagnetic moment, which may not otherwise be aligned in smaller fields (hundreds of oersteds (Oe)) typically used to switch the alignment of the ferromagnetic layers in an MTJ. Another reason for the upper limit is that superconducting tunneling spectroscopy involves only one ferromagnetic electrode, whereas TMR measurements involve two ferromagnetic electrodes. Growth roughness and stacking faults may propagate into the upper ferromagnetic electrode and so limit the polarization of this ferromagnetic electrode. However, studies in which the ferromagnetic electrode is placed above or below the tunnel barrier in FIS experiments, show that for proper optimization of the structure, the same TSP values are found for both the lower and upper interfaces. [35] The problem with MTJs is that the alignment of the AP state is likely to be imperfect since the formation of this state in small magnetic fields relies on either exchange bias or different coercivities of the two ferromagnetic electrodes, as discussed in chapter 1.

2.3 Inelastic electron tunneling spectroscopy

The tunneling magnetoresistance (TMR) of magnetic tunnel junctions (MTJs) decreases with increased voltage and temperature. This is thought to be due to inelastic tunneling from phonons, and magnons at the interface between the ferromagnetic electrode and the insulator, and impurities both at these interfaces and within the interior of the tunnel barrier, which may result in flipping of the electron spin and so a decrease in the spin polarization of the tunneling electrons. The predominant elastic tunneling, where incident electrons from one electrode tunnel through the barrier without loss of energy to the opposite electrode, gives rise to a significant background of the conductance versus voltage curve. Figure 2.10 shows an energy diagram comparing elastic and inelastic tunneling processes. It is thus important to clarify the relationship between the tunnel conductance and the interface structure of an MTJ.

The dependence of the tunneling current (I) on applied bias (V) is reasonably well understood for elastic tunneling processes: at low voltage I is proportional to V , and at higher voltage, I depends exponentially on V . This I - V relation is often modeled using the Simmons' equation which is derived from straightforward quantum mechanical arguments under the assumption that the tunnel energy barrier has a simple trapezoidal shape with tunnel barrier width. This problem can be solved exactly analytically. Thus such fits allow an effective barrier height and the effective mass of the tunneling electrons to be extracted. [37] Deviations from this simple behavior are common especially when higher order dependences of the conductance versus bias voltage curves are measured i.e. measurement of dI/dV versus V or d^2I/dV^2 versus V . [38]

Inelastic electron tunneling spectroscopy (IETS), is the measurement of d^2I/dV^2 versus V and was first developed in 1966 by Jacklevic and Lambe [39]. This is a very sensitive spectroscopic technique which has been used to study the electronic structure of chemical compounds and complexes incorporated within insulating barriers, as well as the detailed electronic nature of interfaces within metal/ insulator/ metal (MIM) tunnel junctions. In the latter case the observation of both the vibrational as well as electronic spectra (defects, impurities, magnons, and phonons) has been carried out. Unfortunately, the

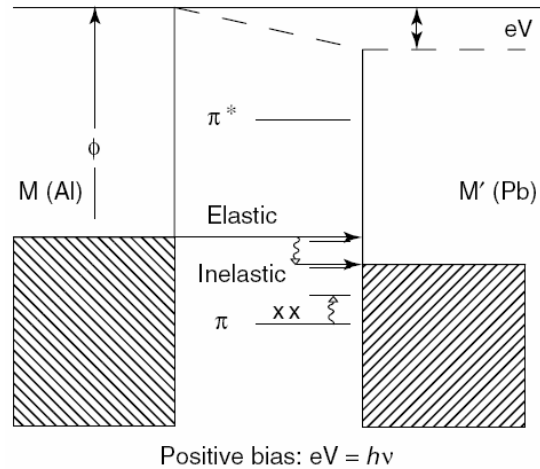


Figure 2.10: Energy diagram of a tunneling junction showing elastic and inelastic tunneling processes. [40]

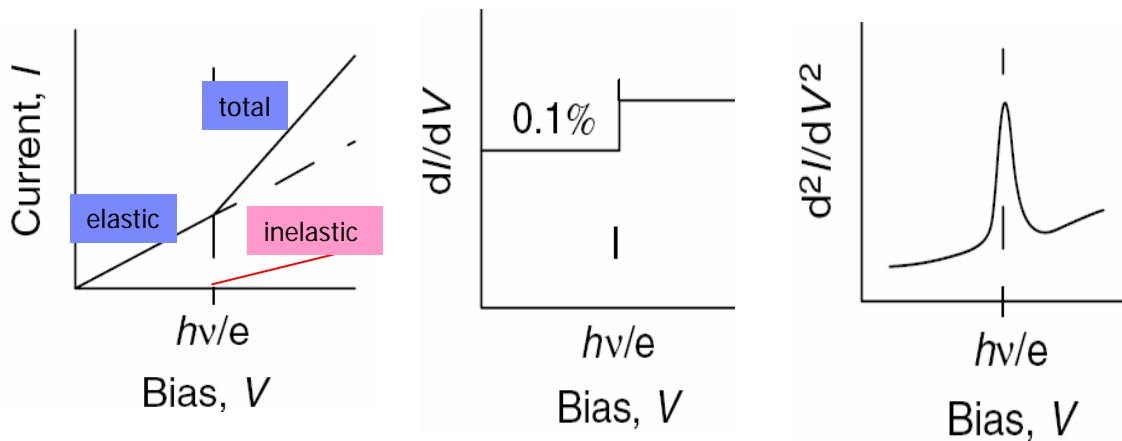


Figure 2.11: Illustration of an I - V curve, and corresponding conductance and derivative of conductance versus V curves (the latter corresponds to what is termed the inelastic tunneling spectrum - IETS).

number of electrons tunneling inelastically is usually orders of magnitude smaller than the number utilizing elastic channels (see Figure 2.11). Thus, it is hard to detect the energy at which an inelastic channel opens from I - V or conductance- V curves because the contribution from these channels is too small against the much larger elastic background. However, higher order derivatives of the conductance versus voltage curves often reveal peaks at energies corresponding to those of the inelastic tunneling channels, where

incident electrons lose energy inside the tunnel barrier or at the barrier/electrode interfaces.

Experimentally, modulation techniques are often employed to obtain the second derivative of the I - V curve. Either the current or the voltage applied across the junction may be modulated because the line shapes of d^2V/dI^2 and d^2I/dV^2 versus the dc bias voltage are related through the relationship $d^2V/dI^2 = -(1/G^3)d^2I/dV^2$, where the dynamic conductance, $G = dI/dV$, is slowly varying over the desired voltage range. If the voltage applied across the tunnel junction is a small AC signal $V_w \cos(\omega t)$, superimposed on a DC bias signal (V_G), the current through the junction can be written as a Taylor expansion,

$$\begin{aligned} I(V) &= I(V_G + V_w \cos \omega t) = I(V_G) + \left. \frac{dI}{dV} \right|_{V_G} V_w \cos \omega t + \frac{1}{2} \left. \frac{d^2I}{dV^2} \right|_{V_G} V_w^2 \cos^2 \omega t + \dots \\ &= I(V_G) + \left. \frac{dI}{dV} \right|_{V_G} V_w \cos \omega t + \frac{1}{4} \left. \frac{d^2I}{dV^2} \right|_{V_G} V_w^2 + \frac{1}{4} \left. \frac{d^2I}{dV^2} \right|_{V_G} V_w^2 \cos 2\omega t + \dots \end{aligned} \quad (2.15)$$

Therefore, the amplitude of the first harmonic is proportional to the first-derivative term, and the second harmonic is proportional to the second-derivative term, which can be extracted using phase-sensitive detection techniques. In the early 60s, a complex low-noise bridge circuit was used to detect the second harmonic signal. [41, 42] Today, we can simply use a lock-in amplifier to detect the second harmonic component which is proportional to d^2I/dV^2 .

Actual IETS peaks are broadened due to thermal smearing of the Fermi edge. For normal metal electrodes, Jacklevic and Lambe [43] obtained a half maximum width $\delta V = 5.4kT$ by considering the line thermal broadening. Klein *et al.* [44] computed the line-width $\delta V = 1.22eV_w$ due to the broadening from a finite modulation amplitude. Using a finite-modulation technique, the full width at half maximum (FWHM) of the line peak δV is given by

$$\delta V = \sqrt{(5.4kT)^2 + (1.22eV_w)^2} \quad (2.16)$$

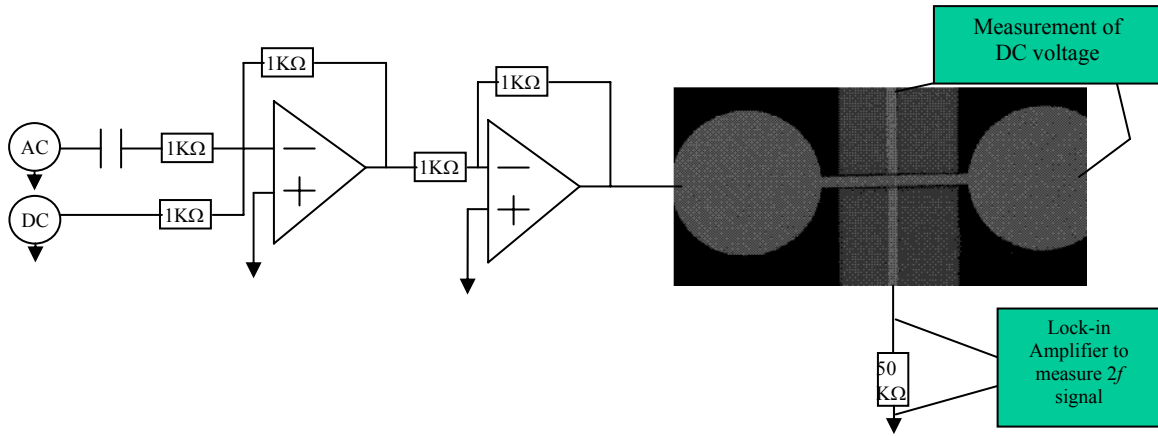


Figure 2.12: IETS measurement scheme for a MTJ. The complex filter scheme is not shown.

The modulation amplitude can be adjusted to give good resolution. However, a compromise must be found between the modulation amplitude and the signal-to-noise ratio. [45] Shen *et al.* [46] demonstrated that the optimum measurement condition for detecting IETS is about $kT/eV_w=0.2$. At $T=4.2\text{K}$, the simple equality of the broadening prescribes a modulation magnitude of 1.6mV. At $T=2\text{K}$, the optimum measurement condition involves a modulation amplitude of 0.8mV. In IETS experiments, the usual practice is to keep the modulation at a level, where broadening is comparable with $5.44 kT$ [47]. The modulation frequency is another factor in obtaining good resolution. Considering the tunnel junction as a simple resistor-capacitor (RC) parallel network, the magnitude in the real component of IETS signal decreases at higher frequencies. [48] However, $1/f$ noise is smaller at higher frequencies. In order to compromise between higher resolution and improved signal-to-noise ratio, the modulation frequency should be optimized, which happens in the kHz frequency range.

In our experiment, AC and DC voltage sources are summed through op-amplifiers as shown in Figure 2.12, and applied to two terminals of the tunnel junction. The DC junction voltage is measured at the other two terminals using a voltmeter, and a lock-in amplifier is used to detect the second harmonic current signal. A typical measurement is shown in Figure 2.13. The IETS signal from the AP configuration is normally large and

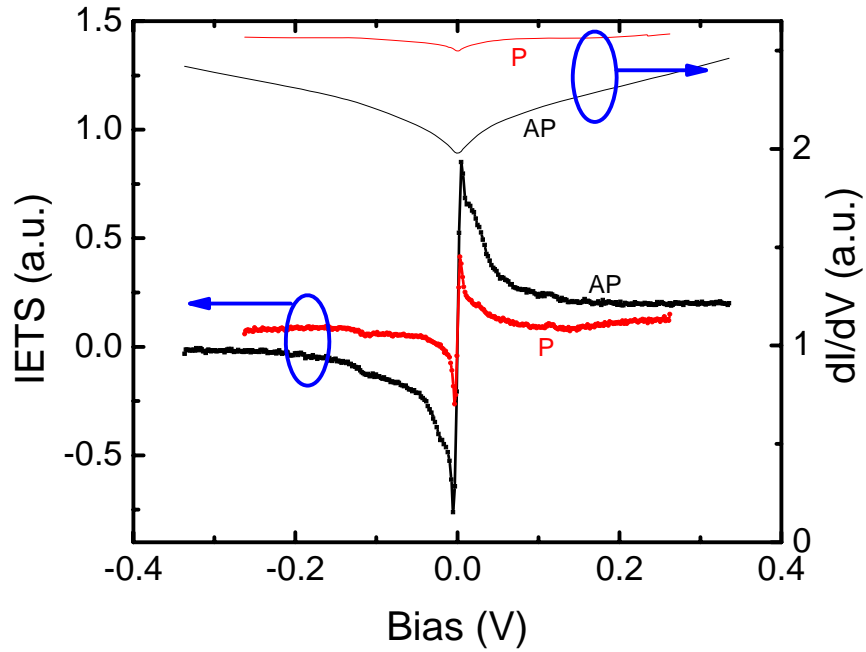


Figure 2.13: Conductance and IETS measurement from CoFe/ Al_2O_3 barrier/ CoFe junction at 2.6K. Red corresponds to the parallel configuration and black indicates the antiparallel configuration.

more sensitive to the spin-dependent scattering. Typical phonon spectra of the Al (33mV) and the Al-O longitudinal optical (LO) modes (20mV and 120mV) were observed.

2.4 Sample preparation

For this work, magnetic and superconducting tunnel junctions were deposited on Si(100) substrates coated with 25 nm thick SiO₂ using *in situ* metal shadow masks. The films were prepared by dc magnetron sputtering in 3mTorr argon in a high vacuum deposition system with a background pressure of $\sim 2 \times 10^{-9}$ torr, which is achieved by a series of roughing, turbo, and cryo-pumps.

The shadow masks are used to define patterns of the deposited material on the substrate. They are made of various metals and can be fabricated to allow for feature sizes down to as little as 20 μm . However, for MTJs and STS structures the smallest features were usually about 80 μm . Both the substrate and mask platters are fully automated and independently rotatable, thus allowing for the use of any substrate with any mask at any gun position (see Figure 2.14 for a schematic drawing of the sputtering deposition system). Permanent magnets placed above the substrate platter in several of the deposition positions create a ~ 100 Oe magnetic field to set the exchange bias field direction.

All samples are grown on 1-inch Si substrates supplied by Virginia semiconductor with 25 nm of thermal silicon oxide. They are cleaned in an ultra-violet ozone cleaner for 8 min, followed by a de-ionized rinse for 3 min to remove surface contamination. The samples are then placed in the vapor of boiling isopropanol for 3 min, and then heated to 50 °C in a nitrogen dryer until dry, for approximately 2 min. The samples are then mounted on a substrate carrier and loaded into a sputtering system. The system is then baked with the walls of the chamber reaching ~ 110 °C and the samples reaching 150 °C. This base pressure of 2×10^{-9} torr is achieved every morning after being vented for ~ 2 hours, and baked for 8 hours overnight.

Typical deposition rates are 0.1 nm/sec and the shutters are timed so that the layer can be grown with ~ 0.1 nm precision. The thickness of a given layer depends on the power of the magnetron source, the geometry of the source/target, the material, and the conditions of sputtering. The key to navigating this multidimensional space is to perform systematic

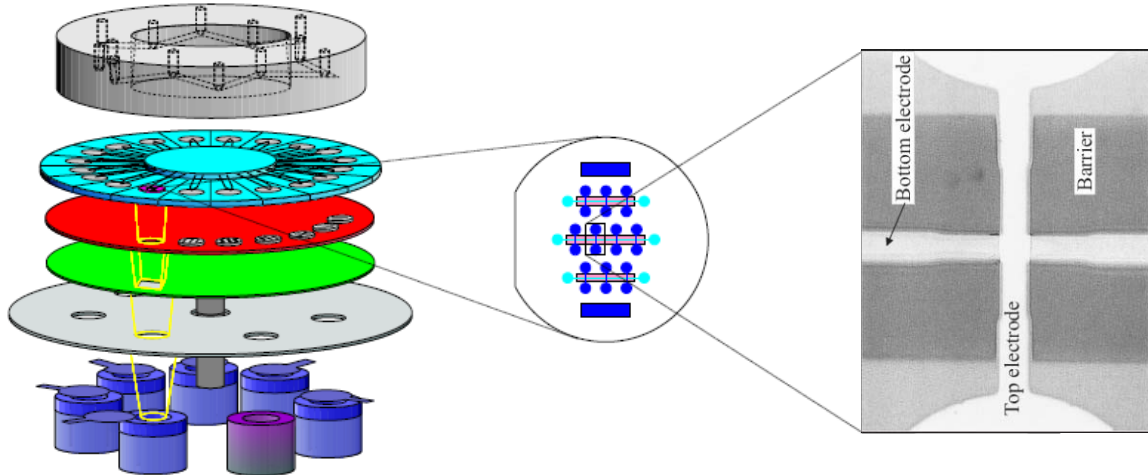


Figure 2.14: Schematic of the sputtering system (left image). Shadow masking is used to define the electrodes and barriers. In the middle a typical deposited wafer and on the right hand side an SEM picture of one of the junctions is shown.

experiments while maintaining many variables constant. To determine the rates, 50nm thick calibration films are deposited on specially masked substrates. The mask for the calibration films allows thickness measurements with a DekTak mechanical profilometer. After the thickness of the film is determined, the deposition rate can be calculated. Also, the calibration films can be analyzed with Rutherford Back Scattering Spectroscopy (RBS) to determine the composition of alloy films because the target composition is not always mapped 1:1 onto the substrate. RBS also allows for the determination of impurity concentrations and the thickness of the calibration film.

This sputtering system allows for deposition in argon, oxygen, nitrogen or any combination of the above. Usually the deposition of metals is done in an Ar atmosphere of 3mTorr. In addition to the thermal oxidation process, oxide barriers can either be fabricated by plasma oxidization of the metal (usually in 100mTorr O₂) or via reactive sputtering of the metal in an Ar/O₂ atmosphere where the Ar/O₂ ratio is usually set between 97/3 and 90/10.

Chapter 3. Coherent tunnel barriers

3.1 High TMR from Fe/MgO(001)/Fe

One intriguing possibility illustrated by the Julliere model is that if magnetic electrodes can be found that have spin polarization values of exactly 100%, then the TMR of a magnetic tunnel junction incorporating such electrodes would be infinitely large. Such metals are termed half metals, a term coined by de Groot in 1983 [49], because only one of the two spin bands has filled electronic states (the other has no spin states). Such a MTJ could theoretically act like a perfect switch with no current flowing for one orientation of the magnetic electrodes - antiparallel if both electrodes are formed from either majority or minority spin polarized half-metals and, parallel if the two electrodes are comprised of one majority and one minority spin polarized half metal. Much attention has been focused on materials which were predicted to be half metallic (NiMnSb [49], CrO₂ [50], Fe₃O₄ [51], and LSMO [52]). None of these materials has proven to be half metal at room temperature, although very high TMR and TSP values have been found for both LSMO and CrO₂ at low temperatures (TMR ~1000% in the former case [53] and TSP values of nearly 100 % in the latter [50]). Recent calculations [54] have suggested that at finite temperatures the half metallic character will likely be destroyed.

Most of the predicted half metallic ferromagnets have Curie temperatures well below room temperature. By contrast, conventional ferromagnetic metals and alloys formed from one or more of Fe, Co and Ni have much higher Curie temperatures—well above room temperature. However, after several decades of work, the highest TSP found in technologically useful tunnel junctions incorporating these metals is ~55% for alumina tunnel barriers [22, 55], with corresponding TMR values in MTJs of up to ~70% at room temperature [56]. Due to the amorphous nature of the Al₂O₃ tunnel barrier, a theoretical calculation of the TMR or TSP from first principles calculations has not yet been carried out.

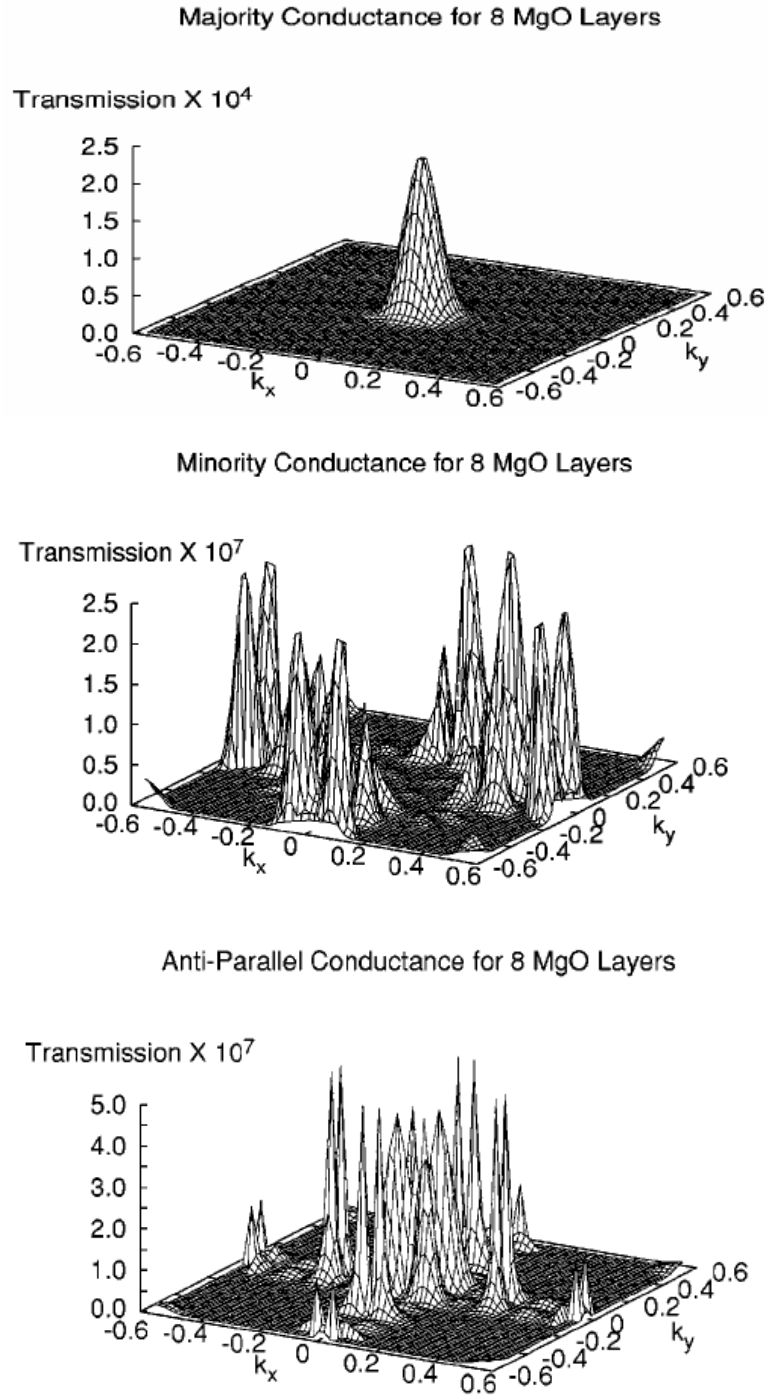


Figure 3.1: Majority (top), minority (middle), and antiparallel (bottom) conductance versus the crystal momentum in the film plane for a (100) Fe/8ML MgO/Fe structure. [57]

It has been predicted that crystalline tunnel barriers may give rise to much higher TSP and TMR values because of a highly spin-dependent evanescent decay of certain wave-

functions, with particular transverse momentum values, across the tunnel barrier [58]. TMR values as high as thousands of percent were predicted for perfectly ordered (100) oriented Fe/MgO/Fe MTJs. [57, 59] The origin of this enormous TMR effect is coherent spin-polarized tunneling, where the symmetry of the electron wave functions plays an important role. Butler et al. [58] deduced that the tunneling conductance depends strongly on the symmetry of the Bloch states in the electrodes and the evanescent states in the MgO barrier. In particular, Bloch states decay at different rates through the barrier layer depending on their symmetry and interfacial resonance states with particular in-plane momentum. The upper two parts of Figure 3.1 show the conductance of majority and minority channels on momentum parallel to the barrier for a barrier composed of 8 MgO (100) layers. The bottom part of the same figure shows the parallel momentum dependent conductance for antiparallel alignment of the Fe electrodes. An important feature in the majority conductance is the concentration of the transmission in the region near $k_{\parallel}=0$. While the k_{\parallel} dependence of the majority channel conductance bears at least some similarity to that of free electrons incident on a simple barrier, the minority channel conductance is completely different. The complicated and sharply peaked structure arises from the interplay of interfacial resonance states, the k_{\parallel} dependence of the wave function decay rate in the MgO (including interference effects), and the symmetry of the minority Fe Bloch states relative to that of the complex energy bands of MgO. The transmission as a function of k_{\parallel} for the antiparallel alignment shows a combination of the features observed in the majority and minority channels for parallel alignment. Even for the thickest MgO barrier that was modelled, however, the maximum conductance for the antiparallel alignment does not occur exactly at $k_{\parallel}=0$.

In order to better understand the conductance, Butler et al. also examined the *tunneling* DOS for $k_{\parallel}=0$ for the individual energy bands. Figure 3.2 shows the density of states (DOS) for electrons incident from the left electrode for the individual majority and minority spin polarized conduction bands. One particular majority band (Δ_1) readily enters the MgO layers and decays slowly across the MgO barrier. The Δ_1 band is the only one of the 4 majority spin polarized bands at the Fermi energy compatible with *s* angular momentum character. The other bands contain significant amounts of *d* angular

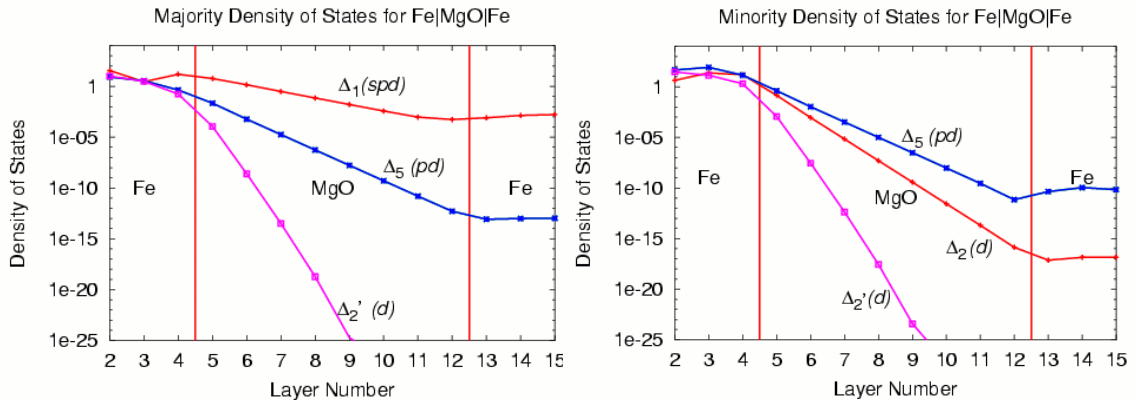


Figure 3.2: Tunneling density of states (TDOS) of the majority and minority channels at $k_{\parallel}=0$ from Fe(100)/8ML MgO/Fe(100). [57]

momentum character.

The main prediction from this first-principles calculation is the coherent tunneling of totally symmetric Δ_1 Block states. Among the evanescent electronic states in the band gap of MgO(001) in the $k_{\parallel}=0$ direction, Δ_1 states exhibit the slowest decay in the MgO tunnel barrier and therefore dominate the tunneling current. In the case of ideal coherent electron tunneling, only Fe- Δ_1 states, which are highly spin-polarized at the Fermi energy, couple with MgO- Δ_1 evanescent states at $k_{\parallel}=0$ when the Fe(001)/MgO(001) interface is not oxidized. [60]

These theoretical predictions motivated intense research activities over the past several years on epitaxial MTJs grown on single-crystalline substrates using molecular beam epitaxy deposition techniques. None of them [61-63], however, has demonstrated TMR values much higher than those that were achieved with alumina tunnel barriers. However, a giant TMR effect has been observed recently in MTJs with MgO(001) tunnel barriers by Parkin *et al.* in sputter deposited MTJs on amorphous substrates (in 2001) and by Yuasa *et al.* in MBE grown films on single crystal substrates (in 2004). The discovery of giant TMR values in sputter deposited polycrystalline films promises the application of these remarkable MTJs to magnetoresistive random access memory and magnetic sensors. [17, 64, 65] In the case of Yuasa's result, however, the need for single crystal substrates

and the growth using molecular beam epitaxy (MBE) limits its practical use. In addition, until very recently most work was for MTJs with very high resistance, which limits their operation frequency due to high Johnson and shot noise signals [66]. The resistance-area product (RA) of the MTJs must be less than $1\text{-}5 \Omega \mu\text{m}^2$ for TMR heads to compete with present-day spin-valve heads, and give sufficiently high data reading rates and noise margins. [67] For this low RA value, the tunnel barrier thickness has to be reduced to less than 1nm, which is hard to achieve uniformly across a whole wafer. A high TMR ratio at such low resistance was realized by the insertion of a thin Mg metal layer of 0.4nm between the bottom electrode and tunnel barrier layer. [66]

The remaining section of this chapter is devoted to recent improvements in MgO based MTJs in IBM within Stuart Parkin's group. These structures are prepared by a straightforward DC magnetron sputtering technique on thermally oxidized Si wafers at room temperature. Extraordinarily high TSP values of more than 90%, and correspondingly high TMR values of up to 350% at room temperature and nearly 600% at low temperature, using non-half metallic electrodes (CoFe) will be reported. The dependence of TSP on thermal annealing, structure, FM material as well as crystallographic orientation of the FM is discussed. The use of TSP measurements has several advantages over TMR measurements. In particular, for exchange biased MTJs in which the lower ferromagnetic layer is exchange biased, stacking faults tend to propagate from the IrMn layer through the lower CoFe layer through the MgO tunnel barrier to the upper CoFe layer. By replacing the top electrode with a superconductor, we can eliminate this effect and characterize only the single lower CoFe/MgO interface. Whereas TMR involves the measurement of the conductance of both the parallel and antiparallel states to infer the TSP of the conducting electrodes, in STS studies the TSP is measured directly from a single magnetic electrode where large magnetic fields completely align the moment of the ferromagnetic electrode. Because the AP alignment of the ferromagnetic electrode moments in a TMR measurement is unlikely to be perfect, TSP values give the upper value that TMR could reach if this alignment were to be perfect. Moreover, the fact that STS measurements using Al superconducting electrodes are also always carried out at very low temperature ($<0.4\text{K}$) also tends to give higher TSP values from STS than from TMR measurements.

3.2 TSP from (100) CoFe/MgO

For this work, superconducting tunnel junctions were deposited on Si(100) substrates coated with 25nm thick SiO₂ using *in situ* metal shadow masks. The films were prepared by dc magnetron sputtering in 3mTorr argon in a high vacuum deposition system with a background pressure of $\sim 2 \times 10^{-9}$ Torr. Four separate shadow masks were used to sequentially form the bottom electrode, tunnel barrier, isolation pads, and finally the top electrode. A bottom electrode consisting of 10nm Ta/ 25nm IrMn/ 3.5nm CoFe was first deposited, where the Ta and IrMn underlayers promote growth of an ultra smooth and highly textured layer of ferromagnetic bcc CoFe (100) [17] and form an exchange-biased CoFe layer similar to that of a practical MTJ device [68]. A highly textured MgO(100) layer is formed by reactive magnetron sputtering from a Mg target in an Ar-O₂ mixture [17]. Thick (~ 20 nm) isolation pads formed from MgO were used to avoid electrical shorts between the upper and lower electrodes. [35] Finally, the counter-electrode of Al was grown. The area of the tunnel junction in each case is $\sim 240 \times 80 \mu\text{m}^2$. The STS samples are usually grown with the superconductor on the bottom, whereas in our final structures AlSi constitutes the top electrode in order to maintain epitaxial growth of MgO utilizing Ta/IrMn underlayers. High resolution transmission electron micrographs (HTEM) show smooth and flat layers with a highly oriented (100) MgO barrier, as shown in Figure 3.3.

The TSP of the MTJs, as deposited, is modest but is dramatically increased by thermal annealing in vacuum at temperatures of up to $\sim 440^\circ\text{C}$. This is likely because the epitaxial quality of the MgO layer and the CoFe/MgO interface is improved through reduced impurities and defects. These defects are recognized by the difference in the MgO tunnel barrier height estimated from I - V curves and that directly measured in valence band photoemission studies. [17] As we anneal the samples, the top part of the Al superconducting layer is also likely thermally oxidized. The effective thickness of the Al layer is reduced thinner, resulting in a higher resistance of the Al layer and eventual loss of electrical connection to the device as shown in Figure 3.4. At least 60\AA of AlSi is required in order to anneal the sample up to 420°C . Thick Al gives rise to a bigger orbital

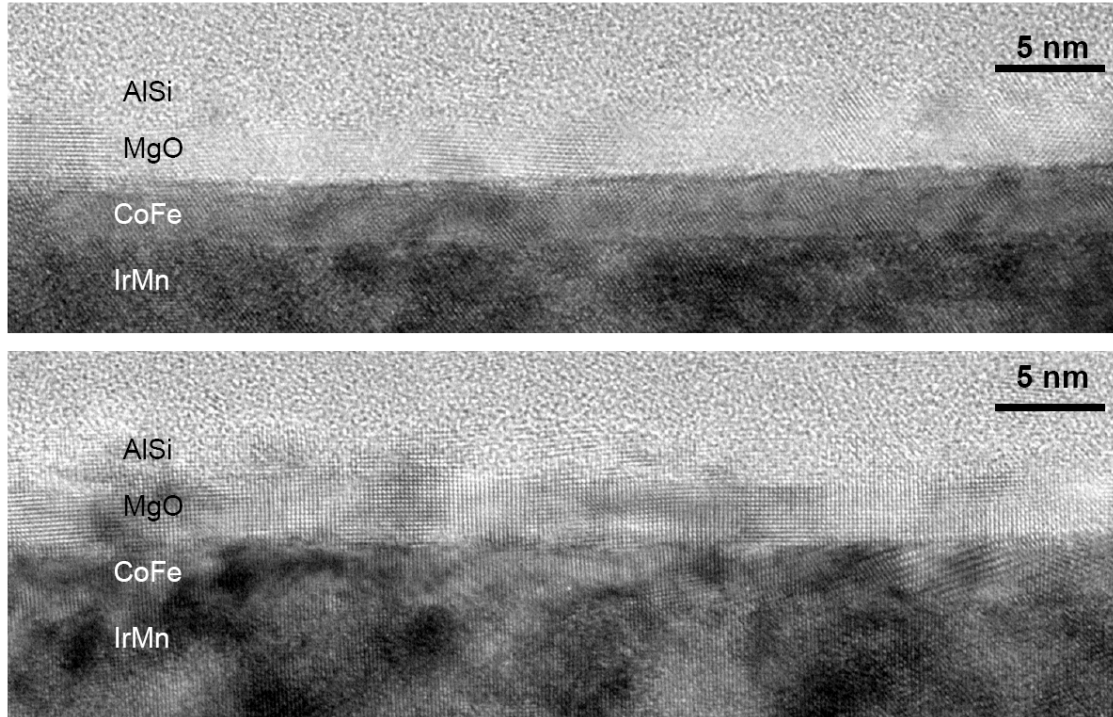


Figure 3.3: Transmission electron micrographs of an STS film with the structure of Ta/IrMn/CoFe/MgO/AlSi. The image is courtesy of Titus Leo, Arizona State University.

depairing parameter (ζ) from formula 2.13, as shown in Figure 3.5. Blurred features and finite conductance indicate an increased depairing parameter. This effect is theoretically plotted in Figure 2.8 (a). Therefore, the choice of an optimum Al layer thickness is crucial for TSP measurements of the annealed samples. The other possible method to prevent the oxidation of the top AlSi layer is to use MgO capping layer on top of AlSi. We did not find any noticeable difference between the samples with and without MgO capping, although the metal capping layer is of paramount importance for higher TMR [69].

One of the most important problems in preparing MgO barriers is to prevent oxide formation at the interface between the MgO barrier and the ferromagnetic electrodes, for example, FeO. In the growth of MgO on Fe by MBE methods a FeO interface layer between the Fe surface and the MgO layer was found. Theoretical predictions showed that even just one FeO layer would significantly reduce the TMR due to the reduced

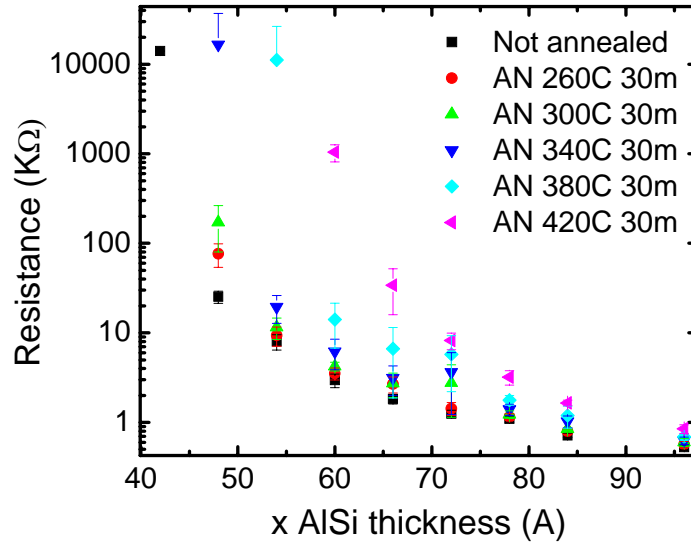


Figure 3.4: The contact resistance change of top AlSi electrode versus AlSi thickness. The structure is Ta/IrMn/CoFe/MgO(100)/AlSi.

conductance for parallel alignment of the magnetizations of the electrodes [60, 70, 71]. Paradoxically, it has more recently been calculated that the formation of symmetric FeO layers on either side of the MgO barrier will lead to high TMR [72]. In our experiment, the MgO barrier is formed by first depositing a thin layer of Mg metal, $\sim 5\text{-}9\text{\AA}$ thick, followed by the reactive sputter deposition of Mg in an Ar-O₂ plasma ($\sim 2\%$ oxygen) to form MgO. The Mg underlayer is used to prevent oxidation of the underlying ferromagnetic electrode but this layer is converted to MgO by reactive oxygen (atomic oxygen) introduced into the sputter chamber during the deposition of the MgO layer. Figure 3.6 shows the dependence of TSP on the thickness of the Mg underlayer. The optimum thickness for an unannealed samples is 8\AA . As we anneal the samples, TSP generally increases irrespective of the Mg thickness and, in some cases, the TSP exhibits high values after annealing above 380°C even without any Mg layer. We conclude that, under some circumstances, the Mg or MgO layer can reduce any oxide formed at the interface with the ferromagnet.

Recent x-ray photoelectron spectroscopy (XPS) measurements of the stoichiometry of the MgO layers show that the sputtered films are magnesium deficient, while the evaporated

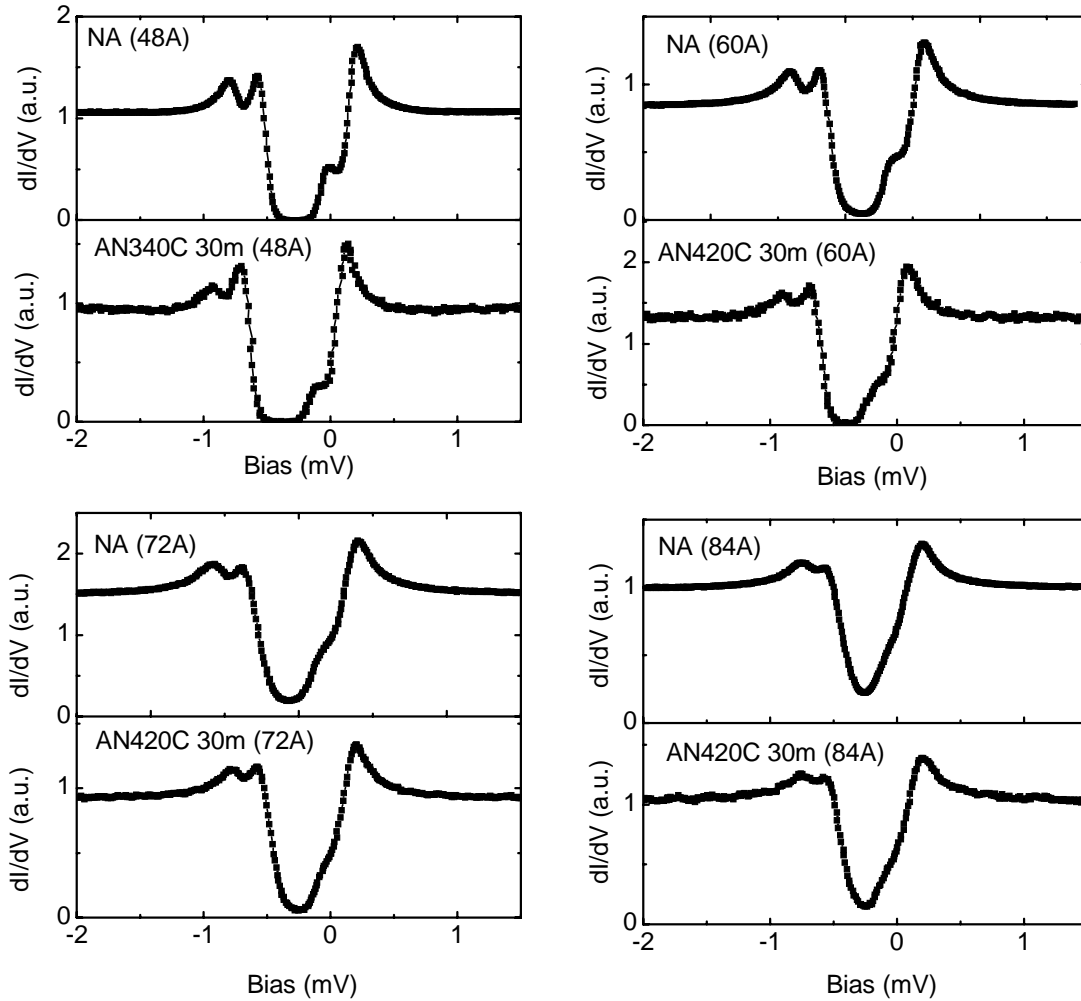


Figure 3.5: Conductance versus applied voltage curves of unannealed and after annealing for various AlSi thicknesses. The annealing temperature is indicated in the figure.

films are oxygen deficient. In both cases, the XPS spectra also clearly indicate a surface oxygen species that is likely bound by defects in the oxide. [73] There is less chemisorbed oxygen on MgO layers that are grown on a (001) textured bottom electrode than for those grown on amorphous electrodes. Thermal annealing of the MgO layers results in a significant decrease in the amount of this chemisorbed oxygen. The deposition of a thin metallic layer on top of the oxide film results in the displacement of some of the chemisorbed oxygen into the MgO and also in the partial oxidation of the overlayer. Upon annealing, oxygen from the electrode is incorporated into the MgO barrier. [74] The reduction of the ferromagnetic oxide (e.g. FeO) upon annealing above

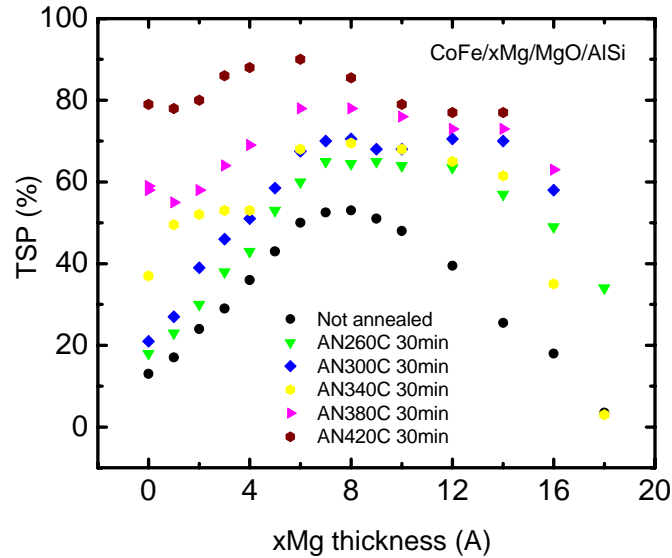


Figure 3.6: Tunneling spin polarization of the Fe/MgO interface versus Mg underlayer thickness for various annealing temperature. The structure is Ta/IrMn/CoFe/xMg/MgO (100)/AlSi.

380°C is likely the reason for the recovery of TSP on annealing for barriers formed without the Mg layer.

The maximum TSP obtained after annealing to successively higher temperatures is shown in Figure 3.7. After annealing at 420°C for 30min, the TSP reaches a value of 90% for barriers formed with a 6Å thick Mg underlayer, as shown in Figure 3.8. This value rivals those previously observed only using half-metallic ferromagnetic CrO₂. [50] Consistent with these high TSP values, we observe extremely high TMR of more than 350% at room temperature and nearly 600% at helium temperatures, as shown in Figure 3.9.

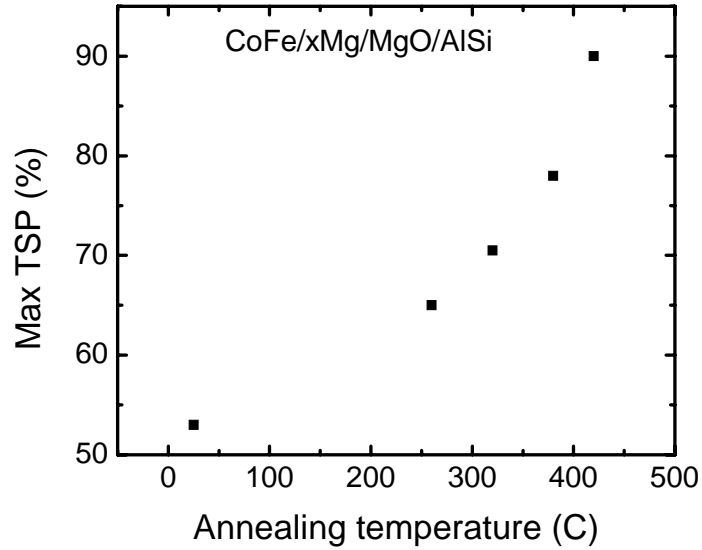


Figure 3.7: Tunneling spin polarization of the $\text{Co}_{70}\text{Fe}_{30}/\text{MgO}$ interface versus annealing temperature measured from STS studies at 0.25 K.

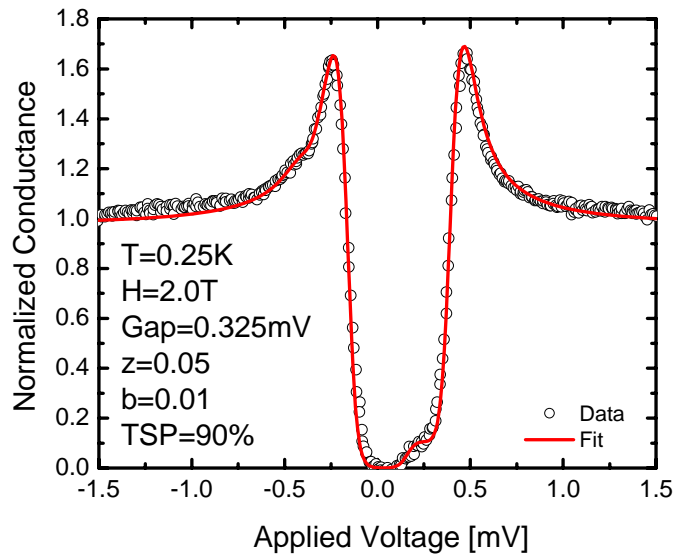


Figure 3.8: Conductance versus applied voltage curves showing 90% tunneling spin polarization from STS measurements. The fitting parameters of the STS measurement are shown in the figure.

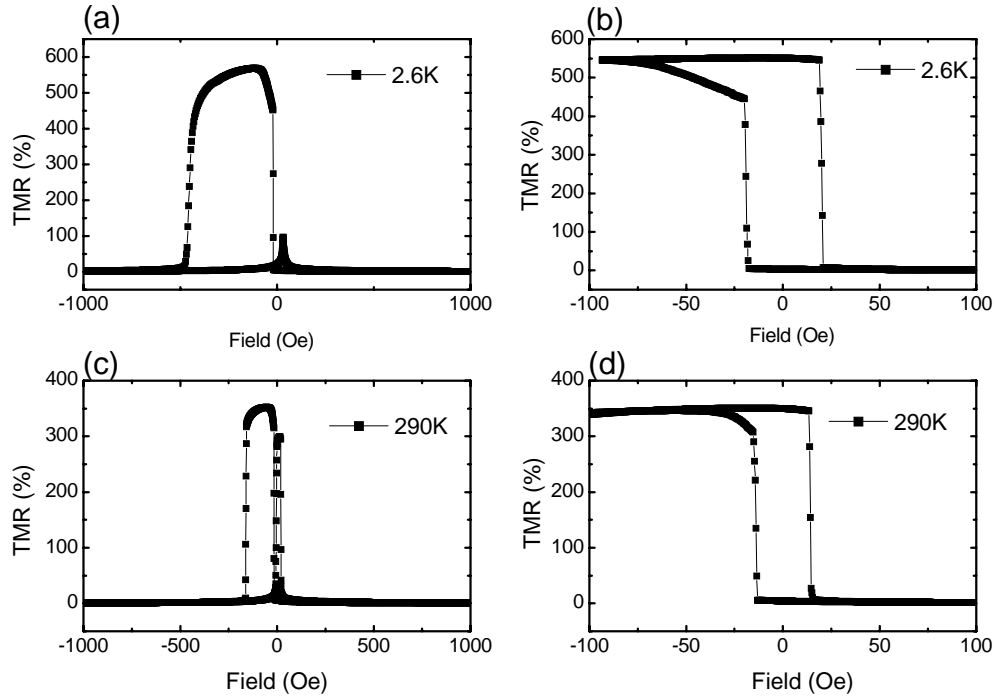


Figure 3.9: TMR versus field curves at (a, b: major loop) 2.6 K and (c, d: minor loop) 290K for an exchanged biased magnetic tunnel junction with a highly (100) textured MgO tunnel barrier.

3.3 TSP from CoFeB/(100) MgO

Amorphous CoFeB ferromagnetic electrodes [17] are thought to be of great advantage compared to polycrystalline CoFe electrodes in achieving highly homogeneous devices particularly at deep sub-micron dimensions. [65] Similarly, in order to obtain low coercivity (H_c) and low parallel coupling fields (H_{coupl}) in MTJ devices, amorphous (or nanocrystalline) ferromagnetic layers are likely to be advantageous [56]. Figures 3.10-3.12 show the TSP versus Mg underlayer thickness for various $[\text{CoFe}]_{1-x}\text{B}_x$ compositions. In the case of 12% and 15% boron contents, the TSP of the unannealed samples has a maximum value for thin Mg underlayers. The TSP values gradually decrease with increasing Mg thickness up to $\sim 8\text{\AA}$, and then suddenly drops above this thickness. After annealing an MTJ device with a 12% B content CoFeB alloy at 300°C , the TSP shows a broad maximum from 3\AA to 8\AA Mg thickness. This trend is similar to the pure CoFe case as shown in Figure 3.6, although the Mg thickness range for CoFe is $7\text{-}14\text{\AA}$. With 20% boron content, the TSP shows a more complex dependence on Mg thickness with two

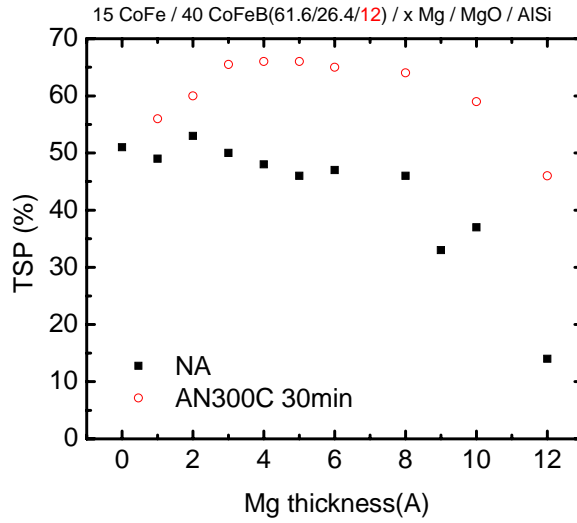


Figure 3.10: Tunneling spin polarization from CoFeB (12%)/MgO versus Mg underlayer thickness.

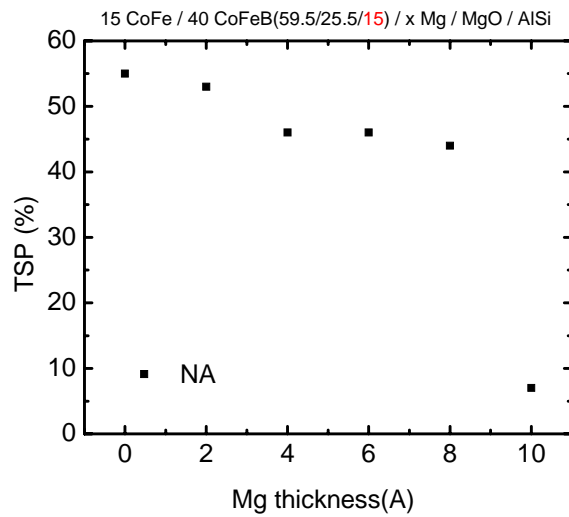


Figure 3.11: Tunneling spin polarization from CoFeB (15%)/MgO versus Mg underlayer thickness.

peaks at Mg thicknesses of zero and $\sim 8\text{\AA}$. This trend is preserved after annealing at 300°C for 30 min. The thickness of the Mg layer ($\sim 8\text{\AA}$) where the second peak in TSP occurs is the same thickness as that for pure CoFe (see Figure 3.6). One of the most distinctive features with CoFeB electrodes is that the TSP of unannealed samples has high values even without the Mg underlayer. This recovery of TSP happens after

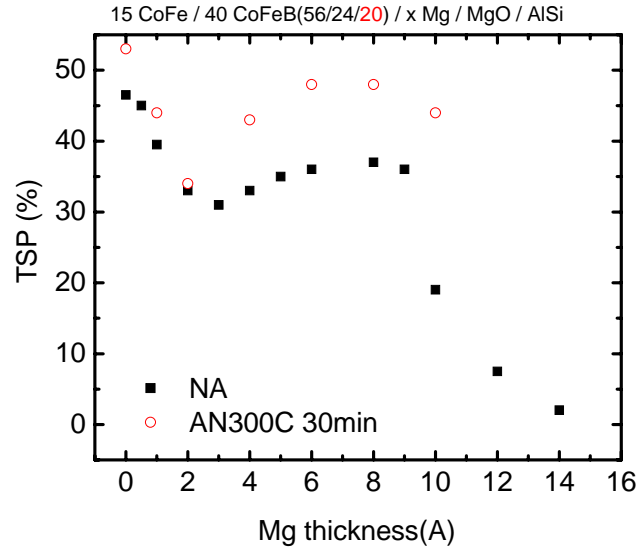


Figure 3.12: Tunneling spin polarization from CoFeB (20%)/MgO versus Mg underlayer thickness.

annealing above 380°C in the case of pure CoFe.

Boron has a larger Pauling electronegativity (2.04) as compared to Co (1.88) or Fe (1.83), which suggests that the driving force for the formation of a ferromagnetic oxide is reduced for CoFeB compared to alloys without any B. This is consistent with the high TSP values we find from unannealed samples without the Mg underlayer: we use the Mg with CoFe to prevent the formation of CoFe oxides which otherwise form. It is proposed that upon annealing B diffuses into the MgO barrier side because B has no solubility in CoFe and forms B-oxide collecting excess oxygen and reducing Fe-oxide. [75] However, our EELS data show that the B diffuses away from the MgO deeped into the CoFe later. One possible explanation is that even if B is located away from CoFeB/MgO interface, it can prevent ferromagnetic oxide formation. The influence of the chemical bonds formed at the ferromagnet/ insulator interface on the magnitude of the tunneling current can be described in terms of a tunneling matrix element. [24] Therefore, the TSP is influenced by the change of the tunneling matrix since the tunneling current is proportional to the density of states multiplied by the corresponding tunneling matrix element. With higher Boron content of 20%, the maximum TSP is increased slightly from 47 to 53% after

300°C annealing, whereas for CoFeB with 12% Boron or CoFe electrodes reaches almost 70% TSP.

3.4 TSP from CoFe(B)/(111) MgO

A Ta underlayer promotes the growth of (100) oriented fcc IrMn which then promotes the growth of (100) bcc CoFe and subsequently a (100) simple cubic MgO layer. These orientations have been confirmed by XTEM images. As discussed in the previous section it is for this orientation of the CoFe electrodes and MgO tunnel barrier that theoretical calculations predicted a highly spin polarized tunneling current. Here we investigate the TSP for a different crystallographic orientation of MgO using STS measurements. The orientation of the CoFe and MgO layers can be changed by growing them on appropriate underlayers. While Ti, Ta, TaN, and TaN/Ta bilayers lead to (100) oriented fcc IrMn, bcc CoFe and sc MgO, using Ta/Pt, Ta/Cu, or Ti/Pd underlayers the IrMn is fcc and (111) textured, the CoFe is bcc but (110) oriented and the MgO grows sc but in the (111) direction. However, XTEM studies show that the IrMn does not grow as flat in the (111) orientation as in the (100) orientation, and that consequently the CoFe and MgO layers are also rougher, as shown in Figure 3.13.

Figure 3.14 compares the dependence of TSP on Mg underlayer thickness for the (100) and (111) MgO orientations. Unannealed and annealed data from both orientations show very similar TSP values. In spite of the roughness of the layers for the case of (111) oriented MgO, TSP is still very high. This is quite a surprising result because the symmetry of the Bloch states for the (111) crystal face is calculated to be mainly of d character [76].

The main difference is that the TSP of the unannealed samples has a peak at zero Mg underlayer thickness for the case of (111) textured MgO. After annealing at 400°C, the TSP is independent of Mg thickness for both crystallographic orientations from zero to about 10Å Mg thickness. This independence of Mg thickness is even more pronounced than that of Figure 3.6. We tentatively attribute this to the effect of very thin (3Å) CoFeB layers placed between the IrMn and CoFe layers. Even a very thin CoFeB layer gives rise

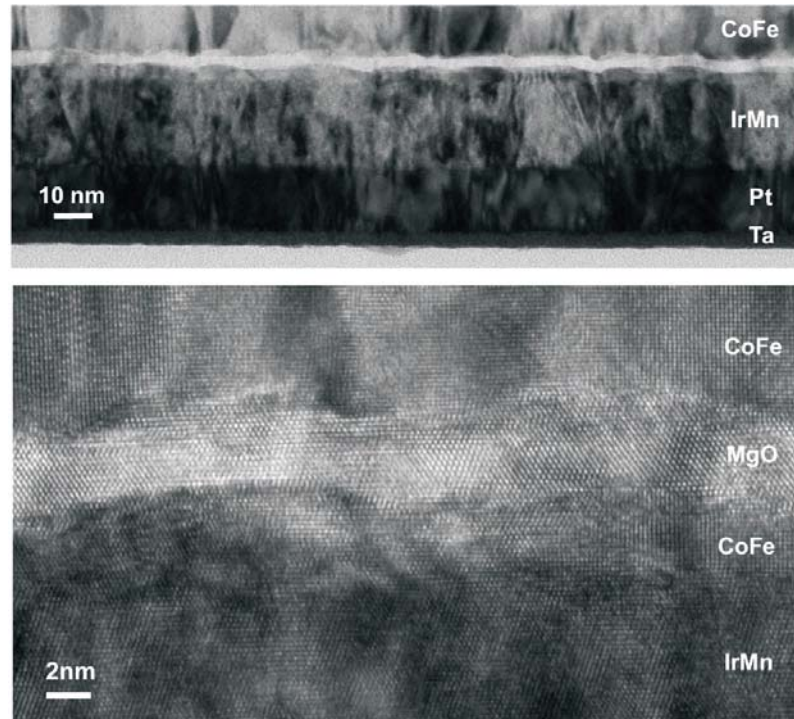


Figure 3.13: TEM images with low (upper panel) and high magnification (lower panel) for the following MTJ structure: 50Ta / 150Pt / 250IrMn / 25CoFe / 40MgO / 100CoFe / 100TaN (in Å). The high magnification image reveals that CoFe grows (110) oriented on the (111)IrMn and the MgO layer has a (111) texture. The image is courtesy of Phil Rice, IBM Almaden Research Center.

to a similar effect to that of a CoFeB electrode.

Although a significant increase of TMR with MgO barrier thickness was predicted, we find that the TSP changes little from 22Å up to 31Å MgO as shown in Figure 3.15. This behavior can be attributed to increased probability of electrons hopping through defect states in the middle of the barrier as MgO is increased in thickness. One notable feature of the MTJs with (111) textured MgO barriers is their poor thermal stability compared to similar MTJs with (100) oriented barriers. Upon annealing (111) textured samples at 410°C, the TSP drops dramatically as can be seen in both Figures 3.14 and 3.15.

MTJs with (111) oriented MgO barriers using a wide variety of underlayers were also prepared. Surprisingly, in contrast to the STS results, the (111) oriented samples in Figure 3.16 usually show much lower TMR values, here a maximum of 225% even at low

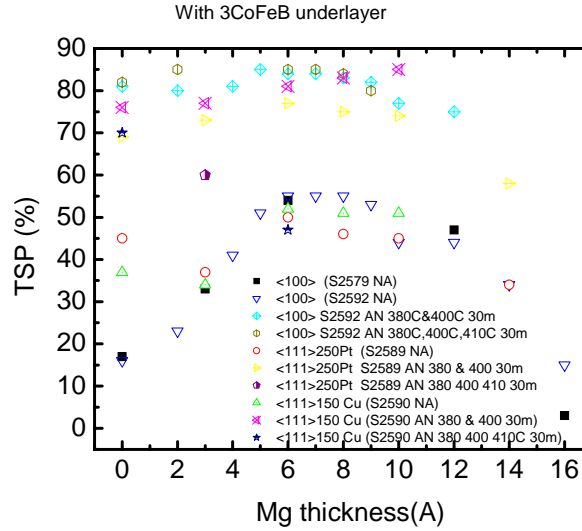


Figure 3.14: TSP versus Mg underlayer thickness for (100) and (111) MgO orientation. The structure is Ta, Pt or Cu/250 IrMn/ 3CoFeB/60CoFe/xMg/MgO/40AlSi (in Å).

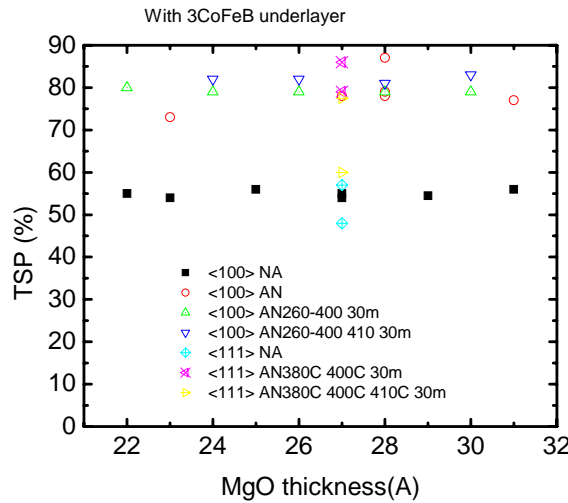


Figure 3.15: TSP versus MgO barrier thickness for (100) and (111) MgO orientation.

temperatures, as compared to the nearly 600% for the control samples that use (100) MgO barriers. TSP measurements only deal with the P state whereas TMR involves both the P and AP states. In Figure 3.16(a) the resistance of the P state (R_p) is almost constant over the entire temperature range, which is the same as for (100) MgO, while the resistance change of the AP state change is smaller than the (100) MgO case. Thus, this

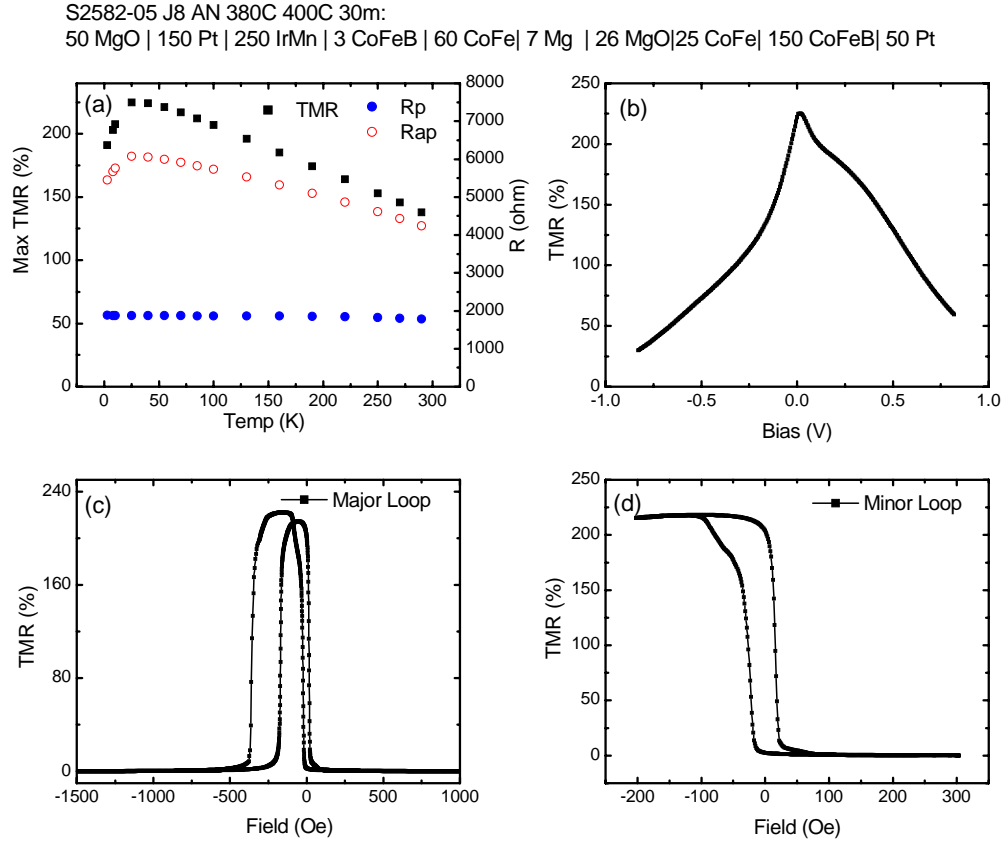


Figure 3.16: TMR of MTJs with (111) textured MgO barriers: (a) R_p , R_{AP} , and TMR versus temperature. (b) Bias dependency (b) and major (c) and minor (d) loops of samples showing the maximum TMR found.

small TMR may be caused by the poor antiparallel alignment in the case of the (111) orientation. Another possibility is the increased parallel resistance due to the reduction of effective junction area from rough MgO since tunneling is dominant through thin MgO region. TMR is defined by $\Delta R/R_p$, so that small change in R_p greatly influences the total TMR value.

Inelastic electron tunneling spectroscopy (IETS) was applied to MTJ samples with both (111) and (100) oriented MgO layers in order to detect various types of excitations at the tunnel-barrier interfaces (see Figure 3.17 and 3.18). For both MgO orientations, the IETS features are similar in both the parallel (P) and antiparallel (AP) configurations. However,

the IETS signal intensity is smaller for the parallel (P) configuration than for the antiparallel (AP) state, indicating that the spin-flip inelastic excitations are dominant for the AP configuration. One of the notable things in IETS is that the intensity difference between the P and AP states is proportional to the TMR value. Typical phonon spectra for the MgO optical (O) phonon at 27mV [44] and the MgO longitudinal optical (LO) surface mode at 83mV [77] were observed. Huge peaks around zero bias from both orientations result from magnon excitations, which are reported to be absent with non-magnetic electrodes. [78-80] The intensity of magnon excitations is comparatively stronger for (100) MgO textured samples than for (111) textured samples. This may be due to the denser lattice planes of (100) than (111) since spin-waves in cubic crystals are most easily excited perpendicular to the densest lattice plane. [81] In addition, the rougher surfaces for (111) MgO could prevent the propagation of spin waves and so being responsible for smaller magnon generation.

The broad peaks appearing around 500-600mV have never been observed in the MTJs with Al-O tunnel barriers and are usually not encountered in ordinary IETS measurements because such high energy inelastic excitations do not normally exist [82]. The energy of the hot electrons at that bias voltage is higher than the Curie temperature of the ferromagnetic electrodes (110meV for the Curie temperature of Co and CoFe) [83], resulting in no magnon excitation. The high energy peaks include information on spin dependent conductance channels that are related to the DOS of the two electrodes. The minority spin Δ_1 band of CoFe has no states at E_F for the direction normal to the barrier, however a band edge exists at $\sim 0.3-1.2\text{eV}$ above E_F depending on the composition of the electrode, whereas an edge of the majority Δ_1 band exists sufficiently below E_F . Consequently, conduction channels between the majority spin and the minority spin Δ_1 bands would open when the applied bias is higher than the band edge for the AP magnetic configuration, thereby creating the high-energy peaks. The observed peak positions are consistent with the band structure calculated for CoFe(001) [84].

Magnetic tunnel junctions have a promising future both as highly sensitive field sensors and as magnetic memory storage elements. In contrast to metallic spin-valve sensors, whose magnetoresistance is limited to 10-20% at room temperature, there is no

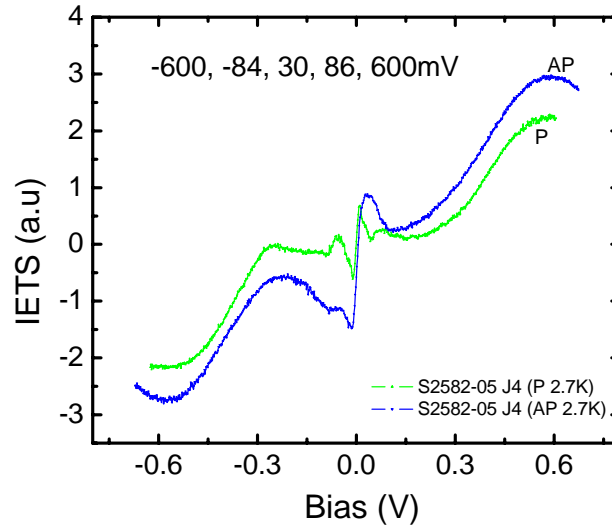


Figure 3.17: IETS of the (111) textured MgO from same sample as Figure 3.16 at 2.7K.

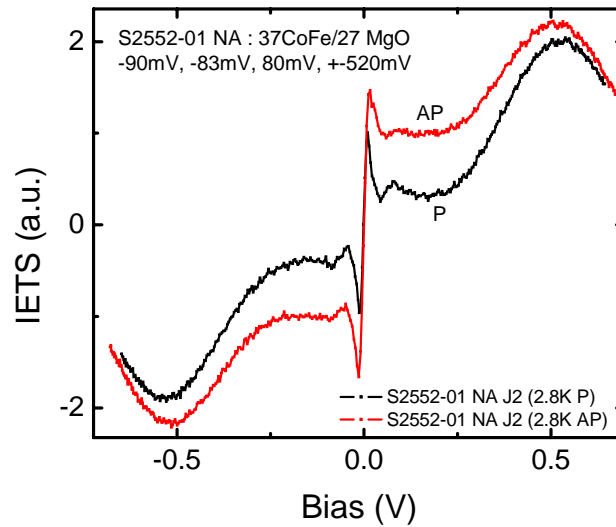


Figure 3.18: IETS from the sample of CoFe/(100)MgO/CoFe at 2.8K.

theoretical limit to the TMR of magnetic tunnel junctions. Whilst the very high TMR of >350% at room temperature observed with crystalline MgO tunnel barriers is very attractive for sensing and memory applications, it seems likely that new materials with

even higher magnetoresistance values will be found in the future which could have even wider technological applications.

3.5 AlN tunnel barriers

AlN tunnel barriers, along with Al_2O_3 and MgO, are one of the most widely studied tunnel barrier materials. Tunnel junctions with AlN barriers were prepared by reactive rf magnetron sputtering from an Al target in Ar- N_2 (20%). As shown in the XTEM in Figure 3.19, the AlN layer is crystalline and displays extremely flat interfaces. Tunneling spin polarization values deduced from superconducting tunneling spectroscopy of MTJs with AlN barriers are shown in Figure 3.20 for various ferromagnetic electrodes. The maximum TSP from CoFe is only 22.5%. However, the TSP with different electrodes changes in the same fashion as the TSP from Al_2O_3 shown in Figure 3.21.

Although it is clear that highly oriented crystalline MTJs are crucial in order to observe coherent tunneling in tunnel barriers such as MgO, and thereby obtain higher spin polarization (SP) and higher TMR, good crystalline material does not always give rise to high SP. More importantly, significantly different symmetries between the majority and minority spin polarized conduction band states in the ferromagnet/insulator are responsible for increased spin polarization of the tunneling current due to the different decay rate of these wave-function states across the tunnel barrier. Thus, the tunnel barrier can act as a spin-filter. The lack of coherent Δ_1 symmetry can be shown to be the absent of high energy excitations in the IETS data shown in Figure 3.22. On the contrary, a huge peak around 500mV is observed in the case of MgO based MTJs. The IETS signal from AlN based MTJs does not show any large peak, except around zero bias. Instead it shows many small excitations, identified as Al-N transverse optical (84mV), N-H (150-200mV), Al-H (225-270mV), and N-H (or O-H) phonon (370-450mV) excitations. MTJs with AlN barrier produce a negligible TMR effect even at low temperature.

By introducing a thin Al-oxide layer on top of AlN to form a hybrid barrier, we can engineer the tunnel barrier height, and thereby the TMR. Figure 3.20 compares the TSP from an AlN and composite AlN/1.5Å Al_2O_3 tunnel barriers. The TSP is systematically

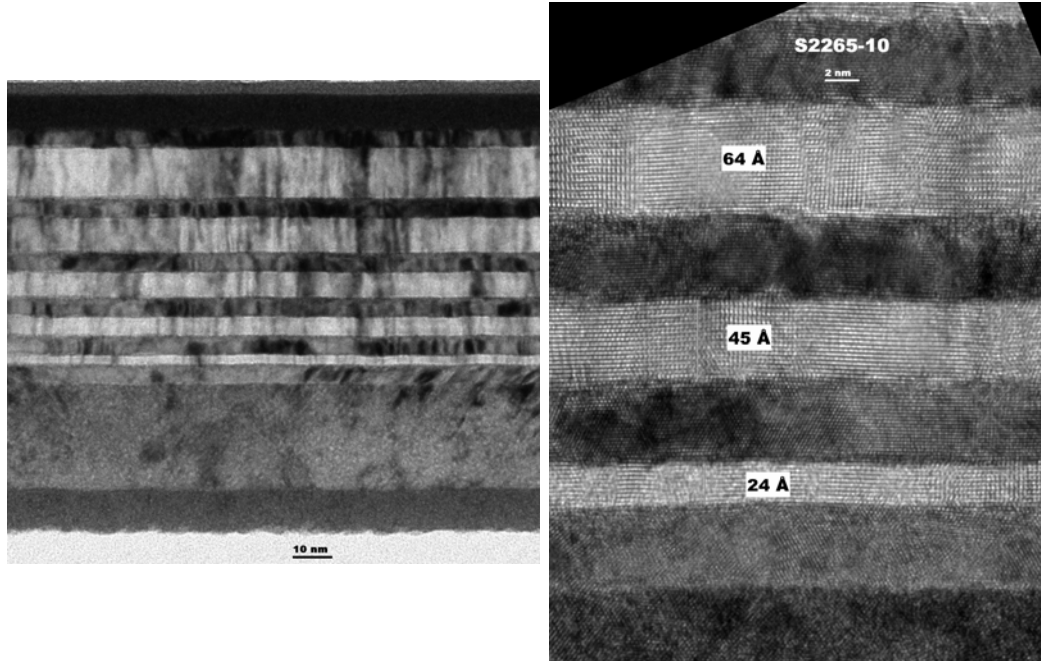


Figure 3.19: XTEM of MTJ with AlN tunnel barrier. The structure is 100Ta/ 250IrMn/ [50CoFe/x AlN]₅ (in Å).

increased slightly for all ferromagnetic electrodes considered except for the case of CoFeGd. This hybrid barrier concept can be used to reduce the RA values while maintaining considerable TSP. The TSP for MTJs with a MgO/Al₂O₃ hybrid barrier are shown in Figure 3.23 and shows the ability to control spin polarization using the thickness of each constituent of the hybrid barrier.

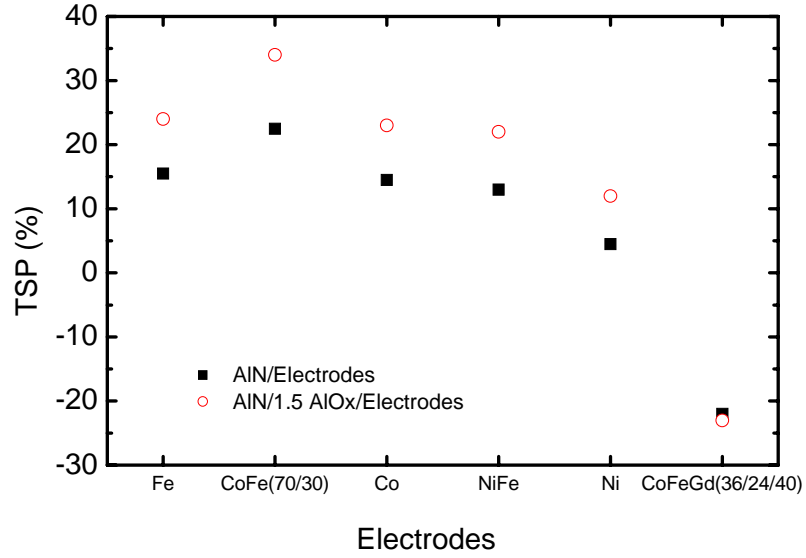


Figure 3.20: TSP from AlN barrier with different electrodes. The sample structure is 45 AlSi/34 AlN/electrodes or 45 AlSi/1.5 Al₂O₃/22 AlN/electrodes (in Å).

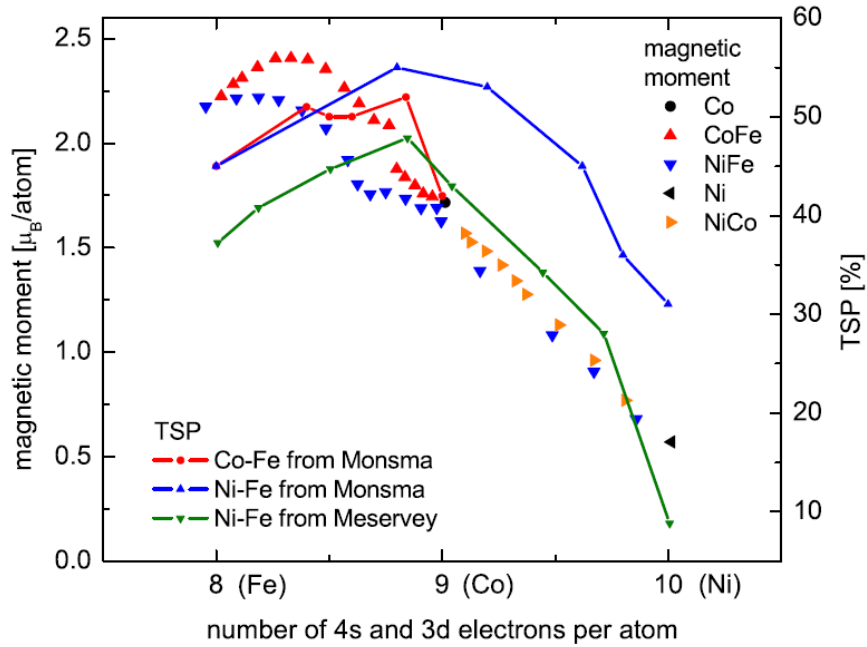


Figure 3.21: Tunneling spin polarization and magnetic moment per atom for different Co-Fe and Ni-Fe alloys. [85]

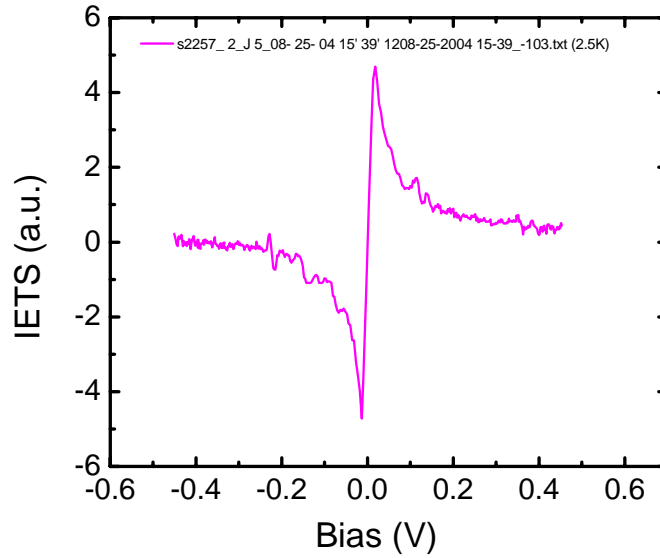


Figure 3.22: IETS data at 2.5 K from an MTJ with the structure of 40 CoFe/45 AlN/200 CoFe (in Å). The signal from P and AP states is almost identical due to small TMR effect.

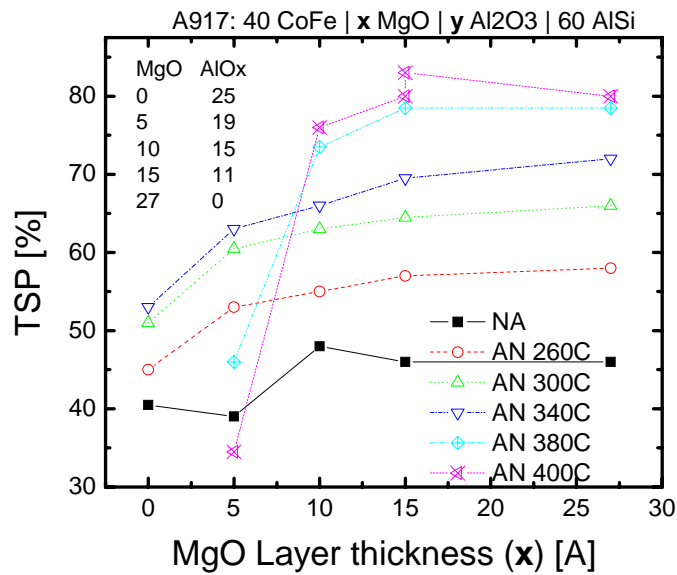


Figure 3.23: TSP data from MgO/Al₂O₃ hybrid barrier. Each barrier thickness is inserted in the figure (in Å).

Chapter 4. NbN superconducting spin detector

4.1 The need for a new superconducting material for STS

The superconducting tunneling spectroscopy (STS) technique, first developed by Meservey and Tedrow [22] using aluminum superconducting electrodes, has been applied to many ferromagnetic and ferrimagnetic metals. Al has been widely used ever since this early work because Al has low spin-orbit scattering, a high superconducting critical field ($\sim 4\text{T}$), and readily forms an insulating barrier (Al_2O_3). However, the measurements must be made at low temperatures ($< 0.4\text{K}$) since the superconducting critical temperature of Al is typically below $\sim 2.5\text{K}$. Figure 4.1 shows normalized conductance versus voltage curves for various temperatures and magnetic fields applied in the plane of ferromagnet-insulator-superconductor (FIS) structures with 4.5nm thick Al. For the case of Al, well-defined features start to appear above 2T at 0.25K, and superconductivity is quenched above 5T. At a fixed field of 3T, the Al FIS structure shows featureless curves at 1K and higher temperatures. It would be helpful to develop a new superconducting materials for STS, which would enable us to measure at elevated temperatures ($\sim 1.2\text{K}$), thereby eliminating the need the ^3He dilution refrigerators.

In discussing the response of superconductors to a magnetic field, superconductors can be divided into two classes, type I and type II. Type I superconductors are usually pure single-element metals, which have a relatively long electron mean free path, and a low transition temperature in zero field, T_{c0} . Type I superconductors are characterized by a penetration depth (λ) which is shorter than the coherence length (ξ). Type II materials are generally alloys, compounds, or dirty (short mean free path) materials in which $\xi < \lambda$.

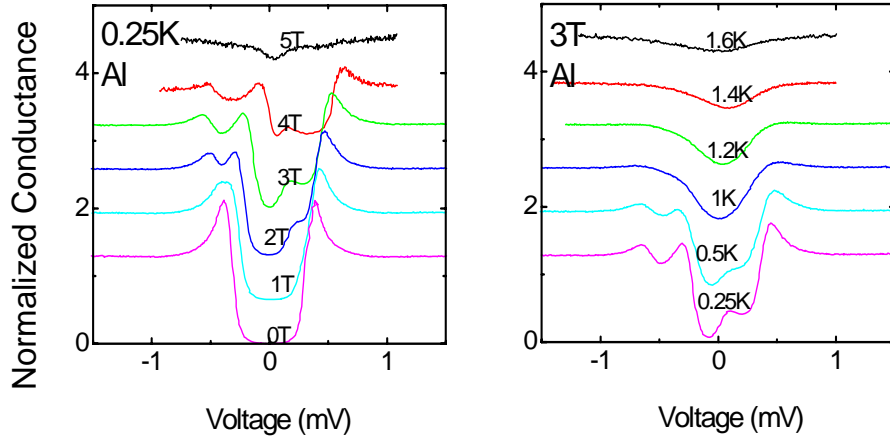


Figure 4.1: Conductance data from Ta/ IrMn/ CoFe/ MgO/ 4.5nm Al at 0.25K for various magnetic fields (left) and at a fixed field of 3T with various temperatures (right).

IA	IIA	IIIB	IVB	VB	VIB	VIIIB	VII	VII	VII	IB	IIIB	IIIA	IVA	VA	VIA	VIIA	0
1 H																	2 He
3 Li	4 Be 0.026											5 B	6 C	7 N	8 O	9 F	10 Ne
11 Na	12 Mg											13 Al 1.175	14 Si	15 P	16 S	17 Cl	18 Ar
19 K	20 Ca	21 Sc	22 Ti 0.40	23 V 5.40	24 Cr	25 Mn	26 Fe	27 Co	28 Ni	29 Cu	30 Zn 0.85	31 Ga 1.10	32 Ge	33 As	34 Se	35 Br	36 Kr
37 Rb	38 Sr	39 Y	40 Zr 0.61	41 Nb 9.25	42 Mo 0.912	43 Tc 7.80	44 Ru 0.49	45 Rh 0.0003	46 Pd	47 Ag	48 Cd 0.517	49 In 3.4	50 Sn 3.72	51 Sb	52 Te	53 I	54 Xe
55 Cs	56 Ba	57 La	58 Ce	59 Pr	60 Nd	61 Pm	62 Sm	63 Eu	64 Gd 1.083	65 Tb	66 Dy	67 Ho	68 Er	69 Tm	70 Yb	71 Lu 0.100	
87 Fr	88 Ra	89 Ac	90 Th 1.38	91 Pa 1.4	92 U .6/1.8	93 Np	94 Pu	95 Am 1.1/.79	96 Cm	97 Bk	98 Cf	99 Es	100 Fm	101 Md	102 No	103 Lr	

Legend

- Atomic Number
- Symbol
- T_c (K)
- Type I
- Type II
- Superconductor at ambient pressure
- Superconductor under high pressure

Figure 4.2: Periodic table showing superconducting transition temperatures of the elements.

When the applied field exceeds a value H_{c1} , type II superconductors admit the external field in the form of units of magnetic flux called vortices. Type II materials generally

have much higher critical fields than type I materials for the same value of T_{c0} . [22] In addition, type II superconductors normally are less sensitive to the orientation of the magnetic field. Figure 4.2 shows the periodic table of elements showing which elements are superconducting, their type and their critical temperature. It is clear that there are not many superconductors with critical temperatures above 10K with sufficiently small atomic number that they could be used for STS measurements. Small atomic number is required because spin orbit coupling, which mixes the spin channels of the tunneling electrons, increases rapidly with atomic number. Here we investigate Ta, Nb, and NbN superconductors as spin detectors. After NbTi, NbN is the most widely used low-temperature superconductor.

4.2 STS using Ta, Nb, and NbN superconductors

For this work, superconducting tunnel junctions were deposited by the same methods discussed in chapter 3.2 except for using NbN superconducting electrodes. The counter-electrode of NbN was grown, using reactive sputtering of Nb in Ar-N₂, capped with 2.5nm MgO to prevent oxidation. NbN and MgO both have simple cubic structures but with a small (~4%) lattice misfit. [86] Superconductor/ insulator/ superconductor (SIS) junctions were also prepared, but in these cases, NbN was directly deposited on top of the substrate without a Ta/IrMn underlayer. Growth of similar SIS junctions on MgO(100) substrates has previously been shown to lead to fully epitaxial junctions. [87] The Nb/N ratio was optimized by varying the N₂ content of the sputter gas and the power applied to the magnetron. Rutherford backscattering spectrometry (RBS) analysis shows that NbN layers deposited in Ar-N₂ with ~12.5% N₂ are stoichiometric within experimental error (50 ±0.5 atomic % N). Several superconducting electrodes with higher superconducting transition temperatures than Al were studied, including Nb, Ta and NbN. The thickness of each material was varied to find the optimum thickness for STS studies.

In order to explore the properties of thin superconducting layers of NbN, we investigated superconductor/ insulator/ superconductor (SIS) structures. The superconducting energy gap derived from the conductance curves from SIS (x nm NbN/ MgO/ x nm NbN)

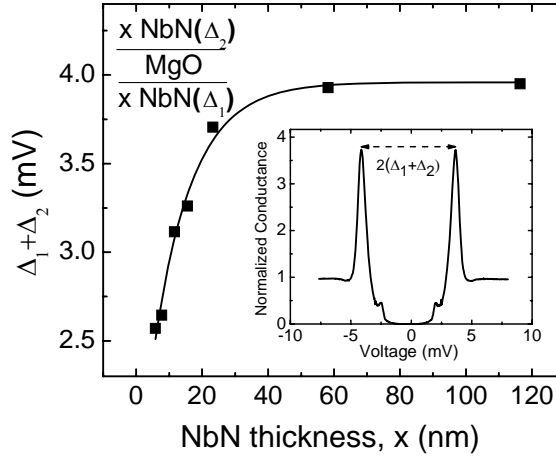


Figure 4.3: Superconducting energy gap $\Delta_1 + \Delta_2$ from tunneling spectroscopy data at zero field and 0.25 K versus NbN thickness for x nm NbN/MgO/ x nm NbN tunnel junctions. Δ_1 (Δ_2) corresponds to the energy gap of the bottom (top) NbN electrode. The inset shows a typical conductance versus bias voltage curve for x= 116nm.

structures is shown in Figure 4.3 as a function of the NbN thickness. This gap corresponds to the sum of the gaps from the two superconducting NbN electrodes ($\Delta_1 + \Delta_2$). From resistance versus temperature measurements of the critical temperature of each electrode in Figure 4.4, the bottom superconducting layer has a smaller energy gap. The largest critical temperature of FIS in Figure 4.4 shows that the morphology of the superconducting layers is better with a Ta/IrMn underlayer. We note that the resistivity of our NbN films varies little with temperature, even for thick NbN films. For example, the resistance of a NbN film ~ 100 nm thick, is 1.2 x higher at 15K than at 300 K. The energy gap increases steeply with thickness of the NbN layers, saturating above ~ 60 nm. The size of the gap is sufficiently large to allow application of the highest attainable field (8T) in our experimental setup with excellent resolution of the Zeeman split peaks in the excitation spectrum. The decrease in superconducting energy gap and transition temperature for thin NbN is typical of many superconducting thin film systems. [88]

Typical conductance data from a NbN/ MgO/ NbN structure are shown in the inset to Figure 4.3. These data correspond to 0.25K and zero applied field. Negligible conductance within the gap and very sharp conductance peaks at $\pm(\Delta_1 + \Delta_2)$ show that the

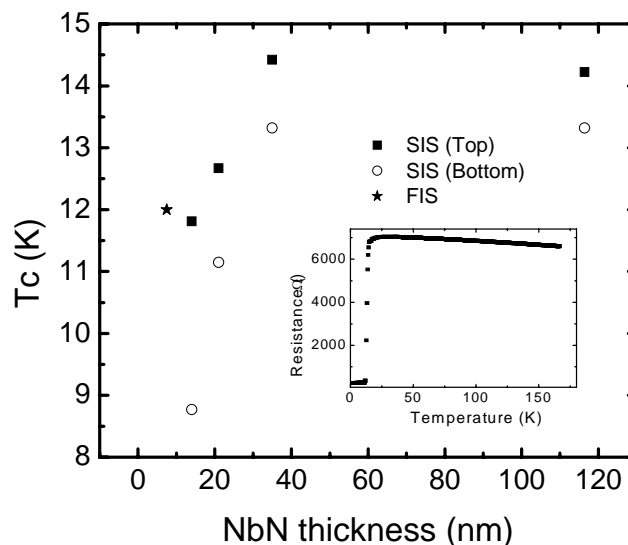


Figure 4.4: The critical temperature of NbN layers. When NbN is used as a top electrode in an FIS structure, it shows a maximum T_c . The inset shows the resistance of NbN layer versus temperature.

junction is of very good quality without any significant pinholes. Difference peaks due to the different gaps in each NbN electrode are not observed at 0.25K because there are few excited quasi-particles at these low temperatures [89]. We also observed a sub-harmonic structure - but only for the case of SIS but not for FIS structures- and some of the samples show multiple peaks in the sub-gap energy region. The origin of these features is not clear, but previous work on SNS junctions has interpreted similar features from higher order tunneling processes or from Andreev scattering from micro-shorts in the junction [90]. The absence of significant sub-gap leakage current would appear to rule out the latter. Typical conductance versus voltage curves from FIS structures are shown in Figure 4.5 for each of these superconductors, Nb, Ta and NbN. In-plane magnetic fields of 6T are used for NbN and Nb but a field of only 2T is used for Ta. In the latter case higher fields cause quenching of the superconducting gap. The data for NbN show a well defined superconducting energy gap with negligible leakage current at low bias and two well-defined peaks and two clear shoulders in conductance (for data measured in large in-plane fields). These features correspond to tunneling of spin-up and spin-down

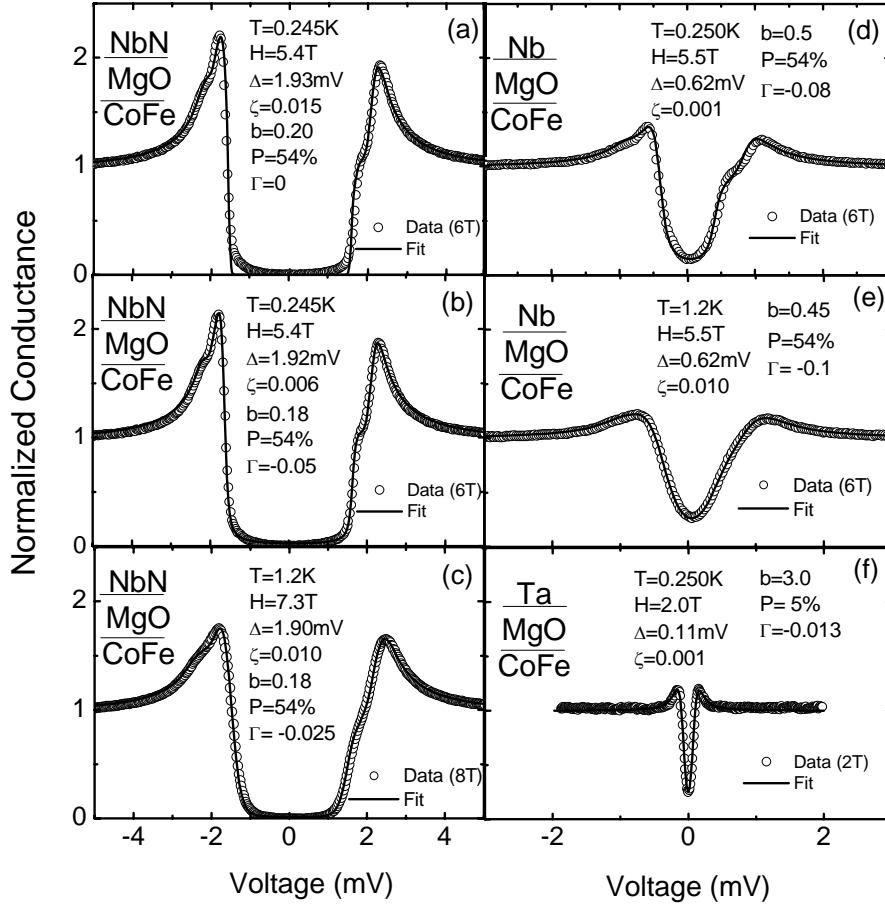


Figure 4.5: Normalized conductance versus bias voltage curves (symbols) and fits (solid lines) for various superconducting counter-electrodes: (a) as-deposited (no anneal) Ta/IrMn/CoFe/MgO/7.5nm NbN junctions at 6T and 0.245K – fit without strong-coupling parameter ($\Gamma=0$), (b) same as (a) but fit with $\Gamma= -0.05$, (c) same as (a) but measured at 8T and 1.2K and fit with $\Gamma= -0.025$, (d) as-deposited Ta/IrMn/CoFe/MgO/5nm Nb junctions at 6T and 0.25K, data fitted with $\Gamma= -0.08$, (e) same as (d) but measured at 1.2K and fit with $\Gamma= -0.1$, and, (f) as-deposited Ta/IrMn/CoFe/MgO/10nm Ta junctions at 2T and 0.25K, data fitted with $\Gamma= -0.013$.

electrons into the Zeeman split quasi-particle density of states in the superconductor.

The data was first fitted with a conventional BCS model, which includes a spin-orbit interaction parameter, b , to take account of spin mixing, and a depairing parameter, ζ to account of depairing of the Cooper pairs in a magnetic field. [91] As shown in Figure 4.5

(a) the data can be fitted reasonably well with such a model except at energies close to the superconducting energy gap. However, after treating the inherent recombination lifetime broadening of quasi-particle states in a strong-coupling superconductor by adding an imaginary part (Γ) to the BCS energy variable [90], very good agreement with the experimental data is found as shown in Figure 4.5 (b). A tunneling spin polarization $P=54\%$ provides the best fit as shown in Figure 4.5 (b). It is interesting to note that the fitted spin-orbit parameter we find for NbN is about 10 times larger than that found for similar structures using Al superconducting electrodes [17]. This ratio, however, corresponds well with the expected ratio of spin-orbit parameters for NbN and Al which vary as $\sim Z_{\text{NbN}}^4/Z_{\text{Al}}^4$ (neglecting the inverse dependence of b on conductivity times superconducting energy gap which turns out to be similar for our NbN and Al films) [22]. At 0.25K and 0T the superconducting transition temperature T_c of a 7.5 nm thick NbN film is reduced from the bulk value of 16.1 K to 12K. We obtain the ratio $2\Delta/k_B T_c$ to be ~ 3.76 (as compared to the BCS value of 3.52).

Even though Nb has a much larger spin-orbit coupling parameter than NbN, we were still able to determine the TSP value from fits to the data as shown in Figure 4.5 (d). Finally, the conductance data from Ta (Figure 4.5 (f)) shows the smallest gap feature, which, however, is quenched in comparatively small magnetic fields.

The high T_c of NbN films compared to Al allows for the possibility of carrying out STS measurements at higher temperatures. Figure 4.6 shows the normalized conductance versus voltage curves for various temperatures and magnetic fields applied in the plane of FIS structures with 7.5 nm thick NbN superconducting electrodes. For NbN, four well-defined conductance features appear above 6T at 0.25K. The NbN structure, at a fixed field of 8T, shows a shoulder at 1.8mV for temperatures up to ~ 1.2 K. We were able to obtain TSP values using NbN at temperatures as high as 1.2K as shown in Figure 4.5 (c), whereas Nb or Al shows featureless curves at 1.2K (see Figure 4.5 (e) and Figure 4.1 for Nb and Al, respectively). This makes possible STS studies without the need for complex ^3He cryostats. However, it is clear that at elevated temperatures, the conductance peaks in the STS data are less pronounced due to thermal broadening of the quasi-particle densities of states, which leads to a reduced accuracy in extracting TSP values. This is,

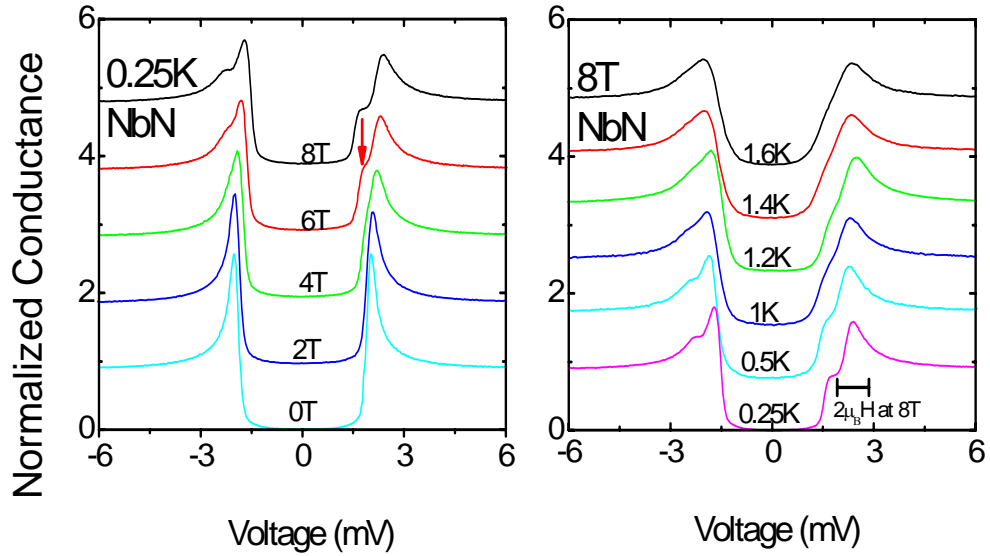


Figure 4.6: Conductance data from Ta/ IrMn/ CoFe/ MgO/ 7.5nm NbN junctions at 0.25K for various magnetic fields (left) and at a fixed field of 8T with various temperatures between 0.25 and 1.6 K (right).

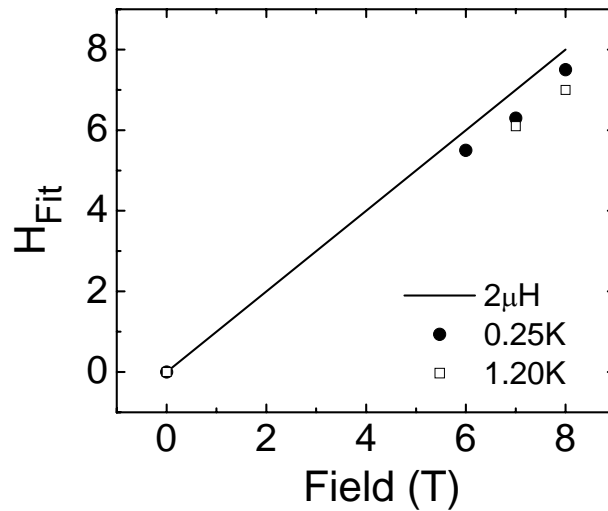


Figure 4.7: The fitted magnetic field is plotted as a function of the applied field at 0.25K and 1.2K for the devices of Figure 4.6. The solid line in the inset corresponds to the fitted field equal to the applied field.

however, mitigated by the possibility of making measurements at much higher magnetic fields than is possible with Al. We found that an as-deposited FIS structure yields a TSP value of 54% ($\pm 1\%$ at 0.25K and $\pm 2\%$ at 1.2 K, see Figure 4.5 (b) and Figure 4.5 (c), respectively), but that after annealing at 380 °C the TSP is increased to $\sim 78 \pm 2\%$ (not shown here). These results are in excellent agreement with STS values measured using Al superconducting electrodes at much lower temperatures (0.25K) [17].

At high applied magnetic fields in NbN the Zeeman splitting obtained from fitting the conductance curves corresponds to fields which are systematically lower as compared to the nominal applied magnetic fields as shown in Figure 4.7. These effects have previously been observed in the case of Ga [89] and V [92] superconductors and can be attributed to the renormalization of the quasi-particle density of states due to Fermi liquid effects.

We have studied the use of alternative superconductors to Al for measurements of the tunneling spin polarization of ferromagnets using superconducting tunneling spectroscopy. Superconducting electrodes of NbN, Nb, and Ta were investigated. NbN was found to be the most useful among these because of its comparatively high superconducting transition temperature and low spin-orbit scattering rate. We have demonstrated that NbN superconducting electrodes allow the measurement of tunneling spin polarization in ferromagnet /insulator/ superconductor tunnel junction devices at temperatures much higher than is possible using Al electrodes, making this an important technique of greater applicability for the further understanding of the spin dependent transport properties of magnetic tunnel junctions. We also showed that the TSP data cannot be fitted with the usual Maki density of states without including, in a strong coupling theory, a complex energy gap for NbN.

Chapter 5. Kondo resonance in magnetic tunnel junctions

5.1 Kondo effect [93]

Although the Kondo effect is a well known and a widely studied phenomenon in condensed matter physics, it continues to capture the imagination of experimentalists and theorists. The effect arises from the interaction between a single magnetic atom, such as cobalt, and the many electrons in an otherwise non-magnetic metal. Such an impurity typically has an intrinsic angular momentum or “spin” that interacts with the electrons. As a result, the mathematical description of the system is a difficult many-body problem. However, the Kondo problem is well defined, making it an attractive testing ground for the new numerical and analytical tools that have been developed to attack other challenging many-body problems. The Kondo effect can provide clues to understanding the electronic properties of a wide variety of materials where the interactions between electrons are particularly strong, for instance, in heavy-fermion materials and high temperature superconductors. Physicists’ fascination with the phenomenon has continued since it was first explained by the Japanese theorist, Jun Kondo, in 1964. In fact, interest in the Kondo effect has recently increased thanks to new experimental techniques from the rapidly developing field of nanotechnology, which have given us unprecedented control over Kondo systems.

The electrical resistance of a pure metal usually drops as its temperature is lowered because electrons can travel through a metallic crystal more easily when the vibrations of the atoms are reduced. However, the resistance saturates as the temperature is lowered below about 10 K due to defects in the material (Figure 5.1). Some metals – for example, lead, niobium and aluminium – suddenly lose all their resistance to electrical current and become superconducting. This phase transition from a conducting to a superconducting

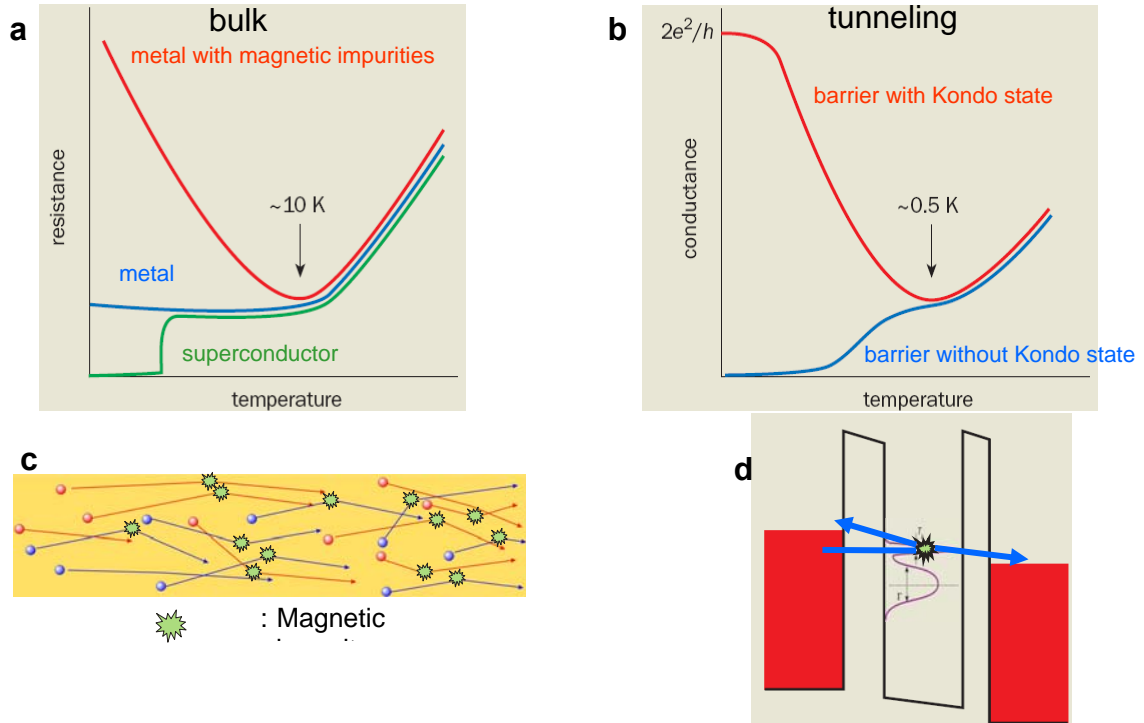


Figure 5.1: (a) Temperature dependence of resistance from different metals. (b) Conductance enhancement due to Kondo assisted tunneling. (c) Metals with magnetic impurities have lots of scattering centers, which increases the resistance at low temperature. (d) Kondo resonance in a double tunnel junction device. [93]

state occurs at a so-called critical temperature, below which the electrons behave as a single entity. Indeed, superconductivity is a prime example of a many-electron phenomenon. Other metals, like copper and gold, remain conducting and have a constant finite resistance, even at the lowest accessible temperatures. The value of the low-temperature resistance depends on the number of defects in the material. Adding defects increases the value of this “saturation resistance” but the character of the temperature dependence remains the same.

However, this behavior changes dramatically when magnetic atoms, such as cobalt, are added. Rather than saturating, the electrical resistance increases as temperature is lowered further, as shown in Figure 5.1 (a). Although this behavior does not involve a phase transition, the so-called Kondo temperature – roughly speaking, the temperature at which

the resistance starts to increase again – completely determines the low-temperature electronic properties of the material. Since the 1930s, there have been many observations of an anomalous increase in the resistance of metals at low temperature. Yet it was not until 1964 that a satisfactory explanation was developed. Electrical resistance is related to the amount of back scattering from defects, which hinders the motion of the electrons through the crystal. Theorists can readily calculate the probability with which an electron will be scattered when the defect is small. However, for larger defects, the calculation can only be performed using perturbation theory. In 1964 Kondo made a startling discovery when considering the scattering from a magnetic ion that interacts with the spins of the conducting electrons. He found that the second term in the calculation could be much larger than the first. The upshot of this result is that the resistance of a metal increases logarithmically when the temperature is lowered, however Kondo's result is correct only above a certain temperature (T_K).

In the late 1960s Phil Anderson's idea of "scaling" in the Kondo problem provided the theoretical framework for understanding Kondo physics below T_K . Later, in 1974, Kenneth Wilson devised a method known as "numerical renormalization" that overcame the shortcomings of conventional perturbation theory and proved the magnetic moment of the impurity ion screened entirely by the spins of the electrons in the metal at temperatures well below T_K .

The Kondo effect only arises when the defects are magnetic –in other words, when the total spin of all the electrons in the impurity atom is non-zero. These electrons coexist with the mobile electrons in the host metal, which behave like a sea that fills the entire sample. The simplest model of a magnetic impurity, which was introduced by Anderson in 1961, has only one electron level with energy ϵ_0 . In this case, the electron can quantum mechanically tunnel from the impurity and escape provided its energy lies above the Fermi level, otherwise it remains trapped. In this picture, the defect has a spin of 1/2 and its Z-component is fixed as either "spin up" or "spin down".

However, so-called exchange processes can take place that effectively flip the spin of the impurity from spin up to spin down, or vice versa, while simultaneously creating a spin

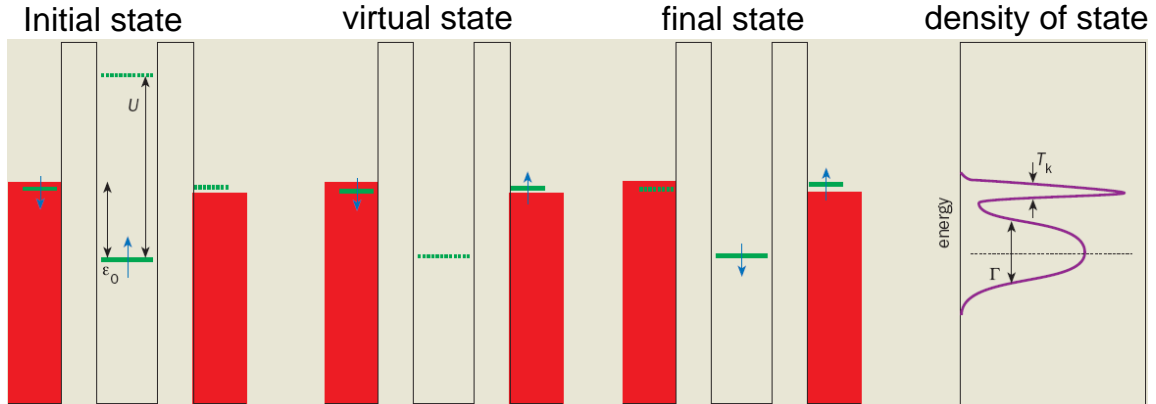


Figure 5.2: The Anderson model of a magnetic impurity with one electron energy level (ϵ_0), showing effective spin flipping due to quantum mechanical tunneling. Right figure shows the Kondo resonance due to many such tunneling events. [93]

excitation in the Fermi sea. Figure 5.2 illustrates what happens when an electron is taken from the localized impurity state and put into an unoccupied energy state at the surface of the Fermi sea. The energy needed for such a process is large, between about 1 and 10 electron volts for magnetic impurities. Classically, it is forbidden to take an electron from the defect without putting energy into the system. In quantum mechanics, however, the Heisenberg uncertainty principle allows such a configuration to exist for a very short time around $h/|\epsilon_0|$, where h is Planck's constant. Within this timescale, another electron must tunnel from the Fermi sea back towards the impurity. However, the spin of this electron may point in the opposite direction. In other words, the initial and final states of the impurity can have different spins. This spin exchange qualitatively changes the energy spectrum of the system. When many such processes are taken together, one finds that a new state, known as the Kondo resonance, is generated with exactly the same energy as the Fermi level as shown in Figure 5.2. The low-temperature increase in resistance was the first hint of the existence of the new state. Such a resonance is very effective at scattering electrons with energies close to the Fermi level as shown in Figure 5.1 (c). Since the same electrons are responsible for the low-temperature conductivity of a metal, the strong scattering contributes greatly to the resistance.

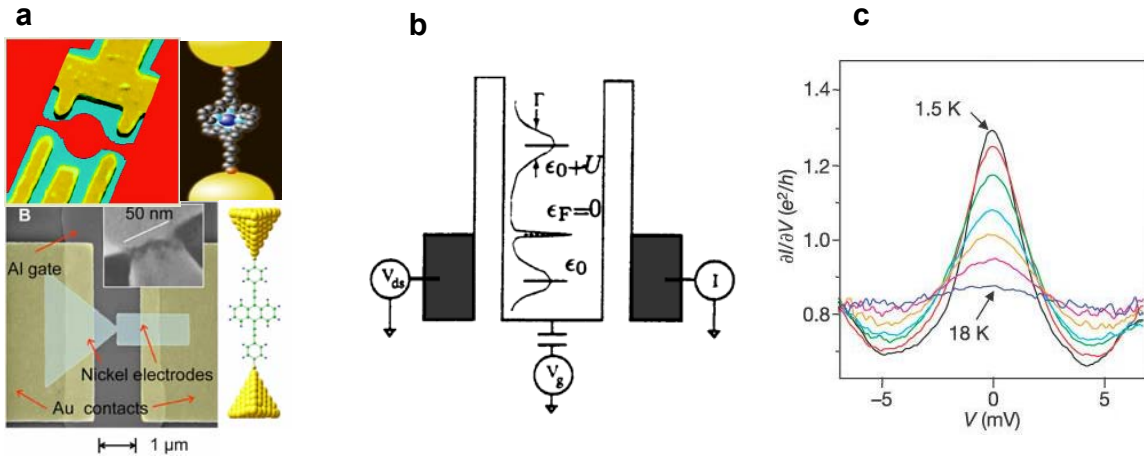


Figure 5.3: (a) Previous studied Kondo examples. (b) Simple device diagram with Kondo resonance state. (c) Conductance enhancement due to Kondo effect. [94]

It is important to note that the Kondo state is always “on resonance” since it is fixed to the Fermi energy. Even though the system may start with an energy, ϵ_0 , that is very far away from the Fermi energy, the Kondo effect alters the energy of the system so that it is always on resonance. The only requirement for the effect to occur is that the metal is cooled to sufficiently low temperatures below the Kondo temperature T_K .

In a metal, the electron states are plane waves, and scattering from impurities in the metal mixes electron waves with different momentum. This momentum transfer increases the resistance. In a tunneling structure, however, all the electrons have to travel through the device, as there is no electrical path around it. In this case, the Kondo resonance makes it easier for states belonging to the two opposite electrodes to mix as shown in Figure 5.1 (d). This mixing increases the conductance (i.e. decreases the resistance). In other words, the Kondo effect produces the opposite behavior in a tunneling device with impurities to that of a bulk metal.

The advent of nano-electronics allows physicists to control the number of electrons in quantum dot (QD) from odd to even [94, 95], enabling a situation very close to the predictions of single-impurity theories [96-99]. Quantum dots are often called artificial atoms since their electronic properties resemble those of real atoms. Several other studies

have also concentrated on very small devices such as carbon nanotubes and single molecular devices [100-102] as shown in Figure 5.3 (a), because it is believed that the smaller size of the devices and smaller number of conducting channels are critical to observe the Kondo effect [94]. In addition, most of these devices are coupled to a non-magnetic metal. In the following parts of this chapter, we present results on planar magnetic double tunnel junctions (DTJs) that can serve as a powerful tool to probe Kondo physics with reproducible and controllable Kondo temperatures (T_K), and so providing one means of investigating the interactions between impurities when spin dependent bands are formed at both the electrodes (the leads) and the impurities.

5.2 Kondo resonance in MTJs

Magnetic tunnel junctions (MTJs) are promising devices for data storage and field sensor applications. MTJs with MgO barriers exhibit giant tunneling magnetoresistance (TMR) effects which can exceed 220% at room temperature [17]. The TMR of typical MTJs decreases with increasing bias voltage and temperature [103]. Double tunnel junctions (DTJs) with three ferromagnetic (FM) electrodes give rise to a slower decrease of TMR with bias voltage by about a factor of two because the bias voltage across each junction is halved compared to a single junction device [104, 105]. There have also been theoretical predictions [106, 107] and experimental observations of increased TMR in DTJs and granular tunneling systems [108, 109] through Coulomb blockade effects. Another possible interesting feature is the Kondo assisted tunneling process at low temperatures [110]. This process was introduced to account for zero bias anomalies observed at low bias voltages and temperatures in non-magnetic planar tunnel junctions [111] via impurities in the tunnel barrier [90]. In their work, they assumed that there is no interference between the localized spin states of these impurities i.e. they are sufficiently far apart and dilute that the interaction between the impurities is negligible. A second observation was that the impurities need to be located close to or even inside one of the electrodes in order to observe the Kondo effect. In contrast to semiconductor dots, planar tunnel junction devices enable us to use various kinds of contacts, such as magnetic and superconducting electrodes, and makes it easier to control the coupling between the dots

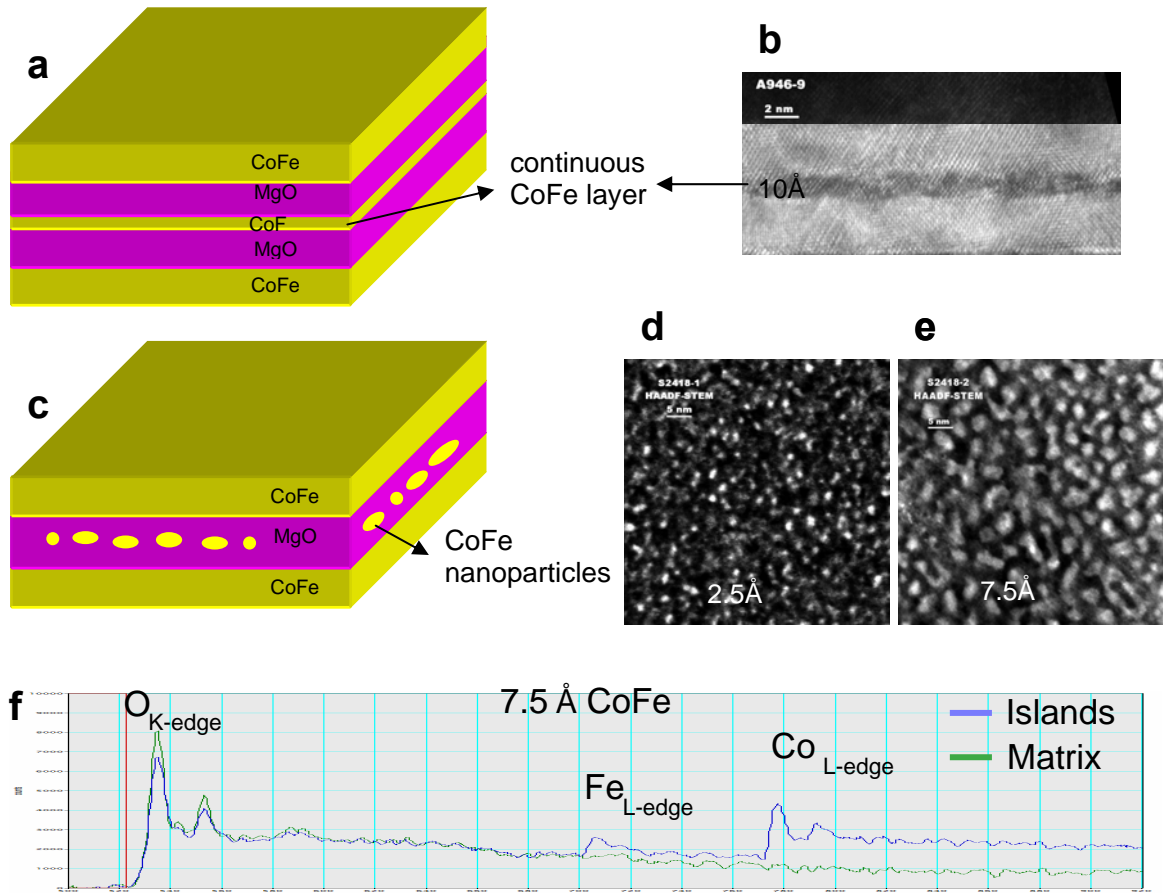


Figure 5.4: Schematic illustration of magnetic tunnel junctions with transmission electron micrographs (TEM). In this work double magnetic tunnel junctions are comprised of 100 Ta / 250 IrMn/ 35 Co₇₀Fe₃₀/ 25 MgO/ X Co₇₀Fe₃₀/ 25 MgO/ 70 Co₇₀Fe₃₀/ 150 IrMn/ 100 Ta, where all thicknesses in angstroms (Å). Active tunnelling area is $\sim 700\mu\text{m} \times 700\mu\text{m}$. (a) When middle CoFe thickness is above 10 Å. (b) TEM shows continuous layer of 10 Å CoFe. (c) When middle CoFe thickness is less than 10 Å, nanoparticles are formed. (d) scanning TEM (STEM) of 2.5 Å CoFe layer. (e) STEM image of 7.5 Å CoFe layer. (f) Electron Energy-Loss Spectroscopy data from 7.5 Å CoFe layer.

(here the impurities or defects in the tunnel barrier) and the electrodes due to well established multilayer growth techniques. The precision of the tunnel barriers is the order of one angstrom, which is impossible using conventional lithography and e-beam methods to define lateral structures. This well controlled strong coupling of the dots and leads in planar tunnel junctions make it easier to study Kondo physics at elevated temperatures and thus over a much wider range of temperature.

We investigated the magneto-transport properties, as a function of temperature and bias, of DTJs formed with MgO tunnel barriers and CoFe magnetic electrodes in which the middle electrode is so thin that it is discontinuous and is thus comprised of small CoFe nanoparticles. Schematic sample structures are shown Figure 5.4 (a) and (c). The CoFe middle layer is continuous above 10 Å, as shown in the XTEM micrograph in Figure 5.4 (b), whereas planar transmission electron microscope (TEM) pictures for 2.5 Å (Figure 5.4 (d)) and 7.5 Å (Figure 5.4 (e)) thick CoFe layers show a three dimensional growth of CoFe because of the poor wetting of CoFe on MgO. Electron Energy-Loss Spectroscopy (EELS) data in Figure 5.4 (f) from each dot show clear evidence for Co and Fe but do not have enough energy resolution to address whether or not the CoFe dots are much, if at all, oxidized.

As the temperature is reduced, the central CoFe layer forms virtual bound resonance states due to interaction with the tunneling electrons. Moreover, the Coulomb blockade (CB) effect arises due to the discrete quantized energy levels which suppresses transport. The formation of energy gaps in the DOS around the Fermi level due to the CB effect results in a steep increase of resistance. As a result, as shown in Figure 5.5 (d) and (e), the resistance of a DTJ with a 4.5Å CoFe thick middle layer at zero bias increases over 60 times compared to less than 2 times (see Figure 5.5 (a) and (b)) for a single tunnel junction (STJ) as the temperature is reduced from room temperature (RT) to low temperatures (LT: ~2.5 K). The STJ is composed of only one MgO barrier and two electrodes. The virtual bound resonance in the CoFe middle layer could act not only as an intermediate state, but also as a spin-flip center. The localized states act as a bridge between the exponential tails of the wave functions of the conduction electrons on opposite sides of the junction, effectively decreasing the size of the barrier [99]. When the spin of nanoparticles is coupled to the spin polarized conduction electron of the FM electrodes, new phenomena such as the TMR dip emerge [112] as shown in Figure 5.5 (f).

The size of the CoFe dots formed in the middle electrode layer was confirmed by measurements of the blocking temperature of the magnetic moments of these dots. When the dots are sufficiently small in volume their magnetization exhibits a

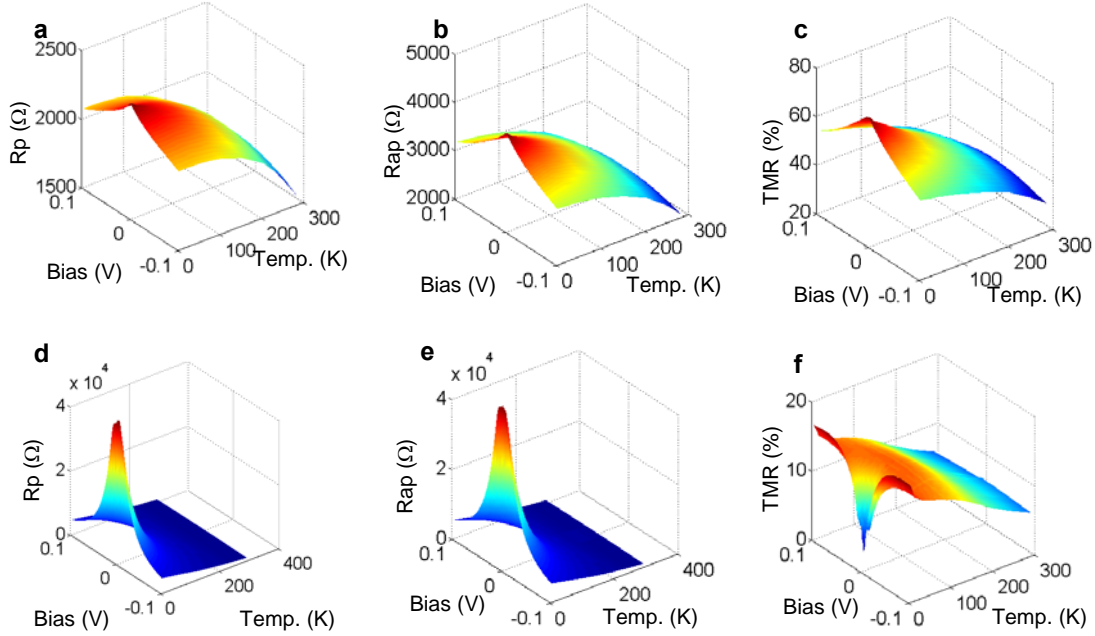


Figure 5.5: Signature of Coulomb blockade and TMR suppression in a DTJ. Magnetic fields of -500 and +10,000 Oe were applied to set the state of the junction in the AP and P states, respectively. Single tunnel junctions were prepared with same method as DTJ, consisting of 100 Ta / 250 IrMn / 35 Co₇₀Fe₃₀ / 28 MgO / 70 Co₇₀Fe₃₀ / 100 Ta, where thicknesses are in Å. TMR, typically defined as $(R_{AP}-R_P)/R_P$, where R_{AP} and R_P are the resistances for anti-parallel (AP) and parallel (P) alignment of the magnetic moments, respectively. (a) R_P change of STJ with temperature and bias. (b) R_{AP} change with temperature and bias. (c) corresponding TMR of STJ shows highest value at low temperature and zero bias. (d) R_P change with temperature and bias of DTJ with 4.5 Å thick middle CoFe layer. (e) R_{AP} change with temperature and bias of same DTJ. (f) TMR of DTJ shows a dip at low temperature and low bias.

superparamagnetic behavior as shown in Figure 5.6 (a) for nanoparticles formed from a 5 Å thick CoFe layer. The increase in resistance, presumed to arise from the Coulomb blockade effect for different nanoparticle sizes, is shown in Figure 5.6 (b). As the sample is cooled, the smaller nanoparticles show a step increase in resistance which saturates due to the competition between Coulomb blockade and the Kondo effect. Even though FM from the electrodes are expected to suppress Kondo assisted tunneling [113, 114], we observe a peak in the conductance in the DTJs with CoFe nanoparticles shown in Figure 5.6 (c) at low bias voltages and temperatures in addition to the strong suppression of TMR, shown in Figure 5.5 (f), in the same bias voltage and temperature regime as

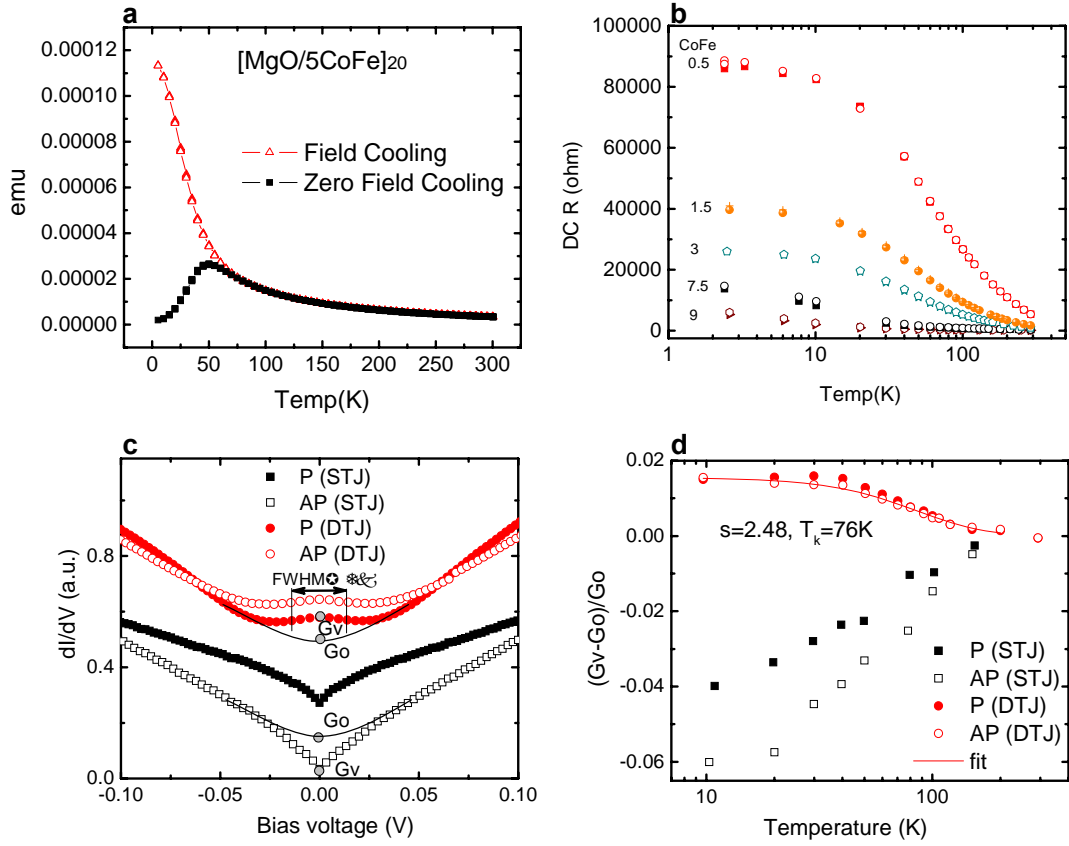


Figure 5.6: (a) Field cooled and zero field cooled magnetization versus temperature for 5 \AA thick CoFe middle layers in MgO based MTJs. (b) DC resistance at zero bias vs temperature for different thicknesses of the CoFe middle electrode and consequently, the nanoparticle size. Open (filled) symbols correspond to R_P (R_{AP}). (c) Differential conductance with 5 \AA middle electrode at 2.5 K. (d) Maximum excess conductance ratio with 2 \AA middle electrode is calculated from $(G_V - G_0)/G_0$, where G_V is experimental conductance data at zero bias and G_0 is the minimum of fitted background. This excess conductance of DTJ is saturated to a maximum value well below T_K . The line is a fit of the excess G as a function of temperature using the formula $G_K(T) = G_0 / (1 + (2^{1/s} - 1)T^2 / T_K^2)^s$, yielding $T_K = 76\text{ K}$ and $s = 2.48$.

expected theoretically [112, 115]. We investigated different kinds of middle layers, such as Au, Pt, Cu, CrMo, NbN, IrMn, and Ni. In the case of 3, 5, 7 \AA Au and 2 \AA Pt middle layers, there was no conductance peaks. On the contrary 5 \AA Cu, CrMo, NbN, IrMn and Ni middle layers showed conductance peaks. All these samples showed large resistance

changes from RT to LT due to Coulomb blockade effects from the nanoparticles, but no spin dependent tunneling phenomena was observed in any of these cases, except for Ni. Hence, there is almost zero TMR even at LT and thus no TMR dip.

These results suggest that the conductance peaks arise from the interaction of spins between the localized moments in the ferromagnetic dots and the conduction electrons. These features are strongly reminiscent of Kondo resonance effects previously observed in lithographically defined quantum dots [94] and C_{60} molecules placed between FM electrodes [116]. For temperatures much larger than T_K , the enhanced conductance disappears due to thermally activated transport. For elevated voltages above 30mV, the electrons at one electrode can no longer tunnel into the other electrode via localized states in the middle electrode as the separation of the energy levels between the two electrodes and the Kondo states is increased. Hence, the conductance peak at zero bias disappears. [94]

At LT, there is a conductance inversion for the DTJ shown in Figure 5.6 (c) between P and AP configurations around zero bias as predicted [112, 114]. This does not happen in a STJ. We observed this negative MR effect in alternating-current (a.c.) measurements with 5 Å nanodots as well as with 0.5 Å nanoparticles in direct-current (d.c.) measurements (see Figure 5.7 (b)) where the TMR suppression is over 100% indicating negative TMR. The solid lines in Figure 5.6 (c) represent the calculated background, G , fitted by a 2nd order polynomial.

We can clearly see the conductance development of DTJ and STJ is in the opposite direction to the background signal. The height of the zero bias resonance decreases logarithmically with bias between 10 mV and 20 mV. The temperature evolution of enhanced conductance is depicted in Figure 5.6 (d), which also shows logarithmic behavior at temperatures from 40K up to 100K, which is a typical signature of the Kondo effect. The net conductance enhancement, assuming the background as that of STJ, is always larger in AP than P (as in Fig. 3d) because spin flip (10-60% of incident electron) creates additional channels in the AP case than in the P case.

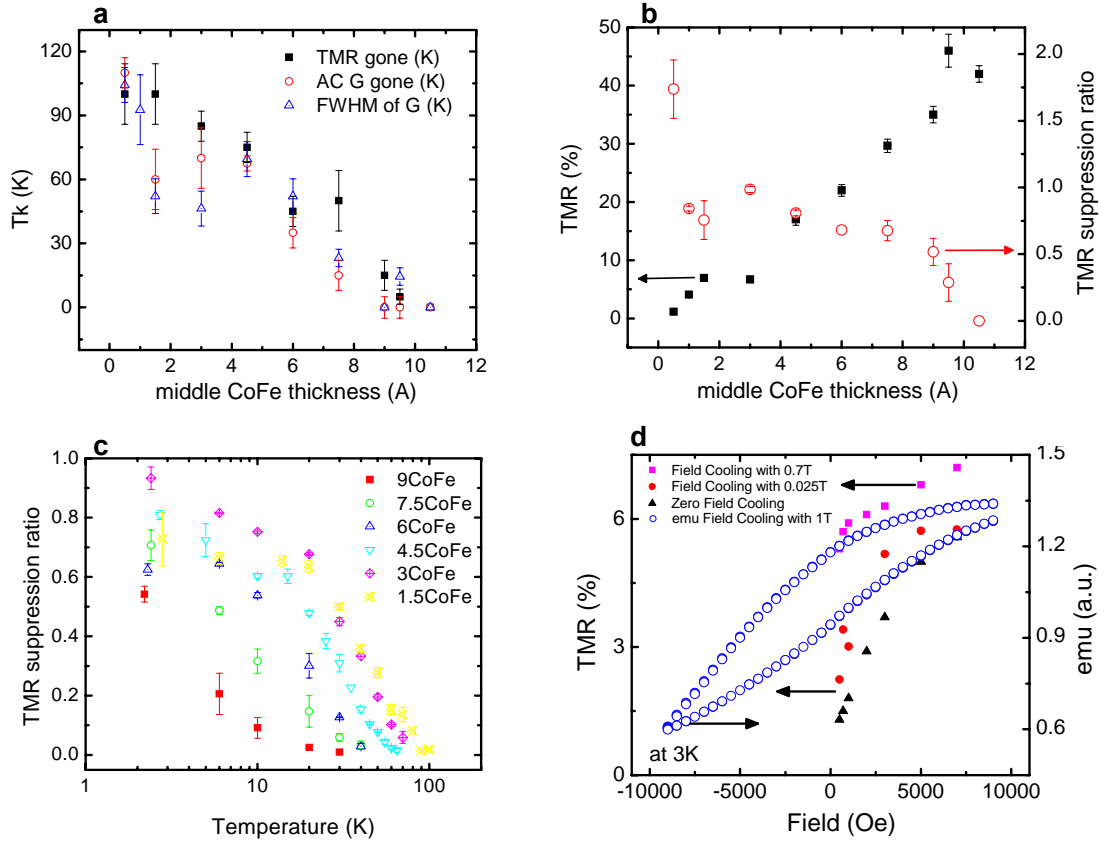


Figure 5.7: Nanoparticle size of middle CoFe layer effect. (a) Kondo temperature (T_K), defined by three different methods. (b) The maximum TMR and TMR suppression ratio change with the size of nanoparticles. TMR suppression ratio is defined by the ratio between maximum TMR and TMR at zero bias. (c) TMR suppression evolution with temperature. (d) TMR and magnetization as a function of magnetic field from 100 MgO | 150 Ta | 40 CoFe | 23 MgO | 5 CoFe | 23 MgO | 150 Ta.

We compared the Kondo temperature (T_K) derived from three different methods; first, at what temperature the enhancement of the conductance disappears, second, at what temperature the TMR dip disappears, and finally from the spectral width of the enhanced conductance. The spectral width of the Kondo resonance scales proportionally with T_K . We used full-width at half-maximum (FWHM) as $2k_B T_K/e$, where k_B is the Boltzmann constant and e is electronic charge. Even though our samples show slightly different values of T_K depending on which junction on a single wafer is studied, all three methods show reasonably good agreement, as shown in Figure 5.7 (a).

The T_K distribution from different junctions on the same wafer may be due to the inhomogeneous grain size as well as different interactions among the impurities, which is reported on the atomic scale [117]. However, our T_K is about an order of magnitude higher than that of mesoscopic devices, indicating that the coupling between the localized states and the middle layer is very strong, even if localized electrons do not contact with conduction electrons i.e. the local moment is isolated between two insulators. This could be attributed to the highly oriented (100) MgO tunnel barrier shown in Figure 5.4 (b), similar to the oriented crystal effect [118].

In the thin ($<4 \text{ \AA}$) CoFe middle layer cases, the maximum TMR at LT is small ($<10\%$), but the TMR is almost suppressed as shown in Figure 5.7 (b). This smaller TMR is mainly due to the fact that the nanoparticles are hard magnets which require very large fields to align. Therefore the cooling field of 1T is not enough to align the moments of the nanoparticles, as shown in Figure 5.7 (d). As the thickness of the middle CoFe layer increases, the TMR suppression and conductance enhancement are weakened and eventually disappear when the CoFe layer's thickness is increased to 10 \AA . This is in good agreement with theory [113] that T_K decreases with increasing spin polarization. This is due to increased interactions [119] between the moments in the middle CoFe layer, therefore, it is more favorable energetically to form a spin singlet with the other local moment than to form a Kondo singlet [120], giving rise to complete suppression of the Kondo effect. Complete magnetic ordering is presumed to eliminate the Kondo effect because the Kondo effect is overcome by the Ruderman-Kittel-Kasuya-Yosida (RKKY) interaction. The temperature dependence of TMR suppression is shown in Figure 5.7 (c). With small CoFe nanoparticles, the TMR suppression is maintained up to higher temperatures than with thicker CoFe middle layers, which is consistent with the values of T_K shown in Figure 5.7 (a).

The conductance is plotted in Figure 5.8 for different middle CoFe layer thicknesses. As the middle CoFe layer become thicker ($>5 \text{ \AA}$), charge fluctuations start to play a role, the Kondo peak shows a visible splitting and the conductance at zero bias is then completely suppressed above 10 \AA as expected [113, 114]. Our devices are close to the asymmetric coupling case between free electrons in the electrodes and isolated electron in the middle

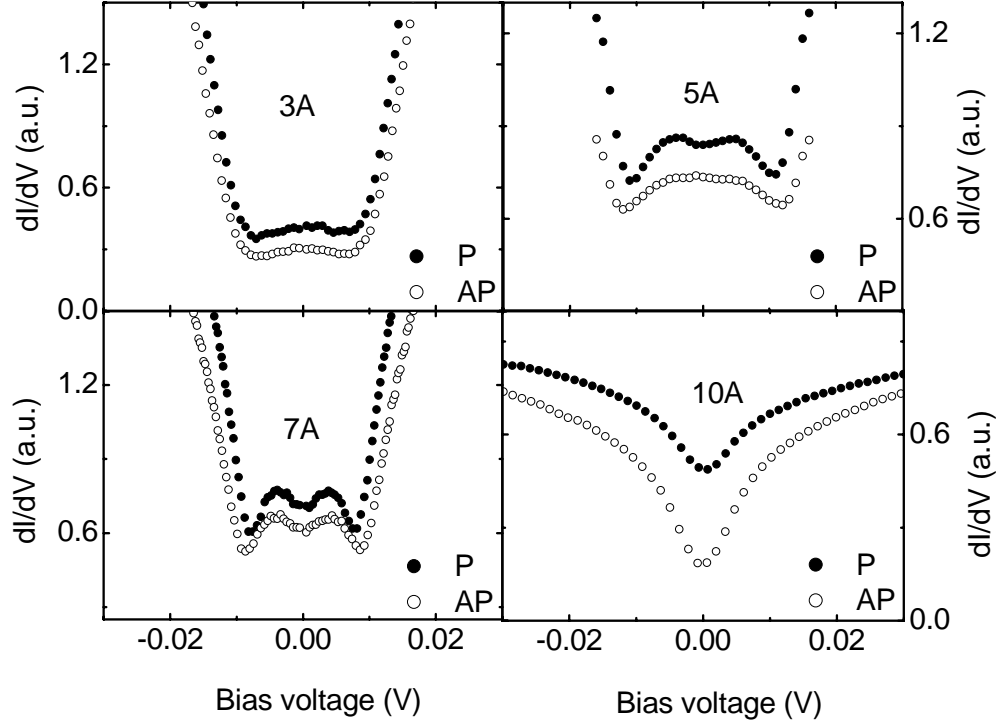


Figure 5.8: Measured conductance at 2.5K with different middle CoFe layer thicknesses.

CoFe nanoparticles because the FM layer thickness of the side electrodes is different and it turned out that the top MgO barrier is thinner than the bottom layer because the top MgO layer first fills the space between the CoFe nanoparticles and then forms barrier. In the case of the 5 Å middle layer, the Kondo effect is more robust against spin flips in the AP configuration than in the P alignment [121], therefore only the DC conductance of P configuration shows a Coulomb blockade-type dip [122] centered at zero bias. In the devices with a middle CoFe layers less than 5 Å, the Kondo effect is too strong to be weakened by the CB effect. With 7 Å thick middle layers, however, the quantization levels in the impurities is much closer, enabling more spin-flip processes in both the P and AP cases. The Kondo resonances are suppressed when taking into account the spin-flip process [123]. In the same junction, the FWHM of the enhanced conductance, proportional to T_K of the AP states, is always wider than that of the P, indicating impurity local density of state in the AP is wider and larger in amplitude.

There is another possible way to explain the suppression of the enhanced conductance which is due to interactions between magnetic scatterers [119]. CoFe atoms start to couple as the thickness of middle CoFe layer increases. These larger magnetic clusters give rise to the competition between the zero bias anomaly (ZBA) of the conductance-dip type which happens above 10 Å for the middle CoFe layers and the ZBA of the conductance-peak type (Kondo effect), dominant in the junctions with CoFe middle layers less than 5 Å.

Even though we observed the splitting of the conductance peak irrespective of magnetic fields as explained above, there was little effect on the splitting of the enhanced conductance with magnetic fields, one of the distinctive signatures of the Kondo effect. One needs to apply a magnetic field comparable to the peak width, which is too large (tens of Tesla) in our case. Instead we observed the broadening of the conductance peak with magnetic fields, leading to a g-factor value of 1.87.

In summary, in recent years there has been a revival of interest in the Kondo effect because of new methods to fabricate small nano-devices which contain small and countable numbers of electrons. Devices which contain small numbers of electrons and, especially, with net spins of $\pm \frac{1}{2}$, are thought to be candidate quantum bit (Q-bit) devices for quantum computers. The ability to manipulate the spin of the electron as well as its charges is expected to provide a foundation for entirely new computational paradigms. In our studies of magnetic double tunnel junctions we have shown that at low temperature a virtual bound resonance state is formed at the Fermi level due to the interaction between localized impurities of the middle CoFe layer and conduction electrons in the other two electrodes [124]. This resonant scattering contributes higher order tunneling processes including spin flipping, thereby enhancing the conductance but decreasing the TMR. This is opposite behavior to that of a bulk metal.

Chapter 6. Impurity assisted resonant tunneling

6.1 Motivation

The TMR of MTJs typically increases with anneal treatments, likely due to improved properties of the tunnel barrier and the interface between the barrier and the ferromagnetic electrodes. However, the TMR is observed to decrease drastically above some characteristic annealing temperature, typically above $\sim 400^\circ\text{C}$ in MTJs exchanged biased using IrMn and PtMn antiferromagnetic layers. One reason might be due to diffusion of Mn from these layers into the barrier, possibly leading to the formation of Mn oxide [125]. In addition to Mn oxide, it is also possible that other oxides are formed at the interface between the MgO barrier and the ferromagnetic electrodes, for example, CoO. For these reasons we have explored the properties of MTJs in which we have inserted thin insulating antiferromagnetic (AF) layers formed from oxides of Mn, Ni and Co at the MgO interfaces. These oxides have similar simple cubic structures to MgO and grow epitaxially on MgO (100) as shown in Figure 6.1. In this Chapter, we report the magneto-transport properties, as a function of temperature and bias, of MTJs grown with barriers formed from double layers of MgO/ [NiO, CoO or MnO] as well as triple layers of MgO/[NiO, CoO or MnO]/MgO. The Ni/O ratio was optimized by varying the O_2 content of the sputter gas and the power applied to the magnetron. Rutherford backscattering spectrometry (RBS) analysis shows that NiO layers deposited in Ar- O_2 with $\sim 10\%$ O_2 are stoichiometric within experimental error (50.8 ± 0.5 atomic % O).

We find that the insertion of thin layers of NiO, CoO or MnO in the MgO barrier results in dramatic changes in the TMR. The magnitude of the TMR is significantly decreased independent of whether these layers are inserted at the MgO interfaces or within the interior of the MgO layer. More importantly, the sign of the TMR can even be changed,

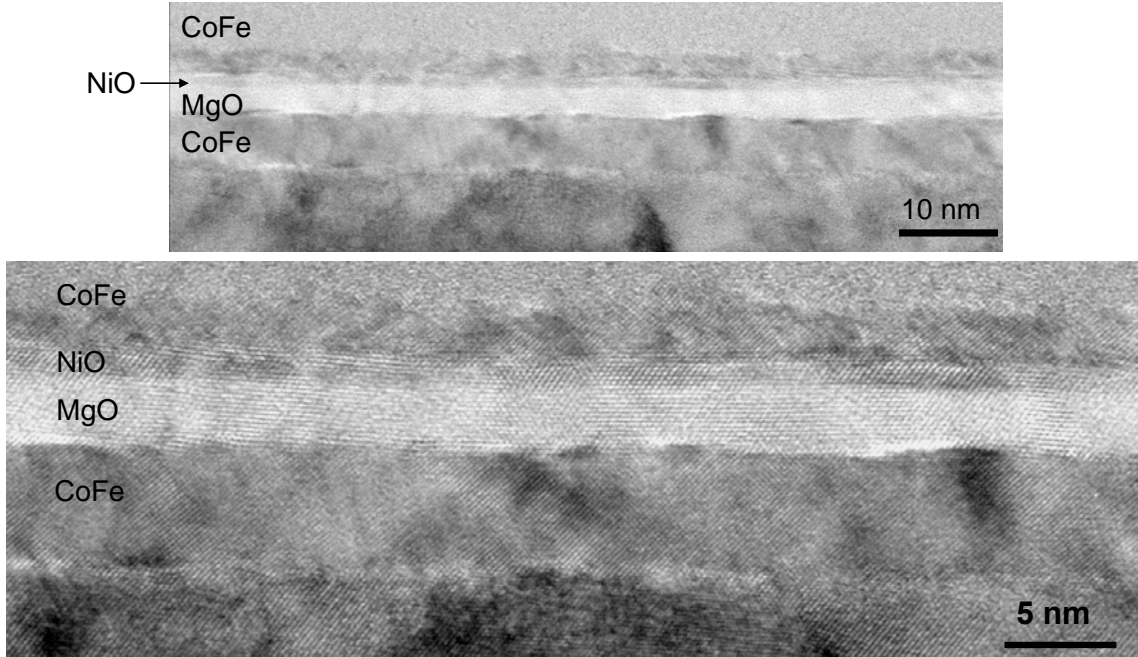


Figure 6.1: TEM images with low (upper panel) and high magnification (lower panel) for the following MTJ structure: IrMn | 60 CoFe(70/30) | 8 Mg | 25 MgO | 10 NiO | 25 CoFe(70/30) (in Å). The image is courtesy of Titus Leo, Arizona State University.

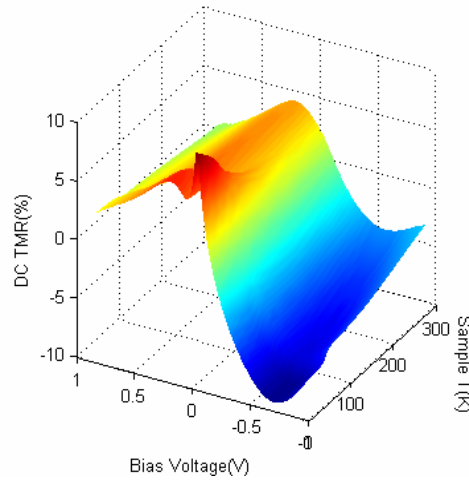


Figure 6.2: The voltage and temperature dependence of TMR from an MTJ with a structure of CoFe/MgO/4Å NiO/CoFe.

resulting in *negative* TMR under certain bias voltage conditions. A typical example is shown in Figure 6.2, where results are included for the structure of the form CoFe/MgO/4Å NiO/CoFe. In this case, highly asymmetric bias voltage dependence is found with negative TMR at negative bias voltages above -200meV. Here negative bias voltage corresponds to electrons tunneling from the CoFe/MgO interface into the NiO/CoFe interface. We observe negative TMR, even at room temperature. We also observe at low temperatures, a significant dip in TMR at small positive bias voltages (~90 meV) which broadens and disappears as the temperature increases above 70K.

6.2 Voltage dependence of TMR

Using any tunnel barrier material in a magnetic tunnel junction, including MgO, it is observed that the TMR decreases with increasing bias voltage. Zhang *et al.* [83] proposed that this was a result of inelastic scattering by magnon excitations at the ferromagnet/insulator interface. Hot electrons, which overcome the barrier, arrive at the second ferromagnet/insulator interface and then lose their energy by emitting a magnon and thereby flipping the electron spin. With increasing bias voltage, more magnons can be emitted, resulting in the reduced TMR values. The energy dependence of the spin polarization due to band structure effects may also reduce the TMR at high bias. [80] Assuming two parabolic bands in the free electron model, Figure 2.5 shows the calculated dependence. Because just a few monolayers in the electrode adjacent to the ferromagnet-insulator interface dominate the magnetotransport properties of MTJs, changes in the electronic structure of the ferromagnet, such as DOS of different crystalline phase of the same material, influences the variation of TMR versus the applied voltage. [126]

However, investigating the electron tunneling between a Co(0001) surface and an amorphous tip across a vacuum barrier with a spin-polarized STM, Ding *et al.* [127] observed an almost constant TMR with bias voltage. Thus, the zero-bias anomaly in planar tunnel junctions with insulator barriers can be attributed to defect scattering in the barrier, rather than to magnon creation or spin excitations at the interfaces. This

observation strongly suggests that the voltage drop in TMR is due to localized states in the barrier. [6, 7] Along with the fact that actual tunnel junctions contain large amounts of disorder in the electrodes, in the barrier, and at the electrode/barrier interfaces, recent reports also support this contention by showing that the effective tunneling barrier height is much smaller than expected, even in the high TMR samples using MgO barriers. [17, 64]

To understand the voltage dependence of TMR, various experiments were carried out in artificially engineered structures. The addition of a nonmagnetic metal interface layer causes a very asymmetric bias voltage dependence of TMR as a signature of the development of quantum well states. [128] This quantum well effect is also reported in Fe ultrathin layer [129] and the epitaxial fcc Co/Cu(001) system [130].

The controlled modification of the electrode DOS by dusting with Cr and Ru in Co/Al₂O₃/Co tunnel junctions leads to a strong dependence of TMR on applied voltage. [131, 132] The creation of virtual bound states (VBS) due to the *s-d* wavefunction hybridization for impurity concentrations lower than 10% induces DOS modification. [133]

Asymmetric barriers from over or under-oxidation also can lead to a strongly asymmetric bias voltage dependence. [134] A Cu-AlO_x intermixing zone also develops a large asymmetry upon annealing. [135] Sharma *et al.* [136] used composite barriers and reported that the TMR shape versus voltage is dependent on the barrier oxidation time, indicating some role played by the barrier defects, possibly spin flip scattering.

The effect of disorder on tunneling also leads to resonant tunneling via localized electronic states which are formed in the barrier in the presence of impurities or defects. These resonant states are coupled to the propagating states in the electrodes by diffusive and relaxation processes, which provide additional conduction channels. Under these conditions the electronic structure at the electrode/barrier interfaces may control the tunneling current. [6] The resonant states exist as spikes, so called “hot spots”, in the conductance distribution at particular k_{\parallel} -points in the two-dimensional Brillouin zone. [137] The width of these spikes is determined by the strength of the coupling to the propagating states. The existence of enhanced tunneling at particular k -points affects a

voltage response of the tunneling current, and hence may give rise to asymmetric TMR curves. With increasing disorder the conductance of the minority spins increases dramatically, while that of majority spins is insensitive to disorder, which leads to a decrease in the TMR and sometimes negative TMR. [138] In real MTJs, with strongly disordered tunnel junctions, the tunneling current may flow through a few regions of the insulator where local disorder provides highly conducting channels for electron transport. This mechanism of conduction leads to a broad distribution of the tunneling current. Tsymbal and Pettifor [138] predicted a decrease in the spin polarization of the tunneling current with disorder and insulator thickness. The fact that the TMR of thicker MgO barrier above 30Å tends to decrease strongly suggests there is disorder inside our MgO barrier, identified by localized spikes in the tunneling current from STM measurements [139]. Interestingly, Tsymbal and Pettifor found that the TMR is in agreement with Julliere's formula, in which $P_{1,2}$ is defined as the spin polarization of the tunneling current from the ferromagnet to a non-magnetic metal. This might explain the success of the Julliere's formula when comparing the TMR magnitudes with the spin polarization values measured in experiments on superconductors. [6]

The degree of disorder can be tuned by either the number of resonant states or the incident energy of electrons by varying the applied voltage. We note that disorder breaks the symmetry of the system and mixes the propagating Bloch states in the leads. This makes it possible for the states which are not able to tunnel effectively through the barrier in the perfect tunnel junction by symmetry to be mixed with the states which are and therefore to be involved in transport. [6] DOS modification demonstrated by LeClair *et al.* [131, 132, 140] can be understood from the fact that disorder produces an electronic structure at the electrode/barrier interfaces which control the tunneling current.

Disorder in the barrier broadens the conduction and the valence bands of the insulator and creates localized electronic states within the band gap. The broadening of the bands reduces the effective potential barrier and negatively influences the spin polarization of tunneling electrons in MTJs according to Slonczewski model [18]. If the applied bias is tuned to excite the localized impurity or defect states, resonant tunneling occurs. The

conductance per spin from a simple one-dimensional model for impurity assisted tunneling is given by [141]

$$G = \frac{4e^2}{h} \frac{\Gamma_1 \Gamma_2}{(E - E_i)^2 + (\Gamma_1 + \Gamma_2)^2} \quad (6.1)$$

where E_i is the energy of the impurity state, and Γ_1 and Γ_2 are the leak rates of an electron from the impurity state to the left and right electrodes. For simplicity we assume the leak rate is proportional to the DOS of the electrodes, ρ_1 and ρ_2 , at the left and right interfaces, so that $\Gamma_1 \propto \rho_1 \exp[-2\kappa x]$ and $\Gamma_2 \propto \rho_2 \exp[-2\kappa(d-x)]$, where κ is the decay constant and x is the position of impurity within the barrier of thickness d . Off resonance, when $|E - E_i| \gg \Gamma_1 + \Gamma_2$, the spin conductance is given by $G \propto \rho_1 \rho_2$ leading to normal TMR from Julliere's formula. At resonance, when $E = E_i$, the conductance is inversely proportional to the DOS of the one of the ferromagnets, which results in the sign inversion of the TMR. Thus, the spin-dependent leak rates under resonant conditions invert the effective spin polarization of one of the electrodes. [142]

6.3 Resonant inversion of TMR from MgO/NiO(or CoO) barriers

NiO is one of the materials which were explored to make tunnel barriers in the early 80s. However, MTJs showed very small TMR (<2.5%), even at low temperature (4.2K). [143] As demonstrated by Doudin *et al.* [144], electrodeposited Ni/NiO/Co junctions exhibit two-level fluctuations of the electrical current, indicating impurity/defect-driven transport. By performing measurements on a large number of samples and comparing experimental and calculated statistics, Tsymbal *et al.* [142] reported that the TMR is inverted when the energy of a localized state in the barrier matches the Fermi energy of the ferromagnetic electrodes. Here we report very strong bias voltage dependence of TMR in MgO/NiO (or CoO) junctions, hence giving rise to -12% TMR under specific bias conditions. Surprisingly, we have observed resonant tunneling phenomena in large area planar junctions, even up to room temperature in a very controllable and repeatable

fashion, in contrast to previous observations and expectations [142]. Previous resonant tunneling reports all attribute their features to the unknown midgap impurities located randomly in the barrier. [142, 145, 146] In our samples, however, the spatial impurity position, hence the leak rate is controlled by thin film deposition, and the energy of the defect state is identified by inelastic electron tunneling spectroscopy (IETS).

Figure 6.3 displays the bias dependence of TMR and IETS signals from samples with different barrier thicknesses. Without any NiO layer, the TMR curve of Figure 6.3(a) is symmetric and shows a large MR ratio, up to 130% at 2.8K, as grown (no anneal). IETS data in Figure 6.3(b) from the same sample also shows very symmetric features versus bias voltage and have broad peaks around $\pm 500\text{mV}$, which are identified as the minority spin Δ_1 band of MgO [82] with CoFe electrodes [84]. For a more explanation of this peak, please see Chapter 3.4. The strong peak at $\pm 83\text{mV}$ can be associated with the excitation of longitudinal-optical surface modes [77] while the smaller maximum at $\pm 27\text{mV}$ is attributable to an optical phonon mode of MgO [44]. As the thickness of NiO increases, the influence of the Δ_1 band edge on the IETS signal is reduced and new features at 17-23mV and $\pm 60\text{-}70\text{mV}$, which are dominant peaks with 6Å and 8Å NiO, are developed. The energy levels of the new features tend to increase slightly with thicker NiO layer. The tunneling current is dominated by electrons with momentum vectors that are exactly normal to the barrier because the tunneling probability decreases rapidly when the momentum vectors deviate from the barrier-normal direction, especially in a thick MgO barrier. On the other hand, if the barrier is thin enough, electrons with momentum vectors deviating from the $k_{\parallel}=0$ point can have a finite tunneling probability. Therefore, the peak from the minority spin Δ_1 band of MgO is most prominent in the sample with a simple MgO barrier and then the peak intensity decreases with thicker NiO because we fixed the total barrier thickness and the barrier height for NiO is smaller than MgO. With 4 Å NiO, a clear asymmetric bias dependence of the TMR is visible with a maximum negative TMR of -12% occurring at 2.8K.

This asymmetric and negative TMR effect can be thought of as a barrier profile effect [147] due to asymmetric barriers and can be calculated based on Slonczewski's model [18]. The electron wavefunction matching at interfaces is significantly affected by the

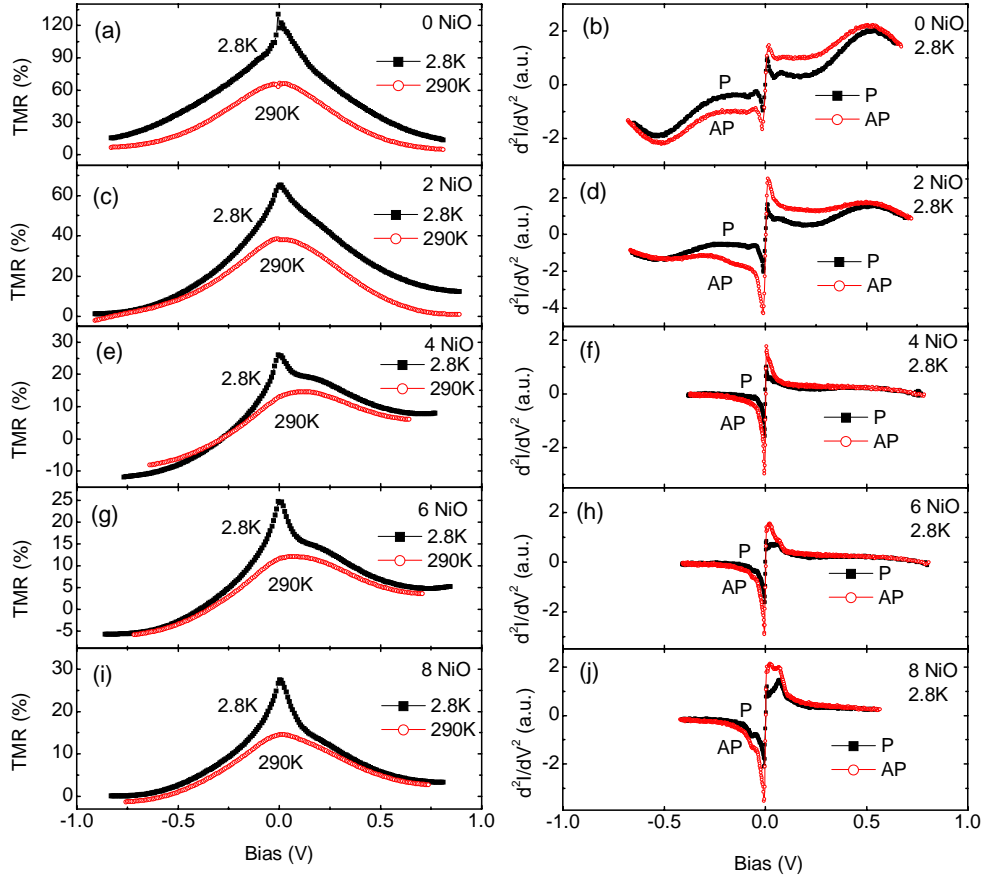


Figure 6.3: Bias dependence of TMR (left column) and IETS data (right column) from an MTJ with a structure of CoFe/yMgO/x NiO/CoFe ($x+y=27\text{\AA}$). All the samples are unannealed.

barrier height and shape. This in turn results in a different bias dependence for the conductance, such that the AP configuration has higher conductance than the P state for voltage biases above the transition bias (V_c), at which point the TMR changes from positive to negative. The calculation suggests that the lower the barrier height, the smaller the transition bias will be [148]. The effective barrier height decreases with thicker NiO since we fixed the total barrier thickness. However, the transition bias is increasing from 4\AA to 8\AA of NiO thickness in the opposite way to the calculation. Therefore, we rule out the possibility of the barrier shape effect.

Introducing less than one monolayer of NiO, which is the case in Figure 6.3(c, d), has a small effect in terms of asymmetric TMR. With 4Å NiO the TMR develops the largest negative asymmetric behavior, and then this effect is reduced as we further increase the NiO thickness. Within the understanding of the barrier profile effect, a more asymmetric barrier should give rise to a larger asymmetric effect. This also implies that our observation cannot be understood simply on the basis of the barrier shape effect.

The observed TMR shape can be explained by resonant tunneling via localized states in the NiO barrier as a similar resonant effect was reported in Ni/NiO/Co nanojunctions [142], Fe/ZnSe/Fe [146], and MnAs/GaAs(AlAs)/MnAs [145]. In these observations the authors cannot identify the origin of the impurity, the location of the impurity, or the energy level of the impurity. The excited energy levels in IETS at 17-23mV and 60-70mV with a NiO layer gives the impurity energy, which is similar to the previously reported energy, 35-55mV [142, 145, 146] even though these values were calculated values. By changing the barrier order (MgO and NiO), we confirmed that the asymmetric TMR shape is flipped with respect to the bias voltage, as shown in Figure 6.4(a), which suggests that the NiO layer is indeed the origin of this inversion of TMR. In our sample the spatial location of NiO layer is close to one of the electrodes which is a very important condition for negative TMR. [146]

On the other hand, moving the defect states towards the middle of the barrier, hence $\Gamma_1=2$, the TMR shape recovers its symmetric features and the negative TMR disappears, as shown in Figure 6.4(b). However, we are still able to detect a broad IETS peak at (41mV in Figure 6.4(d), which is symmetric in bias voltage. One of the interesting features from 12Å MgO/4Å NiO/12Å MgO barrier is the temperature dependence of TMR in Figure 6.4(c). In the barriers formed from double layers of MgO/NiO, the TMR at zero bias increases only two times from room temperature to low temperature (2.8K). However, the magnitude of TMR from a triple layer barrier (MgO/NiO/MgO) reaches over 50% at 2.8K, which is only 1% at room temperature. This is due to the Coulomb blockade effect from the thin NiO layer as shown in the resistance measurement in Figure 6.4(c). As the temperature is reduced, electrons tend to skip the NiO layer and the effective barrier thickness becomes the sum of two MgO layers. This also validates that

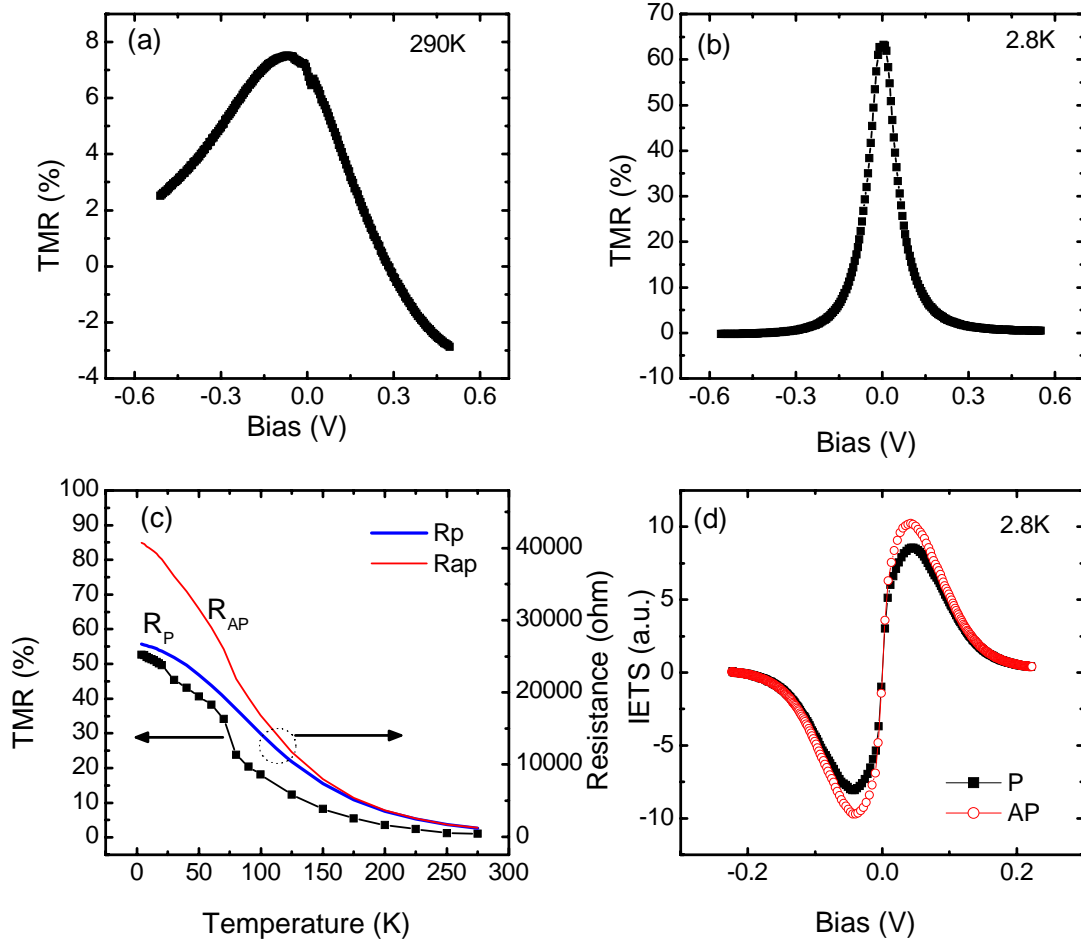


Figure 6.4: (a) Voltage dependence of TMR from a sample of CoFe/4Å NiO/25Å MgO/CoFe at 290K. (b) Voltage dependence of TMR from a sample of CoFe/12Å MgO/4Å NiO/12Å MgO/CoFe at 2.8K. (c) Temperature dependence of TMR and junction resistance at zero bias from the same sample as (b). (d) IETS data from the same sample as (b) at 2.8K.

the resonant TMR inversion is due to the spatially asymmetric impurity location.

In order to confirm the existence of impurities in the NiO layer, we annealed the sample at two temperatures, 260°C and 400°C, for 30 mins each. After annealing at 260°C, the TMR increases up to 90% and the negative TMR almost disappears, and the Δ_1 peak in IETS starts to grow. Upon annealing at 400°C, the TMR shape changes into a more symmetric one and the TMR shows 160% at 2.8K. In addition, the IETS signal shows a

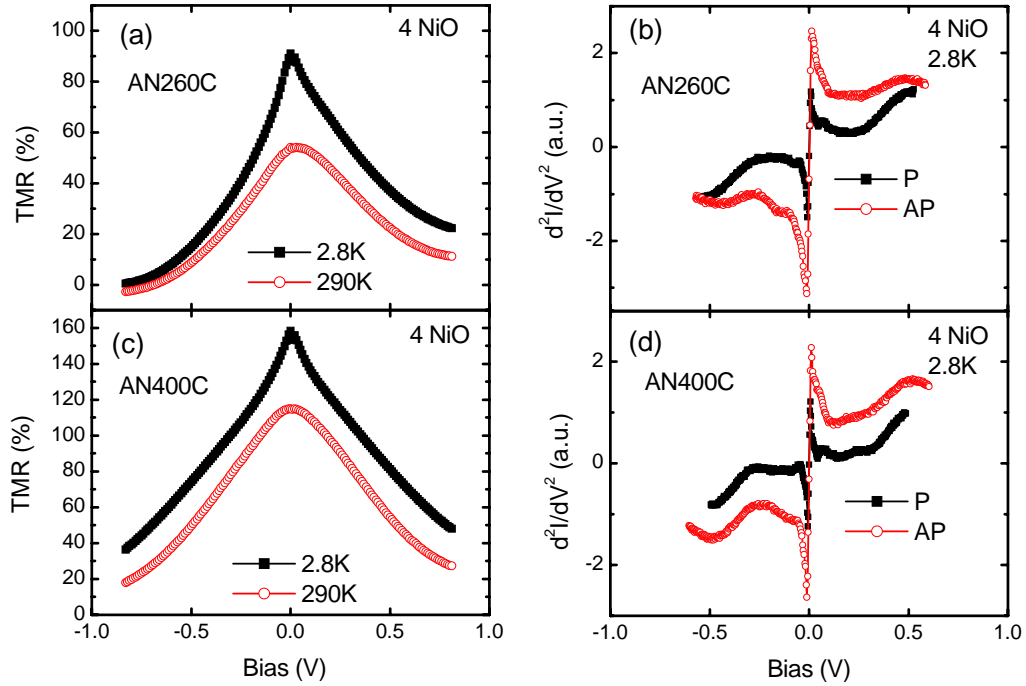


Figure 6.5: Voltage dependence of the TMR and IETS from an MTJ with a barrier of MgO/4 Å NiO annealed at 260°C (a, b) and 400°C (c, d).

large Δ_1 peak around ± 500 mV, which is similar to the unannealed single MgO barrier shown in Figure 6.3(b). The annealing treatment reduces the number of defect states, thereby enhancing the TMR and recovering the Δ_1 feature in IETS.

As we increase the thickness of NiO beyond 4 Å, the magnitude of the negative TMR as well as the positive TMR diminishes. In addition, the broad transition from positive to negative TMR is quite different from that previously reported [142, 145, 146]. We attribute this to the broad impurity band in addition to the large area of our junctions. The 16 Å NiO layer in Figure 6.6 (a) shows that several localized states, which are indicated by the small local peaks, are forming a broad impurity band resulting in a big hump around ± 350 mV. The small series of excitation peaks is similar to what Tsui *et al.* [149] reported as multiple magnon excitations. Without any MgO barrier, a 56 Å NiO barrier shows only one symmetric broad peak around ± 300 mV. Therefore we conclude that the excitation peaks in our IETS data are due to the formation of resonant states at the

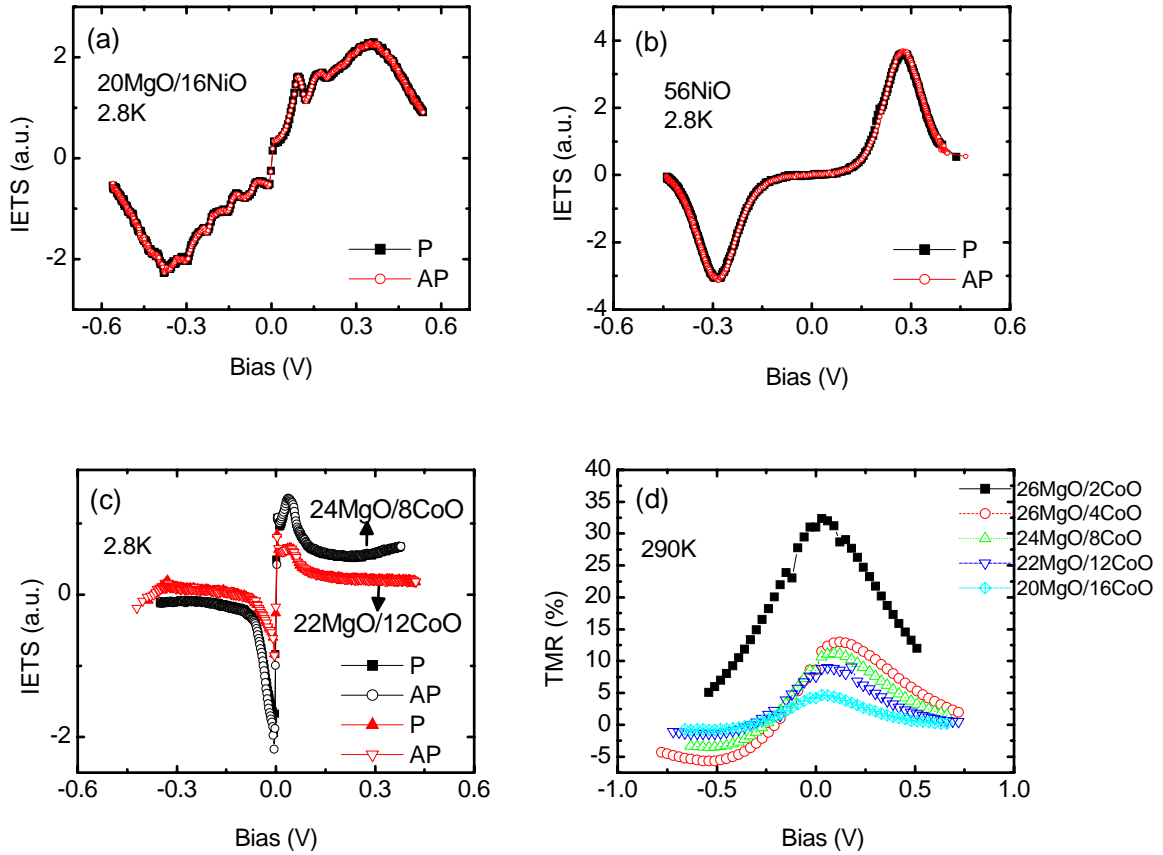


Figure 6.6: (a) IETS from the barrier of 20Å MgO/16Å NiO, (b) IETS from the barrier of 56Å NiO, (c) IETS from the barrier of 24Å MgO/8Å CoO and 22Å MgO/12Å CoO, (d) Voltage dependence of TMR with different CoO thickness.

interface between the MgO and NiO barriers, and are excited by the hot electrons which gain enough energy when electrons tunnel through the barrier. This broad band width is known to weaken both the resonant tunneling effect and the TMR [145]. Above 16Å of the NiO layer, the TMR is fully quenched as can be inferred from the small difference between parallel and antiparallel IETS data in both Figures 6.6 (a) and (b), in contrast to the data of Figure 6.3 (b) or (d). The fact that the localized states are distributed over the entire band energy with thicker NiO or CoO means that as the temperature increases, more channels will be able to conduct and the current spin polarization disappears because of conduction averaging. This also happens in the junction resistance measurements. Without the NiO layer, the junction resistance of the parallel

configuration (R_p) is almost constant from 2.8K to 290K. However, as we increase the NiO thickness, R_p drops more quickly with temperature, suggesting that more hopping electrons via local states are involved in tunneling as the thickness of the NiO layer increases.

We also examined CoO and MnO properties next to the MgO barrier. Some of the IETS features from MgO/CoO composite barriers are shown in Figure 6.6 (c) and TMR dependence in CoO thickness is shown in Figure 6.6 (d). The peak position in IETS moves from 37mV (8Å CoO) to 43mV (12Å CoO), and this is proportional to the transition bias. Even though the total barrier thickness is not fixed unlike the NiO samples discussed previously, Figure 6.6 (d) shows the same trend as MgO/NiO barriers where the transition bias moves to more negative values with thicker CoO layers. 4Å CoO layers gives the biggest asymmetric TMR effect versus bias voltage, and the effect is gradually reduced as we increase the CoO thickness. Among NiO, CoO, and MnO, MnO shows little effect on asymmetric TMR, however MnO also grows epitaxially on top of MgO. This is consistent with the fact that there is no noticeable IETS peak from MgO/MnO barriers.

We discussed the interpretation of our TMR and IETS data in terms of resonant tunneling via localized defect states. The TMR was inverted when the electrons tunnel through the localized states in the barrier if the localized states exist close to one of the electrodes. The observed negative TMR value was quite strong so that we can still see the effect even at room temperature in spite of our large junction area. The resonant state strongly depends on the interfacial atomic and electronic structures of tunnel barriers, thus different materials give quite different features. The controllable spatial location of impurity and energy levels from engineering the thickness of the barriers and changing materials will allow a deeper understanding of the resonant tunneling effect in the future.

Chapter 7. Conclusions & future work

7.1 conclusions

MgO was predicted to give more than 1000% TMR. With careful interface treatment and structural engineering, we achieved nearly 600% TMR at 2.6K, which is very close to theoretical value. Consequently, tunneling spin polarization measurements using superconducting tunneling spectroscopy yield values up to 90%. The extracted barrier height, the bias voltage and temperature dependence of TMR, MgO thickness dependence of TMR imply defect mediate tunneling in the key to understand, hence further improve TMR. In addition more perfect matching of the wavefunction symmetry through strain engineering could be one of the methods to enhance TMR. We developed a novel high temperature superconducting electrode (NbN) for superconducting tunneling spectroscopy. We showed that measurements at elevated temperatures ($\sim 1.2\text{K}$) are possible due to its much lower spin-orbit scattering rate, yet higher superconducting transition temperature, thereby eliminating the need for ^3He dilution refrigerators.

Resonant tunneling effects were explored, such as Kondo resonance and impurity assisted tunneling. We demonstrated not only an increased conductance but also the quenched TMR in the Kondo regime. This suggests that the planar magnetic double tunnel junctions can serve as a powerful tool to probe Kondo physics with reproducible and controllable Kondo temperature (T_k), providing one way to investigate the interactions between impurities when spin dependent bands are formed at both electrodes and impurities. We have explored the properties of MTJs in which we have inserted thin insulating antiferromagnetic (AF) layers formed from oxides of Mn, Ni and Co at the MgO interfaces. The magnitude of the TMR is significantly decreased independent of whether these layers are inserted at the MgO interfaces or within the interior of the MgO layer. More importantly, the sign of the TMR can even be changed, resulting in negative TMR under certain bias voltage conditions. We interpret the negative TMR to be due to

resonant tunneling via localized states in the tunnel barrier based on the data from the inelastic electron tunneling spectroscopy.

7.2 Suggestions for future directions

Future effort is warranted in the exploring new material giving rise to higher spin polarized current, so that spintronic component can be used in the logic application. This new material includes magnetic metal for electrodes and new types of oxide for tunnel barriers. Multiferroics, materials that are both ferroelectric and magnetic, are certainly interesting research topic since it enables the electric field control of magnetism.

Device structure is another aspect we can think about in the future. One reason of the big success of transistors is the gate controllability. This idea can be applied to current day MTJs, which can therefore give one more degree of freedom in addition to that offered by the spin. This scheme may also include electrodes formed from different classes of materials in addition to ferromagnets such as superconductors. More complex tunnel barriers such as those formed from two or more tunneling barriers comprised of both normal and antiferromagnetic materials allow their engineering to achieved desired properties for specific applications. Electron injection with different spin directions can be studied in such structures and how it affects the magneto-transport properties including the material characteristics itself. In-plane spintronic devices can be a good candidate for high current density application and for the integration with conventional CMOS devices.

As device geometries shrink ever more, the incorporation of low dimensional units, such as nanowires and nanodots, is of great interest. Also tunneling characteristics are becoming a significant problem in current CMOS technology. We are exploring the tunneling of spins as the main working principle of a device. In order to make this happen, we first need to understand their basic properties, such as the time scale of spin tunneling and the frequency response of nanoparticles. Coupled nanodots might serve as frequency locked components for future nanoscale circuits.

There are some attempts to modify, as well as detect magnetic properties by light. This offers the prospect of a new research area. Furthermore, magnetic signals can modulate optical signals by coupling. One possible application is the opto-magneto coupler. This is similar to the in-line photodetectors, except that the signal comes from magneto-electronics rather than optical fiber. Investigation of the interaction between magnetic layers and coherent light can be a good direction for future research.

The effort to apply metal spintronics to molecular electronics and bioelectronics has just begun. Interfaces and contacts will be more important in future hybrid systems, where semiconductor, metal, molecules, and tissues need to be connected. Bioengineering is also a very promising area in the future. Magnetic nanoparticles can be a transporting host inside the human body, allowing us to manipulate its motion.

References

- [1] M. Baibich, J. M. Broto, A. Fert, F. N. V. Dau, F. Petroff, P. Etienne, G. Creuzet, A. Friedrich, and J. Chazelas, "Giant Magnetoresistance of (001)Fe/(001)Cr Magnetic Superlattices," *Phys. Rev. Lett.*, vol. 61, pp. 2472, 1988.
- [2] S. S. P. Parkin, N. More, and K. P. Roche, "Oscillations in exchange coupling and magnetoresistance in metallic superlattice structures: Co/Ru, Co/Cr, and Fe/Cr," *Phys. Rev. Lett.*, vol. 64, pp. 2304, 1990.
- [3] J. S. Moodera, L. R. Kinder, T. M. Wong, and R. Meservey, "Large magnetoresistance at room temperature in ferromagnetic thin film tunnel junctions," *Phys. Rev. Lett.*, vol. 74, pp. 3273-3276, 1995.
- [4] T. Miyazaki and N. Tezuka, "Giant magnetic tunneling effect in Fe/Al₂O₃/Fe junction," *J. Magn. Magn. Mat.*, vol. 139, pp. L231, 1995.
- [5] S. S. P. Parkin, X. Jiang, C. Kaiser, A. Panchula, K. Roche, and M. Samant, "Magnetically engineered spintronic sensors and memory," *Proc. IEEE*, vol. 91, pp. 661-680, 2003.
- [6] E. Y. Tsymbal, O. N. Mryasov, and P. R. LeClair, "Spin-dependent tunnelling in magnetic tunnel junctions," *J. Phys. Condens. Mat.*, vol. 15, pp. R109, 2003.
- [7] J. Zhang and R. M. White, "Voltage dependence of magnetoresistance in spin dependent tunneling junctions," *J. Appl. Phys.*, vol. 83, pp. 6512, 1998.
- [8] A. H. MacDonald, T. Jungwirth, and M. Kasner, "Temperature Dependence of Itinerant Electron Junction Magnetoresistance," *Phys. Rev. Lett.*, vol. 81, pp. 705, 1998.
- [9] C. H. Shang, J. Nowak, R. Jansen, and J. S. Moodera, "Temperature dependence of magnetoresistance and surface magnetization in ferromagnetic tunnel junctions," *Phys. Rev. B.*, vol. 58, pp. R2917, 1998.
- [10] M. Julliere, "Tunneling between ferromagnetic films," *Phys. Lett. A*, vol. 54, pp. 225, 1975.
- [11] S. Maekawa and U. Gafvert., "Electron tunneling between ferromagnetic films," *Trans. Magn.*, vol. MAG-18, pp. 707, 1982.
- [12] J. Nowak and J. Rauluszikiewicz., "Spin dependent electron tunneling between ferromagnetic films," *J. Magn. Magn. Mater.*, vol. 109, pp. 79, 1992.
- [13] P. M. Tedrow and R. Meservey, "Spin Polarization of Electrons Tunneling from Films of Fe, Co, Ni, and Gd," *Phys. Rev. B.*, vol. 7, pp. 318, 1973.
- [14] D. J. Monsma and S. S. P. Parkin, "Spin polarization of tunneling current from ferromagnet/Al₂O₃ interfaces using copper-doped aluminum superconducting films," *Appl. Phys. Lett.*, vol. 77, pp. 720, 2000.
- [15] M. B. Stearns, "Simple explanation of tunneling spin-polarization of Fe, Co, Ni and its al," *J. Magn. Magn. Mater.*, vol. 5, pp. 167, 1977.
- [16] J. M. D. Teresa, A. Barthélémy, A. Fert, J. P. Contour, F. Montaigne, and P. Seneor, "Role of Metal-Oxide Interface in Determining the Spin Polarization of Magnetic Tunnel Junctions," *Science*, vol. 286, pp. 507, 1999.

- [17] S. S. P. Parkin, C. Kaiser, A. Panchula, P. Rice, B. Hughes, M. Samant, and S.-H. Yang, "Giant Tunneling Magnetoresistance at Room Temperature with MgO (100) Tunnel Barriers," *Nat. Mater.*, vol. 3, pp. 862, 2004.
- [18] J. C. Slonczewski, "Conductance and exchange coupling of two ferromagnets separated by a tunneling barrier," *Phys. Rev. B.*, vol. 39, pp. 6995, 1989.
- [19] R. Feder, "Polarized Electrons in Surface Physics," 1985.
- [20] Y. S. Dedkov, U. Rüdiger, and G. Güntherodt, "Evidence for the half-metallic ferromagnetic state of Fe₃O₄ by spin-resolved photoelectron spectroscopy," *Phys. Rev. B.*, vol. 65, pp. 064417, 2002.
- [21] R. J. S. Jr., J. M. Byers, M. S. Osofsky, B. Nadgorny, T. Ambrose, S. F. Cheng, P. R. Broussard, C. T. Tanaka, J. Nowak, J. S. Moodera, A. Barry, and J. M. D. Coey, "Measuring the Spin Polarization of a Metal with a Superconducting Point Contact," *Science*, vol. 282, pp. 85, 1998.
- [22] R. Meservey and P. M. Tedrow, "Spin-polarized electron tunneling," *Phys. Rep.*, vol. 238, pp. 173-243, 1994.
- [23] J. W. Gadzuk, "Band-Structure Effects in the Field-Induced Tunneling of Electrons from Metals," *Phys. Rev.*, vol. 182, pp. 416, 1969.
- [24] C. Kaiser, S. v. Dijken, S.-H. Yang, H. Yang, and S. S. P. Parkin, "Role of Tunneling Matrix Elements in Determining the Magnitude of the Tunneling Spin Polarization of 3d Transition Metal Ferromagnetic Alloys," *Phys. Rev. Lett.*, vol. 94, pp. 247203, 2005.
- [25] C. Kaiser, A. F. Panchula, and S. S. P. Parkin, "Finite Tunneling Spin Polarization at the Compensation Point of Rare-Earth-Metal-Transition-Metal Alloys," *Phys. Rev. Lett.*, vol. 95, pp. 047202, 2005.
- [26] I. Giaever, "Energy Gap in Superconductors Measured by Electron Tunneling," *Phys. Rev. Lett.*, vol. 5, pp. 147, 1960.
- [27] J. Bardeen, L. N. Cooper, and J. R. Schrieffer, "Theory of Superconductivity," *Phys. Rev.*, vol. 108, pp. 1175, 1957.
- [28] J. Bardeen, "Tunnelling from a Many-Particle Point of View," *Phys. Rev. Lett.*, vol. 6, pp. 57, 1961.
- [29] D. C. Worledge and T. H. Geballe, "Maki analysis of spin-polarized tunneling in an oxide ferromagnet," *Phys. Rev. B.*, vol. 62, pp. 447, 2000.
- [30] K. Maki, "Pauli paramagnetism and superconducting state II.," *Prog. Theor. Phys.*, vol. 32, pp. 29, 1964.
- [31] W. Meissner and R. Ochsenfeld, *Naturwissenschaften*, vol. 21, pp. 787, 1933.
- [32] K. Maki, "Effect of pauli paramagnetism on magnetic properties of high-field superconductors.," *Phys. Rev.*, vol. 148, pp. 362, 1966.
- [33] A. A. Abrikosov and L. P. Gorkov, *Zh. Eksp. Teor. Fiz.*, vol. 42, pp. 1088, 1962.
- [34] H. Engler and P. Fulde, "The role of spin-orbit scattering in high-field superconducting tunneling.," *Zeitschrift für Physik*, vol. 247, pp. 1, 1971.
- [35] C. Kaiser and S. S. P. Parkin, "Spin polarization in ferromagnet/insulator/superconductor structures with the superconductor on top of the barrier," *Appl. Phys. Lett.*, vol. 84, pp. 3582, 2004.
- [36] L. H. Greene, *Private communication*, 2005.

- [37] J. G. Simmons, "Generalized Formula for the Electric Tunnel Effect between Similar Electrodes Separated by a Thin Insulating Film," *J. Appl. Phys.*, vol. 34, pp. 1793, 1963.
- [38] L. Y. L. Shen and J. M. Rowell, "Zero-Bias Tunneling Anomalies-Temperature, Voltage, and Magnetic Field Dependence," *Phys. Rev.*, vol. 165, pp. 566, 1968.
- [39] R. C. Jaklevic and J. Lambe, "Molecular Vibration Spectra by Electron Tunneling," *Phys. Rev. Lett.*, vol. 17, pp. 1139, 1966.
- [40] K. W. Hipps and U. Mazur, "Handbook of vibrational spectroscopy," 2002.
- [41] D. E. Thomas and J. M. Rowell, "Low level second harmonic detection system," *Rev. Sci. Instr.*, vol. 36, pp. 1301, 1965.
- [42] J. G. Adler and J. E. Jackson, "System for observing small nonlinearities in tunnel junctions," *Rev. Sci. Instr.*, vol. 37, pp. 1049, 1966.
- [43] J. Lambe and R. C. Jaklevic, "Molecular Vibration Spectra by Inelastic Electron Tunneling," *Phys. Rev.*, vol. 165, pp. 821, 1968.
- [44] J. Klein, A. Léger, M. Belin, D. Défourneau, and M. J. L. Sangster, "Inelastic-Electron-Tunneling Spectroscopy of Metal-Insulator-Metal Junctions," *Phys. Rev. B.*, vol. 7, pp. 2336, 1973.
- [45] C. Petit and G. Salace, "Inelastic electron tunneling spectrometer to characterize metal-oxide-semiconductor devices with ultrathin oxides," *Rev. Sci. Instr.*, vol. 74, pp. 4462, 2003.
- [46] H. X. Shen and C. H. C. Li, "Selection of optimum measurement conditions in inelastic electron tunneling spectroscopy (IETS)," *Chin. Phys.*, vol. 2, pp. 232, 1982.
- [47] D. G. Walmsley, R. B. Floyd, and S. F. J. Read, "Inelastic electron tunnelling spectral lineshapes below 10 mK," *J. Phys. C.*, vol. 11, pp. L107, 1987.
- [48] Y. Wang, R. R. Mallik, and P. N. Henriksen, "Easily realized inelastic electron tunneling spectrometer," *Rev. Sci. Instr.*, vol. 64, pp. 890, 1993.
- [49] R. A. d. Groot, F. M. Mueller, P. G. v. Engen, and K. H. J. Buschow, "New Class of Materials: Half-Metallic Ferromagnets," *Phys. Rev. Lett.*, vol. 50, pp. 2024, 983.
- [50] J. S. Parker, S. M. Watts, P. G. Ivanov, and P. Xiong, "Spin Polarization of CrO₂ at and across an Artificial Barrier," *Phys. Rev. Lett.*, vol. 88, pp. 196601, 2002.
- [51] D. L. Camphausen, J. M. D. Coey, and B. K. Chakraverty, "One-Electron Energy Levels in Fe₃O₄," *Phys. Rev. Lett.*, vol. 29, pp. 657, 1972.
- [52] J. H. Park, E. Vescovo, H. Kim, C. Kwon, R. Ramesh, and T. Venkatesan, "Direct evidence for a half-metallic ferromagnet," *Nature*, vol. 392, pp. 794, 1998.
- [53] J. Z. Sun, D. W. Abraham, K. Roche, and S. S. P. Parkin, "Temperature and bias dependence of magnetoresistance in doped manganite thin film trilayer junctions," *Appl. Phys. Lett.*, vol. 73, pp. 1008, 1998.
- [54] P. A. Dowben and R. Skomski, "Finite-temperature spin polarization in half-metallic ferromagnets," *J. Appl. Phys.*, vol. 93, pp. 7948, 2003.
- [55] S. S. P. Parkin, "Magnetically engineered spintronic sensors and memory," *Proc. IEEE*, vol. 91, pp. 661, 2003.
- [56] D. Wang, C. Nordman, J. M. Daughton, Z. Qian, and J. Fink, "70% TMR at room temperature for SDT sandwich junctions with CoFeB as free and reference layers.," *IEEE Trans. Magn.*, vol. 40, pp. 2269, 2004.

- [57] W. H. Butler, X.-G. Zhang, T. C. Schulthess, and J. M. MacLaren, "Spin-dependent tunneling conductance of Fe|MgO|Fe sandwiches," *Phys. Rev. B.*, vol. 63, pp. 054416, 2001.
- [58] P. Mavropoulos, N. Papanikolaou, and P. H. Dederichs, "Complex Band Structure and Tunneling through Ferromagnet /Insulator /Ferromagnet Junctions," *Phys. Rev. Lett.*, vol. 85, pp. 1088, 2000.
- [59] J. Mathon and A. Umerski, "Theory of tunneling magnetoresistance of an epitaxial Fe/MgO/Fe(001) junction," *Phys. Rev. B.*, vol. 63, pp. 220403, 2001.
- [60] X.-G. Zhang, W. H. Butler, and A. Bandyopadhyay, "Effects of the iron-oxide layer in Fe-FeO-MgO-Fe tunneling junctions," *Phys. Rev. B.*, vol. 68, pp. 092402, 2003.
- [61] M. Bowen, V. Cros, F. Petroff, A. Fert, C. M. Boubeta, J. L. Costa-Krämer, J. V. Anguita, A. Cebollada, F. Briones, J. M. d. Teresa, L. Morellon, M. R. Ibarra, F. Güell, F. Peiro, and A. Cornet, "Large magnetoresistance in Fe/MgO/FeCo(001) epitaxial tunnel junctions on GaAs(001)," *Appl. Phys. Lett.*, vol. 79, pp. 1655, 2001.
- [62] J. Faure-Vincent, C. Tiusan, E. Jouguelet, F. Canet, M. Sajieddine, C. Bellouard, E. Popova, M. Hehn, F. Montaigne, and A. Schuhl, "High tunnel magnetoresistance in epitaxial Fe/MgO/Fe tunnel junctions," *Appl. Phys. Lett.*, vol. 82, pp. 4507, 2003.
- [63] S. Yuasa, A. Fukushima, T. Nagahama, K. Ando, and Y. Suzuki, "High Tunnel Magnetoresistance at Room Temperature in Fully Epitaxial Fe/MgO/Fe Tunnel Junctions due to Coherent Spin-Polarized Tunneling," *Jpn. J. Appl. Phys.*, vol. 43, pp. L588, 2004.
- [64] S. Yuasa, T. Nagahama, A. Fukushima, Y. Suzuki, and K. Ando, "Giant room-temperature magnetoresistance in single-crystal Fe/MgO/Fe magnetic tunnel junctions," *Nat. Mater.*, vol. 3, pp. 868, 2004.
- [65] D. D. Djayaprawira, K. Tsunekawa, M. Nagai, H. Maehara, S. Yamagata, N. Watanabe, S. Yuasa, Y. Suzuki, and K. Ando, "230% room-temperature magnetoresistance in CoFeB/MgO/CoFeB magnetic tunnel junctions," *Appl. Phys. Lett.*, vol. 86, pp. 092502, 2005.
- [66] K. Tsunekawa, D. D. Djayaprawira, M. Nagai, H. Maehara, S. Yamagata, N. Watanabe, S. Yuasa, Y. Suzuki, and K. Ando, "Giant tunneling magnetoresistance effect in low-resistance CoFeB/MgO(001)/CoFeB magnetic tunnel junctions for read-head applications," *Appl. Phys. Lett.*, vol. 87, pp. 072503, 2005.
- [67] K. Nagasaka, Y. Seyama, R. Kondo, H. Oshima, Y. Shimizu, and A. Tanaka, "CPP operational mode of GMR head," *Fujitsu Sci. Tech. J.*, vol. 37, pp. 192, 2001.
- [68] S. S. P. Parkin, K. P. Roche, M. G. Samant, P. M. Rice, R. B. Beyers, R. E. Scheuerlein, E. J. O'Sullivan, S. L. Brown, J. Bucchigano, D. W. Abraham, M. R. Yu Lu, P. L. Trouilloud, R. A. Wanner, and W. J. Gallagher, "Exchange-biased magnetic tunnel junctions and application to nonvolatile magnetic random access memory," *J. Appl. Phys. Lett.*, vol. 85, pp. 5828, 1999.
- [69] K. Tsunekawa, D. D. Djayaprawira, M. Nagai, H. Maehara, S. Yamagata, and N. Watanabe, "Effect of capping layer material on tunnel magnetoresistance in

- CoFeB/MgO/CoFeB magnetic tunnel junctions," *Digests of the IEEE International Magnetism Conference*, pp. HP-08, 2005.
- [70] H. L. Meyerheim, R. Popescu, J. Kirschner, N. Jedrecy, M. Sauvage-Simkin, B. Heinrich, and R. Pinchaux., "Geometrical and Compositional Structure at Metal-Oxide Interfaces: MgO on Fe(001)," *Phys. Rev. Lett.*, vol. 87, pp. 076102, 2001.
- [71] H. L. Meyerheim, R. Popescu, N. Jedrecy, M. Vedpathak, M. Sauvage-Simkin, R. Pinchaux, B. Heinrich, and J. Kirschner., "Surface x-ray diffraction analysis of the MgO/Fe(001) interface: Evidence for an FeO layer," *Phys. Rev. B.*, vol. 65, pp. 144433, 2002.
- [72] C. Tusche, H. L. Meyerheim, N. Jedrecy, G. Renaud, A. Ernst, J. Henk, P. Bruno, and J. Kirschner, "Oxygen-Induced Symmetrization and Structural Coherency in Fe/MgO/Fe(001) Magnetic Tunnel Junctions," *Phys. Rev. Lett.*, vol. 95, pp. 176101, 2005.
- [73] E. Tan, P. G. Mather, A. C. Perrella, J. C. Read, and R. A. Buhrman, "Oxygen stoichiometry and instability in aluminum oxide tunnel barrier layers," *Phys. Rev. B.*, vol. 71, pp. 161401, 2005.
- [74] J. Read, P. Mather, E. Tan, and R. Buhrman, "XPS studies of the growth and interfacial structure of MgO tunnel barrier layers," *50th annual conference on magnetism and magnetic materials*, pp. CB-12, 2005.
- [75] J. Y. Bae, W. C. Lim, H. J. Kim, T. D. Lee, K. W. Kim, and T. W. Kim, "Compositional change of MgO barrier and interface in CoFeB/MgO/CoFeB tunnel junction after annealing," *50th annual conference on magnetism and magnetic materials*, pp. HS-18, 2005.
- [76] J. M. MacLaren, X.-G. Zhang, W. H. Butler, and X. Wang, "Layer KKR approach to Bloch-wave transmission and reflection: Application to spin-dependent tunneling," *Phys.Rev. B.*, vol. 59, pp. 5470, 1999.
- [77] W. Plesiewicz and J. G. Adler, "Inelastic electron-tunneling study of MgO barriers," *Phys. Rev. B.*, vol. 34, pp. 4583, 1986.
- [78] R. J. M. v. d. Veerdonk, J. S. Moodera, and W. J. M. d. Jonge, "Characterization of magnetic tunnel junctions using IETS," *J. Magn. Magn. Mat.*, vol. 198-199, pp. 152, 1999.
- [79] X.-F. Han, J. Murai, Y. Ando, H. Kubota, and T. Miyazaki, "Inelastic magnon and phonon excitations in $\text{Al}_{1-x}\text{Co}_x/\text{Al}_{1-x}\text{Co}_x\text{-oxide}/\text{Al}$ tunnel junctions," *Appl. Phy. Lett.*, vol. 78, pp. 2533, 2001.
- [80] J. S. Moodera, J. Nowak, and R. J. M. v. d. Veerdonk, "Interface Magnetism and Spin Wave Scattering in Ferromagnet-Insulator-Ferromagnet Tunnel Junctions," *Phys.Rev. Lett.*, vol. 80, pp. 2941, 1998.
- [81] V. Senz, R. Rohlsberger, J. Bansmann, O. Leupold, and K.-H. Meiwes-Broer, "Temperature dependence of the magnetization in Fe islands on W(110): evidence for spin-wave quantization," *New Journal of Physics*, vol. 5, pp. 47.1, 2003.
- [82] Y. Ando, T. Miyakoshi, M. Oogane, T. Miyazaki, H. Kubota, K. Ando, and S. Yuasa, "Spin-dependent tunneling spectroscopy in single-crystal Fe/MgO/Fe tunnel junctions," *Appl. Phy. Lett.*, vol. 87, pp. 142502, 2005.
- [83] S. Zhang, P. M. Levy, A. C. Marley, and S. S. P. Parkin, "Quenching of Magnetoresistance by Hot Electrons in Magnetic Tunnel Junctions," *Phys.Rev. Lett.*, vol. 79, pp. 3744, 1997.

- [84] W. H. Butler, *Private communication*, 2006.
- [85] C. Kaiser, "Novel materials for magnetic tunnel junctions," *Ph. D. Thesis*, University of Aachen, 2004.
- [86] T. Ishiguro, K. Matsushima, and K. Hamasaki, "Sectional structures and electrical properties of ultrathin NbN/MgO bilayers on Si(100)," *J. Appl. Phys.*, vol. 73, pp. 1151, 1993.
- [87] A. Kawakami, Y. Uzawa, and Z. Wang, "Development of epitaxial NbN/MgO/NbN-superconductor-insulator-superconductor mixers for operations over the Nb gap frequency," *Appl. Phys. Lett.*, vol. 83, pp. 3954, 2003.
- [88] B. Y. Jin and J. B. Ketterson, "Artificial metallic superlattices," *Adv. Phys.*, vol. 38, pp. 189, 1989.
- [89] G. A. Gibson, P. M. Tedrow, and R. Meservey, "Tunneling study of Fermi-liquid effects in amorphous gallium," *Phys. Rev. B.*, vol. 40, pp. 137, 1989.
- [90] E. L. Wolf, *Principles of electron tunneling spectroscopy*. New York: Oxford University Press, 1989.
- [91] K. Maki, "The Behavior of Superconducting Thin Films in the Presence of Magnetic Fields and Currents," *Prog. Theor. Phys.*, vol. 31, pp. 731, 1964.
- [92] G. A. Gibson and R. Meservey, "Evidence for spin fluctuations in vanadium from a tunneling study of Fermi-liquid effects," *Phys. Rev. B.*, vol. 40, pp. 8705, 1989.
- [93] L. Kouwenhoven and L. Glazman, "Revival of the Kondo effect," *Physics world*, vol. 14, pp. 33, 2001.
- [94] D. Goldhaber-Gordon, H. Shtrikman, D. Mahalu, D. Abusch-Magder, U. Meirav, and M. A. Kastner, "Kondo effect in a single-electron transistor," *Nature*, vol. 391, pp. 156-159, 1998.
- [95] S. M. Cronenwett, T. H. Oosterkamp, and L. P. Kouwenhoven, "A Tunable Kondo Effect in Quantum Dots," *Science*, vol. 281, pp. 540, 1998.
- [96] P. W. Anderson, "Localized magnetic states in metals," *Phys. Rev.*, vol. 124, pp. 41-53, 1961.
- [97] J. Kondo, "Resistance minimum in dilute magnetic alloys," *Prog. Theor. Phys.*, vol. 32, pp. 37-49, 1964.
- [98] P. W. Anderson, "Localized magnetic states and fermi-surface anomalies in tunneling," *Phys. Rev. Lett.*, vol. 17, pp. 95-97, 1966.
- [99] J. A. Appelbaum, "Exchange model of zero-bias tunneling anomalies," *Phys. Rev.*, vol. 154, pp. 633-643, 1967.
- [100] J. Nygard, Cobden, D. H. & Lindelof, P. E., "Kondo physics in carbon nanotubes," *Nature*, vol. 408, pp. 342-346, 2000.
- [101] J. Park, A. Pasupathy, J. Goldsmith, C. Chang, Y. Yaish, J. Petta, M. Rinkoski, JPSethna, H. Abruna, P. McEuen, and D. Ralph, "Coulomb blockade and the Kondo effect in single-atom transistors.," *Nature*, vol. 417, pp. 722-725, 2002.
- [102] W. Liang, M. P. Shores, M. Bockrath, J. R. Long, and H. Park, "Kondo resonance in a single-molecule transistor," *Nature*, vol. 417, pp. 725-729, 2002.
- [103] J. S. Moodera, L. R. Kinder, T. M. Wong, and R. Meservey, "Large magnetoresistance at room temperature in ferromagnetic thin film tunnel junctions," *Phys. Rev. Lett.*, vol. 74, pp. 3273-3276, 1995.

- [104] S. Colis, G. Gieres, L. Bär, and J. Wecker, "Low tunnel magnetoresistance dependence versus bias voltage in double barrier magnetic tunnel junction," *Appl. Phys. Lett.*, vol. 83, pp. 948, 2003.
- [105] K. Inomata, Y. Saito, K. Nakajima, and M. Sagoi, "Double tunnel junctions for magnetic random access memory devices," *J. Appl. Phys.*, vol. 87, pp. 6064-6066, 2000.
- [106] J. Barnas and A. Fert, "Magnetoresistance oscillations due to charging effects in double ferromagnetic tunnel junctions," *Phys. Rev. Lett.*, vol. 80, pp. 1058, 1998.
- [107] S. Takahashi and S. Maekawa, "Effect of Coulomb blockade on magnetoresistance in ferromagnetic tunnel junctions," *Phys. Rev. Lett.*, vol. 80, pp. 1758, 1998.
- [108] S. Mitani, S. Takahashi, K. Takanashi, K. Yakushiji, S. Maekawa, and H. Fujimori, "Enhanced magnetoresistance in insulating granular systems: evidence for higher-order tunneling," *Phys. Rev. Lett.*, vol. 81, pp. 2799-2802, 1998.
- [109] H. Sukegawa, S. Nakamura, A. Hirohata, N. Tezuka, and K. Inomata, "Significant Magnetoresistance Enhancement due to a Cotunneling Process in a Double Tunnel Junction with Single Discontinuous Ferromagnetic Layer Insertion," *Phys. Rev. Lett.*, vol. 94, pp. 068304, 2005.
- [110] J. Martinek, J. Barnas, A. Fert, S. Maekawa, and G. Schon, "Transport in magnetic nanostructures in the presence of Coulomb interaction," *J. Appl. Phys.*, vol. 93, pp. 8265-8270, 2003.
- [111] A. F. G. Wyatt, "Anomalous Densities of States in Normal Tantalum and Niobium," *Phys. Rev. Lett.*, vol. 13, pp. 401-404, 1964.
- [112] Q.-K. X. Ping Zhang, Yupeng Wang, and X. C. Xie., "Spin-Dependent Transport through an Interacting Quantum Dot," *Phys. Rev. Lett.*, vol. 89, pp. 286803-1--286803-4, 2002.
- [113] J. Martinek, M. Sindel, L. Borda, J. Barnas, J. König, G. Schon, and J. v. Delft, "Kondo Effect in the Presence of Itinerant-Electron Ferromagnetism Studied with the Numerical Renormalization Group Method," *Phys. Rev. Lett.*, vol. 91, pp. 247202, 2003.
- [114] M.-S. Choi, D. Sanchez, and R. Lopez, "Kondo Effect in a Quantum Dot Coupled to Ferromagnetic Leads: A Numerical Renormalization Group Analysis," *Phys. Rev. Lett.*, vol. 92, pp. 056601, 2004.
- [115] J. Martinek, Y. Utsumi, H. Imamura, J. Barnas, S. Maekawa, J. König, and G. Schön, "Kondo effect in quantum dots coupled to ferromagnetic leads," *Phys. Rev. Lett.*, vol. 91, pp. 127203, 2003.
- [116] A. N. Pasupathy, R. C. Bialczak, J. Martinek, J. E. Grose, L. A. K. Donev, P. L. McEuen, and D. C. Ralph, "The Kondo Effect in the Presence of Ferromagnetism," *Science*, vol. 306, pp. 86-89, 2004.
- [117] A. J. Heinrich, J. A. Gupta, C. P. Lutz, and D. M. Eigler, "Single-Atom Spin-Flip Spectroscopy," *Science*, vol. 306, pp. 466-469, 2004.
- [118] V. Madhavan, W. Chen, T. Jamneala, M. F. Crommie, and N. S. Wingreen, "Tunneling into a Single Magnetic Atom: Spectroscopic Evidence of the Kondo Resonance," *Science*, vol. 280, pp. 567-569, 1998.
- [119] R. H. Wallis and A. F. G. Wyatt, "Evidence for Interactions in Magnetically Doped Tunnel Junctions," *Phys. Rev. Lett.*, vol. 29, pp. 479-482, 1972.

- [120] T. K. Ng and P. A. Lee, "On-site Coulomb repulsion and resonant tunneling," *Phys. Rev. Lett.*, vol. 61, pp. 1768-1771, 1988.
- [121] R. Lopez and D. Sanchez., "Nonequilibrium Spintronic Transport through an Artificial Kondo Impurity: Conductance, Magnetoresistance, and Shot Noise," *Phys. Rev. Lett.*, vol. 90, pp. 116602, 2003.
- [122] J. Ma and X. L. Lei, "Kondo correlation and spin-flip scattering in spin-dependent transport through a quantum dot coupled to ferromagnetic leads," *Europhys. Lett.*, vol. 67, pp. 432-438, 2004.
- [123] P. Zhang, Q.-K. Xue, Y. Wang, and X. C. Xie, "Spin-Dependent Transport through an Interacting Quantum Dot," *Phys. Rev. Lett.*, vol. 89, pp. 286803, 2002.
- [124] A. C. Hewson, *The Kondo Problem to Heavy Fermions*. Cambridge: Cambridge University Press, 1993.
- [125] M. G. Samant, J. Lüning, J. Stöhr, and S. S. P. Parkin, "Thermal stability of IrMn and MnFe exchange-biased magnetic tunnel junctions," *Appl. Phys. Lett.*, vol. 76, pp. 3097, 2000.
- [126] P. LeClair, J. T. Kohlhepp, C. H. v. d. Vin, H. Wieldraaijer, H. J. M. Swagten, W. J. M. d. Jonge, A. H. Davis, J. M. MacLaren, J. S. Moodera, and R. Jansen, "Band Structure and Density of States Effects in Co-Based Magnetic Tunnel Junctions," *Phys. Rev. Lett.*, vol. 88, pp. 107201, 2002.
- [127] H. F. Ding, W. Wulfhekel, J. Henk, P. Bruno, and J. Kirschner, "Absence of Zero-Bias Anomaly in Spin-Polarized Vacuum Tunneling in Co(0001)," *Phys. Rev. Lett.*, vol. 90, pp. 116603, 2003.
- [128] J. S. Moodera, J. Nowak, L. R. Kinder, and P. M. Tedrow, "Quantum Well States in Spin-Dependent Tunnel Structures," *Phys. Rev. Lett.*, vol. 83, pp. 3029, 1999.
- [129] T. Nagahama, S. Yuasa, Y. Suzuki, and E. Tamura, "Quantum-well effect in magnetic tunnel junctions with ultrathin single-crystal Fe(100) electrodes," *Appl. Phys. Lett.*, vol. 79, pp. 4381, 2001.
- [130] S. Yuasa, T. Nagahama, and Y. Suzuki, "Spin-Polarized Resonant Tunneling in Magnetic Tunnel Junctions," *Science*, vol. 297, pp. 234, 2002.
- [131] P. LeClair, J. T. Kohlhepp, H. J. M. Swagten, and W. J. M. d. Jonge, "Interfacial Density of States in Magnetic Tunnel Junctions," *Phys. Rev. Lett.*, vol. 86, pp. 1066, 2000.
- [132] P. LeClair, B. Hoex, H. Wieldraaijer, J. T. Kohlhepp, H. J. M. Swagten, and W. J. M. d. Jonge, "Sign reversal of spin polarization in Co/Ru/Al₂O₃/Co magnetic tunnel junctions," *Phys. Rev. B.*, vol. 64, pp. 100406, 2001.
- [133] M. O. Bowen, "Experimental insights into spin-polarized solid state tunneling," *Ph. D. Thesis, Unité Mixte de Physique CNRS/Thales*, 2003.
- [134] W. Oepts, M. F. Gillies, R. Coehoorn, R. J. M. v. d. Veerdonk, and W. J. M. d. Jonge, "Asymmetric bias voltage dependence of the magnetoresistance of Co/Al₂O₃/Co magnetic tunnel junctions: Variation with the barrier oxidation time," *J. Appl. Phys.*, vol. 89, pp. 8038, 2001.
- [135] H. Brückl, J. Schmalhorst, and G. Reiss, "Evolution of barrier asymmetry in magnetic tunnel junctions," *Appl. Phys. Lett.*, vol. 78, pp. 1113, 2001.
- [136] M. Sharma, S. X. Wang, and J. H. Nickel, "Inversion of Spin Polarization and Tunneling Magnetoresistance in Spin-Dependent Tunneling Junctions," *Phys. Rev. Lett.*, vol. 82, pp. 616, 1999.

- [137] O. Wunnicke, N. Papanikolaou, R. Zeller, P. H. Dederichs, V. Drchal, and J. Kudrnovský, "Effects of resonant interface states on tunneling magnetoresistance," *Phys. Rev. B.*, vol. 65, pp. 064425, 2002.
- [138] E. Y. Tsymbal and D. G. Pettifor, "Spin-polarized electron tunneling across a disordered insulator," *Phys. Rev. B.*, vol. 58, pp. 432, 1998.
- [139] W. Wulfhekel, M. Klaua, D. Ullmann, F. Zavaliche, J. Kirschner, R. Urban, T. Monchesky, and B. Heinrich, "Single-crystal magnetotunnel junctions," *Appl. Phys. Lett.*, vol. 78, pp. 509, 2001.
- [140] P. LeClair, H. J. M. Swagten, J. T. Kohlhepp, R. J. M. v. d. Veerdonk, and W. J. M. d. Jonge, "Apparent Spin Polarization Decay in Cu-Dusted Co/Al₂O₃/Co Tunnel Junctions," *Phys. Rev. B.*, vol. 84, pp. 2933, 2000.
- [141] R. Landauer, "Spatial variation of currents and fields due to localized scatterers in metallic conduction," *IBM J. Res. Dev.*, vol. 32, pp. 306, 1988.
- [142] E. Y. Tsymbal, A. Sokolov, I. F. Sabirianov, and B. Doudin, "Resonant Inversion of Tunneling Magnetoresistance," *Phys. Rev. Lett.*, vol. 90, pp. 186602, 2003.
- [143] S. Maekawa and U. Gafvert, "Electron tunneling between ferromagnetic films," *IEEE Trans. Magn.*, vol. 18, pp. 707, 1982.
- [144] B. Doudin, G. Redmond, S. E. Gilbert, and J.-P. Ansermet, "Magnetoresistance Governed by Fluctuations in Ultrasmall Ni/NiO/Co Junctions," *Phys. Rev. Lett.*, vol. 79, pp. 933, 1997.
- [145] V. Garcia, H. Jaffrès, M. Eddrief, M. Marangolo, V. H. Etgens, and J.-M. George, "Resonant tunneling magnetoresistance in MnAs/III-V/MnAs junctions," *Phys. Rev. B.*, vol. 72, pp. 081303, 2005.
- [146] J. Varalda, A. J. A. d. Oliveira, D. H. Mosca, J.-M. George, M. Eddrief, M. Marangolo, and V. H. Etgens, "Resonant tunnel magnetoresistance in epitaxial metal-semiconductor heterostructures," *Phys. Rev. B.*, vol. 72, pp. 081302, 2005.
- [147] F. Montaigne, M. Hehn, and A. Schuhl, "Tunnel barrier parameters and magnetoresistance in the parabolic band model," *Phys. Rev. B.*, vol. 64, pp. 144402, 2001.
- [148] F.-f. Li, Z.-z. Li, M.-w. Xiao, J. Du, W. Xu, and A. Hu, "Bias dependence and inversion of the tunneling magnetoresistance in ferromagnetic junctions," *Phys. Rev. B.*, vol. 69, pp. 054410, 2004.
- [149] D. C. Tsui, R. E. Dietz, and L. R. Walker, "Multiple Magnon Excitation in NiO by Electron Tunneling," *Phys. Rev. Lett.*, vol. 27, pp. 1729, 1971.